TECHNISCHE
UNIVERSITÄT
WIEN
Vienna | Austria

Additive Manufacturing of fiber-reinforced Ceramics

SLURRY OPTIMIZATION FOR DIGITAL LIGHT PROCESSING AND CERAMIC MATRIX COMPOSITE STRENGTHING

Durchführt am:

Institut für Werkstoffwissenschaft and Werkstofftechnologie TU Wien, im Forschungsbereich Polymer- und Verbundwerkstoffe, in der Forschungsgruppe Werkstoffe und Additive Fertigung.

Unter der Betreuung von:

Univ.Prof. Dipl.-Ing. Dr. mont. Jürgen Stampfl

Projektass. Dipl.-Ing. Anna Lea Kutsch

Von

Bodo Baumgartner

01269118

Wien, 2022

Table of Content

1. Introduction 3
1.1. Hard tissue engineering 3
1.2. Ceramics as bone replacement materials 4
2. Goal of the Thesis 5
3. Theoretical Background 6
3.1. Additive Manufacturing 6
3.2. Lithography-based 3D-Printing 8
3.2.1. Stereolithography 8
3.2.2. Digital Light Processing 11
3.2.3. Blueprinter 6 (BP6) 12
3.3. Photopolymerization 14
3.4. Photoinitiator 17
3.4.1. Curing Depth 19
3.5. Ceramic Slurry 21
3.5.1. Ceramic Matrix Composites (CMCs) 23
3.5.2. Aluminum oxide (Al_2O_3) 24
3.5.3. Aluminum silicate 25
3.5.4. Slurry Stabilization 26
3.6. Thermal post-processing 27
3.6.1. Debinding 28
3.6.2. Sintering 30
4. Experimental Part 32
4.1. Chemicals 32
4.2. Devices 33
4.3. Optimization of the Slurry 35
4.3.1. Slurry Composition 35
4.3.2. Dispersing the Filler Materials 38
4.3.3. Slurry preparation 41
4.3.4. Optical Analysis 43
4.3.5. Rheology Measurements 48
4.4. Optimization of the Print 49
4.4.1. Adjusting the Printer 49
4.4.2. Sample Manufacturing with the BP6 51
4.4.3. Curing depth 55
4.4.4. Shrinkage 56

4.5. Thermal Treatments 57
4.5.1. Debinding Profiles 57
4.5.2. Sintering Profiles 59
4.5.3. Thermomechanical Analysis 60
4.5.4. Thermogravimetric Analysis 61
4.6. Mechanical Testing 62
4.6.2. Biaxial Bending Tests 62
4.7. Density Determination by Archimedes' Principle 64
5. Results and Discussion 66
5.1. Optimization of the Slurry 66
5.1.1. Slurry Composition 66
5.1.2. Dispersing the Filler Material 68
5.1.3. Rheology Measurements 76
5.2. Optimization of the Print 80
5.2.1. Sample Manufacturing with the BP6 80
5.2.2. Curing Depth 80
5.3. Thermal Treatment 83
5.3.1. Debinding 83
5.3.2. Sintering 85
5.3.3. Thermomechanical Analysis 87
5.3.4. Thermogravimetric Analysis 90
5.4. Mechanical Testing 92
5.4.1. Biaxial Bending Test 92
5.4.2. Weibull Modulus 98
5.5. Density Determination by Archimedes' Principle 100
6. Conclusion 102
7. References 104

1. Introduction

1.1. Hard tissue engineering

In 1993, tissue engineering was defined as the combination of principles of engineering and life sciences with the goal of developing biological substitutes that are able to restore, maintain or improve biological tissue function or the whole organ. [1,2]

Keeping in mind, that bone is the second most common tissue requiring repair after blood vessels it was imperative that the field of hard tissue engineering emerged. [3]

There are two main approaches to achieve this. Firstly, the top-down strategy, based on scaffold to which cell are introduced. Secondly the bottom-up approach, also referred to as "biofabrication", where the matrix material and cell are introduced at the beginning to build up larger constructs. [4,5]

In most cases high load-bearing requirements need to be fulfilled, this causes a focus on top-down strategies, with porous scaffolds for cell seeding. Furthermore, materials of inherent biological and chemical similarities to native tissue are of great interest. These include natural polymers, polymer-based composites and bioceramics, as they fulfill biocompatibility requirements as well as mechanical ones. [6,7]

The goal of hard tissue engineering is to find better alternatives to autografts or allografts. [8]

1.2. Ceramics as bone replacement materials

Ceramics are a large class of crystalline, semicrystalline and amorphous materials. When used to repair or reconstruct parts in the body, they are referred to as bioceramics. The use in medical applications can be dated back to the 17th century, as calcium sulfate was used to repair bones of mummies and cadavers. It was firstly implanted in the living human body as a treatment of tuberculous osteomyelitis in 1892. [9,10]

The gold standard of bone replacement is still the autologous or allogenous bone transplantation, which means taking bone from somewhere else of the patient's body or a donor, to replace the damaged bone. To tackle drawbacks of these methods, as slow bone ingrowth, vascularization and disease transmission (when coming from a donor), artificial bone substitutes have been introduced. [11]

Today the materials being used for bone grafting are ranging from inert ceramics (e.g., alumina or zirconia) to hydroxyapatite (HA) and bioactive glasses and can be categorized in Type 1 to 4. [12]

Type 1 being an inert, dense, nonporous material that is attached via "morphological fixation" (e.g., alumina). Type 2 is porous, inert and attaches via bone ingrowth called "biological fixation" (e.g., polycrystalline materials or HA-coated materials). Type 3 are surface active materials, which are dense and nonporous, that undergo "bioactive fixation" via chemical bonding. (e.g., Bioactive Glasses or HA). Lastly, type 4 are dense, nonporous or porous, resorbable ceramics meant to slowly be replaced by growing bone.

Bioinert ceramics as alumina are commonly used in orthopedics (knee or hip replacement) or dentistry (implants or crowns). They remain relevant due to their high mechanical properties like tensile, compressive, hardness, low wear, toughness and good anticorrosion in biological fluid.[13]

An important paradigm shift happened with additive manufacturing (AM), especially light-induced layer-by-layer methods as stereolithography (SLA) or digital light processing (DLP) and other methods for example fused deposition modeling (FDM). The light-induced techniques provide a higher resolution and therefore lead to more precise parts, which can be patient-specific, as AM is based on computer-aided-design.[14]

2. Goal of the Thesis

As discussed in chapter 1.2., aluminum oxide is an example for a high-performance bioceramic. It provides a combination of both excellent physical and chemical properties. Of special relevance are the high abrasion and corrosion resistance, good mechanical strength and biocompatibility. Therefore, aluminum oxide is very interesting material for implants (e.g. hip implants).[15]

The main disadvantage of ceramics is their low fracture toughness. A solution for increasing toughness as well as strength could be the use of fiber reinforced aluminum oxide. It was proven with WHIPOX®, which is an all-oxide ceramic matrix composite (OCMC) material, that oxide ceramic fiber reinforced composites can show ductile behavior, while having a brittle matrix. This is achieved via fiber pull-out, crack branching and/or deflection.[16]

A restriction of ceramic matrix composites (CMCs) is that they are still limited to traditional production methods. This limits their field of application.

Thus, the goal of this master thesis was to investigate the processing of ceramic matrix composites via digital light processing. This is a slurry-based ceramic 3D printing technology including a liquid resin system dispersed with ceramic nanoparticles and fibers as feedstock. This slurry can then be 3D printed by via photopolymerization of the resin. Lastly, the printed green bodies are thermally treated to create the finished CMC part. In order to achieve this, different criterions have to be met.[17]

Firstly, the organic matrix was optimized. During this step all materials were homogenously dispersed. Secondly, the preparation process of the slurry was investigated and fine-tuned, leading to agglomerates that were at least smaller than the layer thickness of the printed layers. Thirdly, the print job was adjusted to the used “ink material”. Lastly, the postprocessing, including thermal treatments, was optimized, concluding to the final ceramic part.

In order to evaluate the mechanical properties of the sintered samples, the focus was kept on the biaxial bending test, as it is common for biocompatible ceramics.[18] The fiber-reinforcement should impact the bending strength as well as the elongation at break.

3. Theoretical Background

3.1. Additive Manufacturing

3D-Printing or additive manufacturing (AM) are both synonyms for a production process creating physical objects from a digital file by successive addition of materials. The American Society for Testing and Materials defines it as:

"[..]the process of joining materials to make objects from 3D model data, usually layer upon layer, as opposed to subtractive manufacturing methodologies, such as traditional machining." [19]

3D-printing originates from layer-by-layer fabrication of 3D-structures which have been designed by computer-aided design (CAD). The process includes two steps, the generation of a mathematical layer information and the manufacturing of the physical layers. When these layers are connected, a 3D object results, with the printed geometry closely resembling the original CAD-data. [20]

AM technologies were commercialized in the 1980s, when Charles Hull introduced stereolithography. Nowadays, AM is used for producing artificial heart pumps, hearing aids, jewelry and even rocket engines, among others. Application fields range from health care over the food industry to the aerospace industry. [19,21,22]

AM has the ability to improve manufacturing efficiency and change the production line, as it enables resource-efficient production of small-pot production or prototyping without expensive tools or molds. Other benefits are that the demand of the consumer has a bigger influence on the production and that it enables high freedom in design, which allows the production of highly complex structures, impossible with subtractive methods. [23,24]

Nowadays, we are able to utilize a large number of different materials, ranging from conventional thermoplastics to graphene-based materials.. AM technologies can be briefly sorted into 7 types, shown in Fig 1:[25]

- Vat Photopolymerization
  Light-induced polymerization of a photosensitive resin, which is deposited in a vat and solidifies in the process. (e.g., SLA)
- Sheet Lamination
  Material sheets are connected after being stacked to form an object.

- Powder Bed Fusion

  Powdered Material is fused together via a heat source. (e.g., laser or electron-beam)
- Material Jetting

  Material droplets are deposited and solidified.
- Material Extrusion

  Extrusion of a material through nozzle onto a building platform. (e.g., FDM)
- Direct Energy Deposition

  An energy source (e.g., laser or e^--beam) melts powdered or wired material upon deposition.
- Binder Jetting

  Powdered Material is connected selectively via a liquid binder.

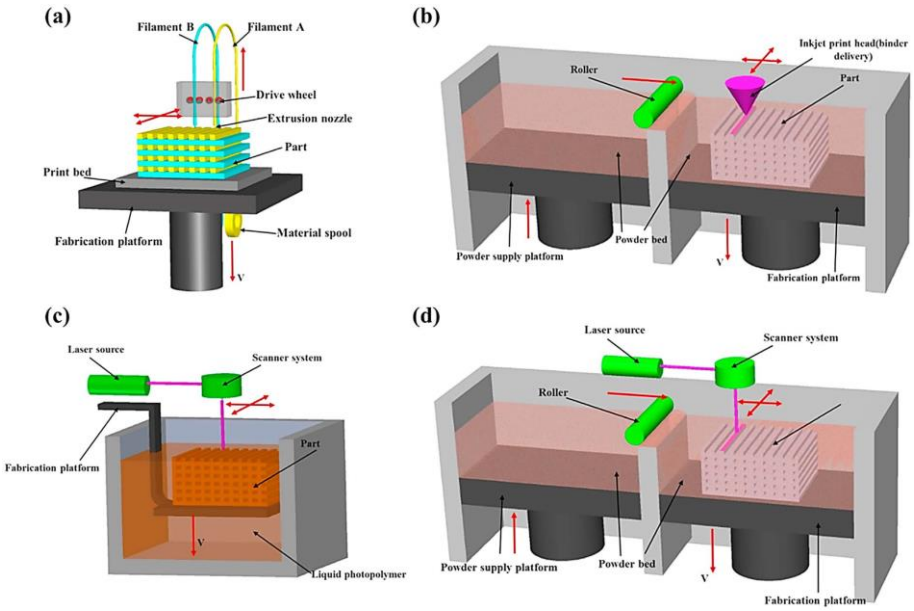

Figure 1: 3D printing approaches; (a) FDM, (b) Binder Jetting, (c) SLA and (d) Powder Bed Fusion.[25]

3.2. Lithography-based 3D-Printing

3.2.1. Stereolithography

It was Charles Hull, who experimented with UV curable polymers in the mid-1980s, using a scanning laser to do so. He was able to produce a solid 3D part by curing one layer on top of another, starting the stereolithographic revolution. Since then, a lot of different SLA-based approaches have been developed.

Based on the Greek terms *stereos* (hard, spatial) and *graphein* (writing), stereolithography has both a poetic and practical "ring" to it, nicely expressing its ability to tear down the boundaries of 3D-design. [26,27]

Compared to other AM technologies, SLA systems provide versatility in the scale of the produced parts (sub-µm to dm), while at the same time having a higher accuracy and resolution. As proven by e.g., Melchels et al. in 2010, SLA is able to produce parts of 200 cm whilst remaining an accuracy of 20 µm. With the ability to create objects with undercuts and internal cavities, very complex geometries, for example found in the human body, can be recreated.[28]

Looking at other AM technologies, they either lack the ability to create internal holes or have high temperature requirements on the raw material, making SLA one of the most precise and mild approaches in this field.[29]

Stereolithography is based on the process of photopolymerization, or light-induced polymerization, in order to create 3D objects in a layer-by-layer fashion. The process of SLA can be divided into two main categories, based on the type of light excitation and absorption, that lead to the polymerization: single-photon and multiple-photon approaches. In general, most systems use UV-light as their driving force, in order to converse photo-sensitive oligomers into cross-linked solid/gel-like polymeric networks. The reaction kinetics can be spatially and temporally controlled, for they purely rely on the effect of light manipulation. [30,31,32]

Single-photon SLA is named after its photoinitiation mechanism, which is driven by a single photon, that is being absorbed. Looking deeper into this method, there are two configurations, that are broadly applied.[31]

Firstly the "vector scan", also known as the laser-based approach and secondly the dynamic mask projection. The vector scan displaces a UV laser beam on a photosensitive slurry, leading to a localized polymerization process. [33]

As implied in the name mask projection, in the second type, a mask is used to define the image that is projected onto the liquid resin and therefore can create the whole solid layer at once, during a DLP process. This can be done by patterning of a large radiation beam by an array of micromirrors, also called Digital Micromirror Device™ (DMD), in order to achieve the wanted geometry of the layer. [34]

The simplest form of a multiphoton approach lies in two-photon systems. Here two separate laser beams are used and only if they intersect, photopolymerization will happen. This process happens, when the sequential or simultaneous absorption of two low-intensity photons leads to the excitation of the photosensitive resin, leaving a high-energy radical state behind and hereby starting the radical polymerization. This absorption mechanism is quadratically proportional to the incident light intensity, which differs to the linear dependence of the single-photon SLA.[35]

This also allows the laser to penetrate deep into the resin without causing polymerization at the surface, since photopolymerization only takes place in the center of the beam focus. Two-photon lithography has the highest resolution of all the SLA methods, achieving spatial resolutions below 100 nm.[33,36]

The physical objects are created by processing cross-sectional contours on top of another. In order to achieve a layer, one slices the 3D CAD file into its 2D layers and scans it in a photopolymer vat with a laser beam. Now one can again differentiate between two approaches, the “bottom-up” or the “top-down” set up, seen in Fig 2.

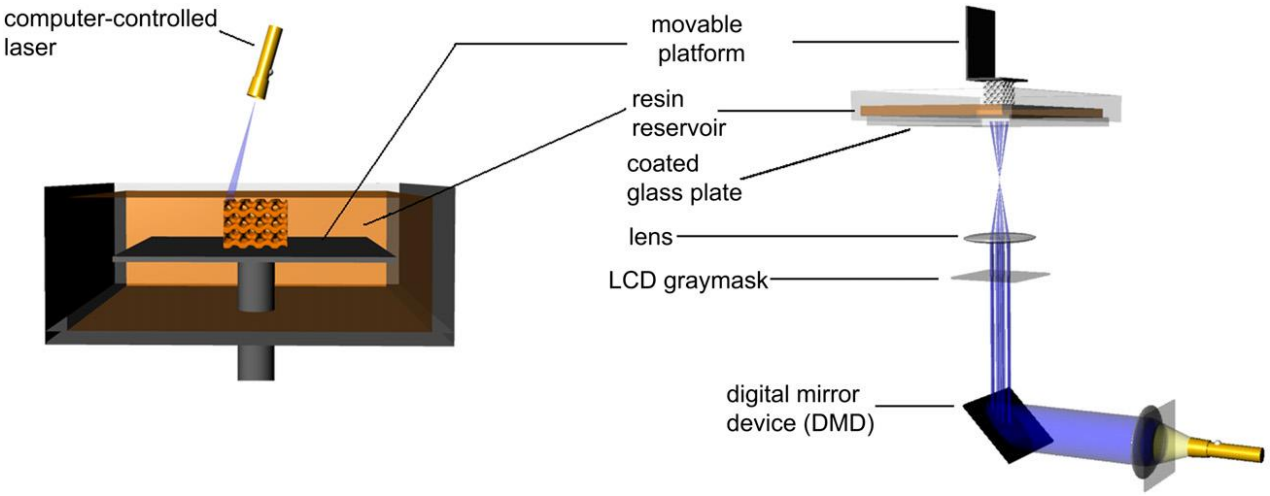

Figure 2: Two types of SLA: bottom-up approach (left) vs. top-down approach (right).[28]

In the bottom-up case, the building platform needs to be lowered deeper into the vat, after one layer was fully cured, so that a new layer of photopolymer can coat the surface of our object. Then one repeats this process until the CAD model was recreated. [37]

In the top-down approach, the light source is underneath the vat, which therefore must be transparent. A building platform is then lowered into the photopolymer filled vat, in the distance of one layer to the bottom of the vat. This results in a layer with a certain thickness that adheres to the building platform. The vat then tilts away from the cured layer and thereby detaches from it. Afterwards the building platform reaches a higher position, allowing new resin to coat the bottom of the vat. This process is repeated until the finished part is created. [38]

While it may seem like an inferior method, because the printed parts need to detach from in vat after every layer and therefore is subjected to higher mechanical forces, it actually has some advantages. The printed layer does not have to be coated, the illuminated surface is always smooth, fewer resin is required and lastly, oxygen inhibition is lower, as the illuminated areas are not subjected to the atmosphere. This method is also used in DLP systems. [28]

The processing of an object has a few key steps as its requirements: data input, part preparation, layer preparation and light scanning/projecting of the 2D contours. The data is represented by a STL-file (Standard Triangle Language), which holds the information of a CAD file or by reverse engineering data from e.g., a computer tomography image. The next step, the part preparation, involves providing support structures and the fitting machine parameters, which determine how the part is being processed in the SLA apparatus. The layer preparation can also be referred to as “slicing” and describes a step of translation, in which the CAD file is divided in, by machine parameters defined, 2D layers.

Typical parameters are: slurry layer thickness, light intensity, exposure time and scanning speeds. With this information, the SLA machine can be used to fabricate an object. [34,36]

Finally, the light scanning/projection describes the actual solidification of each slice. This concludes the building of an object. Afterwards, there can be a mix of different cleaning, post curing and finishing steps. [26]

In order to tend to specific needs, the SLA machine can be adapted. For highly viscous slurries it is necessary to have a blade spreading the resin, in order to have the same wet layer thickness in the whole vat. The blade itself and the movement of it need to be designed to fit the rheology of the slurry. [39]

3.2.2. Digital Light Processing

With the rise of high-performance UV-LEDs, new approaches in additive manufacturing could be achieved. UV-LEDs show a lot of advantages: they have a quick response time, energy conservation, high monochromaticity, long lifespan, are inexpensive and small build-volume. Most importantly, in combination with DMDs, one is able the illuminate and thereby polymerize a whole layer at once. These advantages led to LEDs being the main light source in digital light processing (DLP) systems. [40] DLP has its name from the digital mirror devices, that are used to selectively cure the light sensitive slurry. This leads to a wide array of advantages. It has a higher feature resolution compared to other AMTs, which improve well-defined pores and smooth surfaces. [41]

LEDs also make expensive lasers in SLA or heating chambers in powder bed fusion obsolete and with the use of special coating systems, especially in the top-down set up, the amount of required raw material is very small.[42]

In state-of-the-art systems, the operator can choose the light intensity (mW/cm^2) and the exposure time (s) based on the characteristics of the resin used. This is due to constant parameter light curing strategies that are being applied. Depending on the light engine or rather its DMD chip and its optics, the native resolution of the DLP may vary. With larger optics the exposure of larger building areas is possible, but this will reduce the resolution. In Z-axis the resolution depends more on the layer thickness and other printing parameters than on the light engine. [43]

In order to cure the slurry, the DMD dynamically creates images that are partially reflected on the surface of the vat. The chip of the DMD is assembled by an array of square micromirrors, which are able to tilt individually at +/- 12° along their diagonal via electrostatic forces. [44]

This leads to the ability to create light or dark pixels, when tilted towards or away from the photosensitive material. Furthermore, this allows for the realization of a binary bitmap of the geometrical information from the layers. The timing and order of the slices is determined by a sequence file. It is also possible to realize gray scales. This can be achieved when certain micromirrors are more frequently “on” then “off” for a brighter image (higher intensity) and the other way around for a darker image (lower intensity).[43,45]

3.2.3. Blueprinter 6 (BP6)

Improving the DLP approach, the Institute of Materials Science and Technology at TU Wien designed and built printers called “Blueprinter Systems”.

The one which was used in this work is the BP6, it was designed for filled slurries or other higher viscosity systems.

One addon is a heating system for the material vat. This feature helps to keep the suspension fluid, as a high solid load leads to a high viscosity. With the addition of a finely tuned tilting mechanism the stress on the built layers could be reduced. [42,45–47]

The second was the design and installation of a special coating blade, the amount of material needed for a single print job could be drastically reduced. The designed holes, seen in Figure 3, allow the overflow of slurry to be temporarily stored between the blades, accumulate there and distributed by the second blade. This creates a uniform slurry film on the vat in both movement direction. [42,48]

This leads to a very reproducible layer build-up and reduces the cleaning needed after the print, especially when printing complex and/or porous designs.[41,43,49]

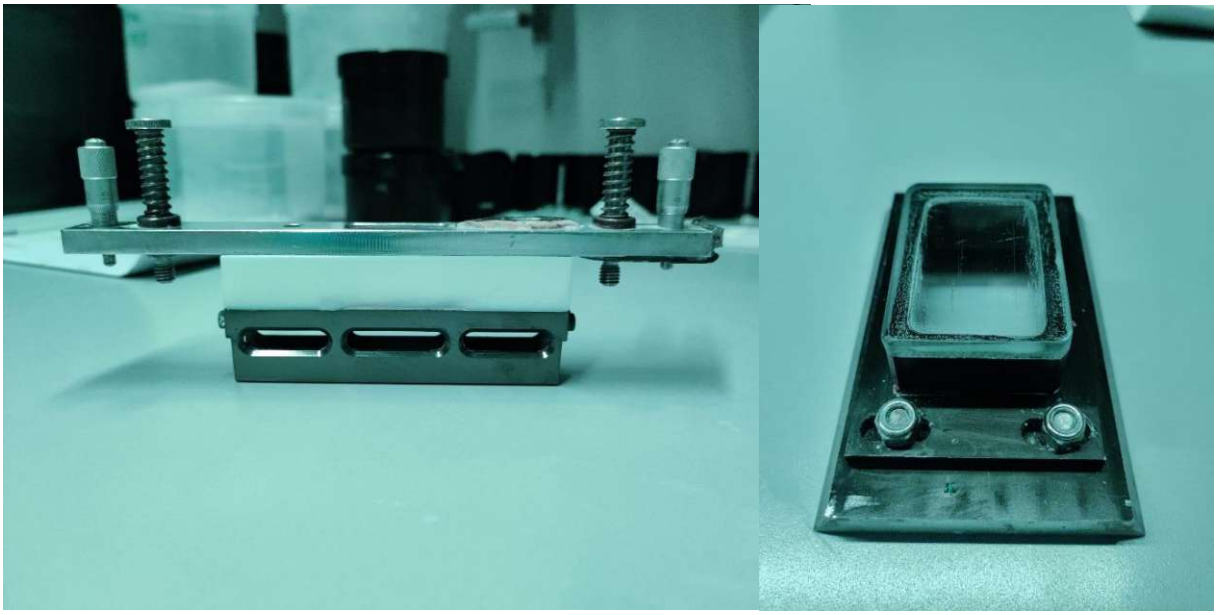

Figure 3: Left: Special double-edged coating blade, right: Building platform.

The building platform is designed with a transparent window, seen in Figure 3, through which a backlight which illuminates the first slurry layer to improve adhesion on the build platform. A light source with a wavelength of 460 nm is used for the backlight and the print. [41,50]

3.3. Photopolymerization

Polymerization is the process which transforms small molecules (monomers/oligomers) into larger ones, called polymers, that are composed of linked monomer units. It can be subdivided into chain-growth and step-growth polymerization.

Step-growth polymerization can be divided into condensation and addition reactions. In condensation reactions, a small molecule is formed as a byproduct, during polymer chain elongation. In polyaddition, the lengthening of the chain happens without the loss of a volatile molecule. However, in both cases the polymer forms in independent reaction steps of pairs of reactants, of any lengths, between their respective functional groups. This leads to a slower increase in average molar mass compared to chain-growth and thereby long chains only forming at high conversion, as can be seen in Fig. 4. [51,52]

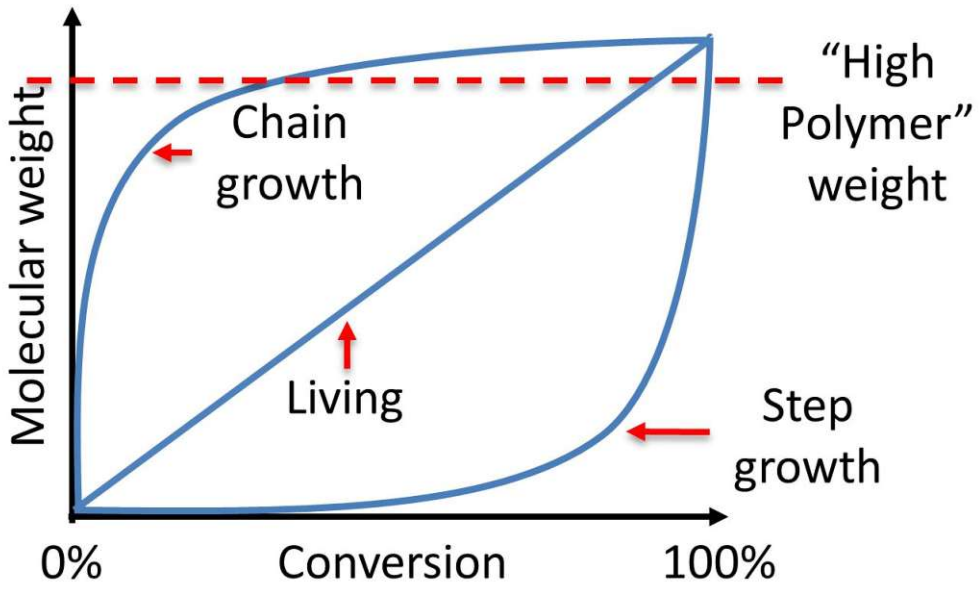

Figure 4: Distinction between chain and step growth.

In chain-growth, the chain-extension can only happen via the reaction of a monomer with the active group of the growing chain, where in step growth any two molecules in the mix can react with one another. After the reaction is initiated by the formation of the active center, the chain propagation is usually a very fast step. Also typical for this type of polymerization is the immediate formation of long chains, depicted in Fig. 4. [51,52]

With a vast array of possibilities at its disposal, stereolithography and DLP most commonly use radical photopolymerization techniques. This chain reaction uses a photochemical initiation step to create a free radical needed for chain-growth. Commonly used monomers, with high UV reactivity, are acrylates and methacrylates.[53]

The steps of radical photopolymerization are displayed in Figure 5 and are described as follows:

1) Initiation: The photoinitiator is exposed to light and decomposes into two radical moieties. Following the radical creation, the active site of the split photointitator is transferred to the monomer.
2) Propagation/Chain growth: The radical species of the monomer can attack a new monomer, creating a chain of monomer units.
3) Termination: This step describes the polymerization ending phenomena, for example caused by two radicals reacting with one another and in general with the formation of a covalent bond.
4) Transfer reaction: The radical site of the molecule is transferred without improving the progress of the reaction.

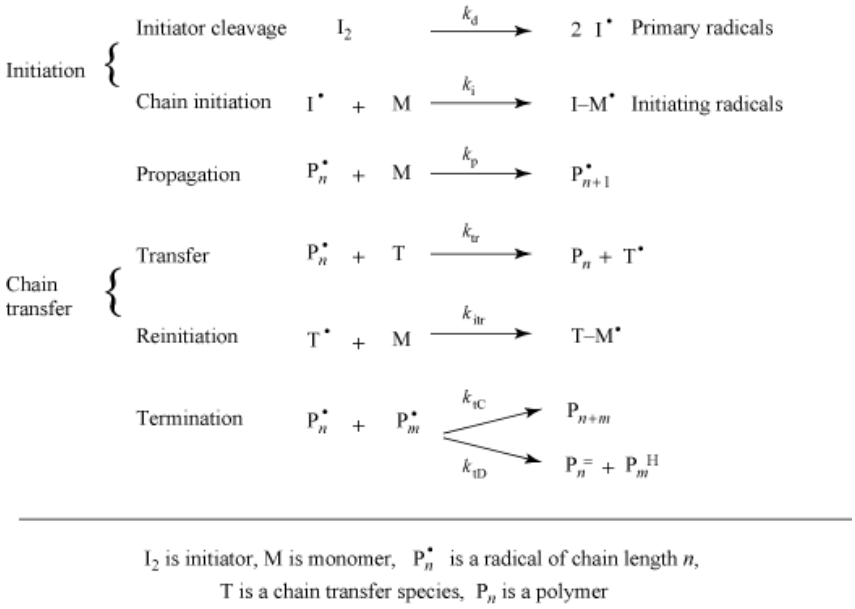

Figure 5: Reaction scheme of the radical photopolymerization. [53]

The diffusion of the reactive moiety is the driving factor for the propagation and termination step.

Photopolymerization offers several advantages compared to other methods: Spatiotemporal control, fast reaction kinetics and mild reactions conditions (e.g., room temperature (RT) or in physiological conditions). Photopolymer resins in 3D printing are usually a mix of different

components: photoinitiator, stabilizers, monofunctional monomers, multifunctional monomers, diluents, flexibilizers, etc.[54]

3.4. Photoinitiator

The photoinitiator plays a crucial role, it is dictating the polymerization efficiency of the curable system. In a first step, one needs to look at the absorption spectrum of the initiator. It should widely overlay with the irradiation profile of the systems light source. The two most common types of photoinitiators are radical and cationic. In the radical branch, one differentiates between type I and type II. Type I initiators function via unimolecular bond cleavage to form free radicals. Type II involve a bimolecular reaction to create the radicals. For radical photoinitiators the generation efficiency of the initiator to create radicals at these wavelengths is equally important Additionally, high shelf stability, low sensitivity to air or moisture should be considered. When used in life sciences, for example in tissue engineering, the photoinitiator should be biocompatible, which excludes several options, because of their cytotoxicity. [31,54]

The photoinitiator acts as a translator between the physical and chemical world. It takes up the physical energy of the illuminating light via absorption and turns it into chemical energy, when facilitating the formation of the reactive intermediates.[26]

This is done via chromophoric groups. When a photon is absorbed, the molecule is excited to the first singlet state. This is a high-energetic state with a short lifetime, as it can be transferred to more stable states via intersystem crossing (ISC), to the less energetic triplet state.

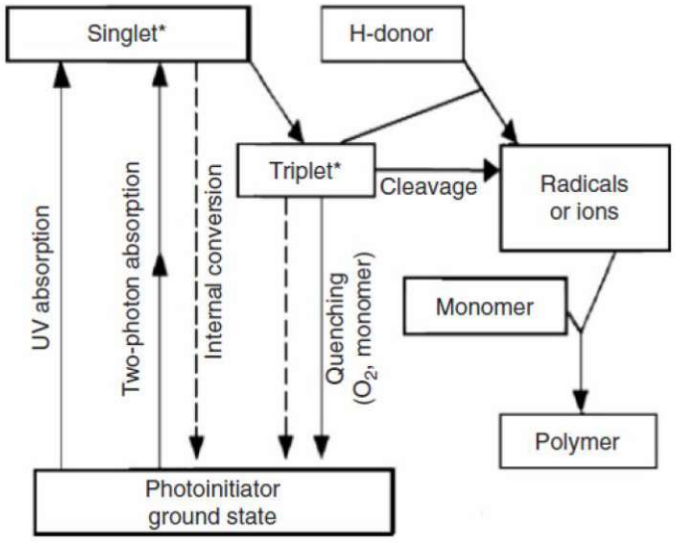

Figure 6: Different pathways of activation and deactivation for a photoinitiator. [55]

As shown in the Jablonski-type scheme in Fig. 6, there are many ways for the molecule to use its gained energy, two of which led towards the formation of radicals. In all other shown processes, the molecule returns to the ground state. (S_0, T_0)[56,57]

In this thesis acylgermanes are being used as initiators, specifically Ivocerin©. The benefit of this choice is, that the $n\pi^*$ - transition has a strongly pronounced red shift. The absorption maximum lies at 408 nm and the tail out goes up to 460 nm.[58–60]

As the chromophore is being destroyed during the absorption of long wavelengths, Ivocerin© is being bleached as part of the photoreaction. The mechanism of the radical formation in shown in scheme 1.[60]

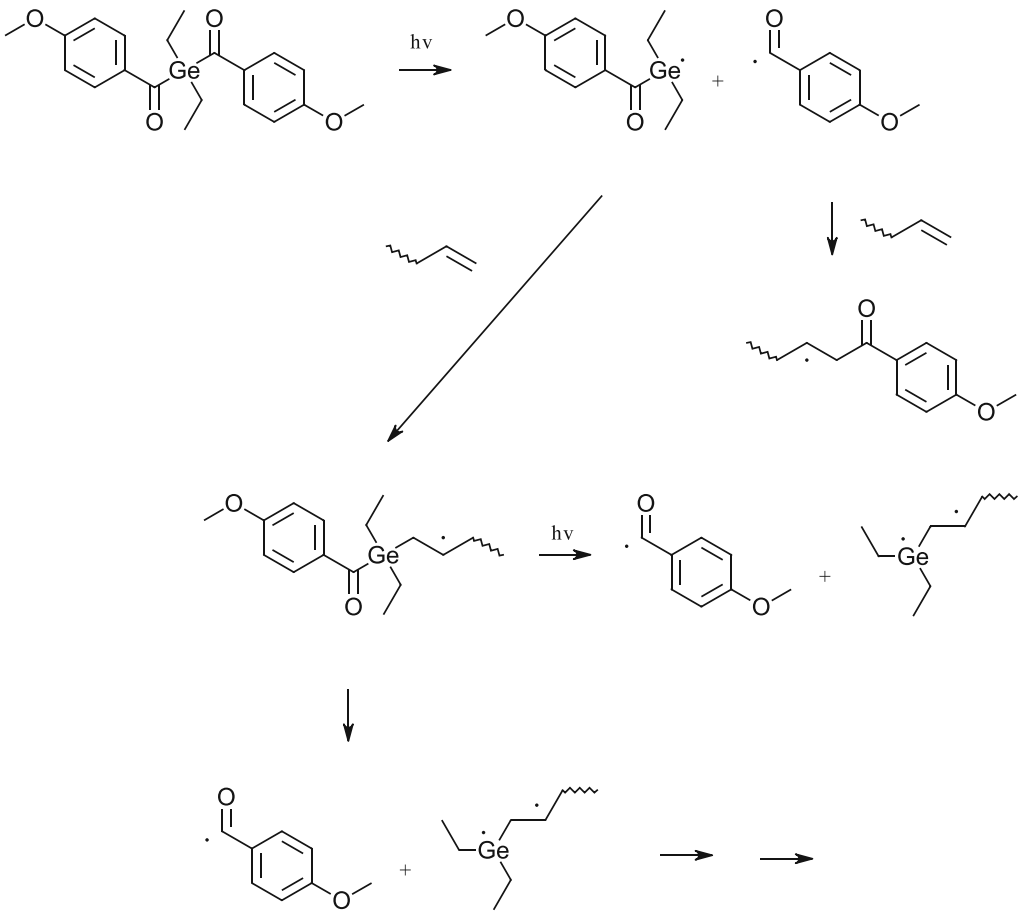

Scheme 1: Initiation mechanism of Ivocerin©

3.4.1. Curing Depth

It was Jacobs in 1992, that stated:

"In the transition of Stereo Lithography from an art to a science, it is natural that we should attempt to develop a model of the process. Although the mathematics may seem formidable to some readers, the physical model is actually quite simple."[61]

One of his conclusions was the equation of the working curve (equation 1), which was later even named after him.

Equation 1: Equation of Jacobs working curve

$$C_d = D_p * ln\left(\frac{E_{max}}{E_c}\right)$$

C_d ... $maximum\ curing\ depth$
D_p ... $penetration\ depth$
E_c ... $critical\ exposure$
E_{max} ... $maximum\ laser\ exposure$

It shows that:

- The cure depth C_d follows a natural logarithm of the maximum actinic laser/light exposure.
- The working curve, seen in figure 7, a semi-logarithmic plot of C_d vs ln(E_{max}), should be displayed in a straight-line relationship.
- The penetration depth of the resin (D_p) at the wavelength of the laser, is defined by the slope of the curve.
- The critical exposure E_c is precisely the intercept of the working curve and x-axis. This follows the mathematical conclusion of ln(1)=0, portraying the value of E_{max} at C_d=0.
- As D_p and E_c are strictly resin parameters, it shows, that within the limits of Jacob's model, the slope and intercept are independent of the laser parameters, such as power, spot size and scanning velocity.

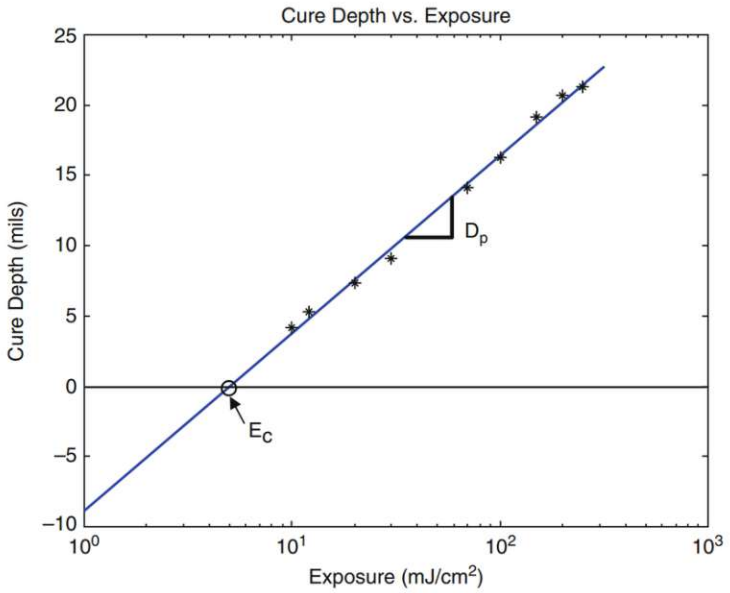

Figure 7: Example of the working curve.[62]

3.5. Ceramic Slurry

Griffith and Halloran were able to use the first highly loaded photocurable resin in SLA, to obtain a high-density ceramic part after sintering, in 1996. [63]

To produce ceramic parts via SLA, a photosensitive resin matrix is needed, in which the ceramic powder is dispersed. The resin contains the reactive monomers, a solvent, photoinitiator, absorbing agents and maybe other additives.

It is crucial that the right flow-ability is achieved for the process, usually low-viscosity curable resins are selected.[39,64] In order to gain a deagglomerated slurry with a low viscosity, a dispersing agent is added.[46]

Most photoinitiators are solid compounds, therefore it needs to be soluble in the organic matrix and most of time is solved in a diluent. The viscosity of the slurry strongly depends on the particle size and vol.-% solid load of the ceramic powder. One way to easily adjust it, is through the amount of diluent added. This is also possible with the addition of dispersants or a special rheology/viscosity additive.[50]

In addition to the parameters for photopolymerization mentioned in chapter 3.3 and the viscosity, a resin loaded with ceramic particles must be further adapted for 3D printing. The difference in refractive indices between the ceramic and the organic compounds strongly reduces the curing depth. To avoid “over-polymerization” dyes are added, that compete for the irradiated light and thereby reducing the over curing effect, caused by light scattering of the ceramic particles.[64]

As shown in Fig. 8, a ceramic slurry is a rather complex system, as all the different components need to work in perfect harmony, in order to provide ceramic parts with high quality resolution.

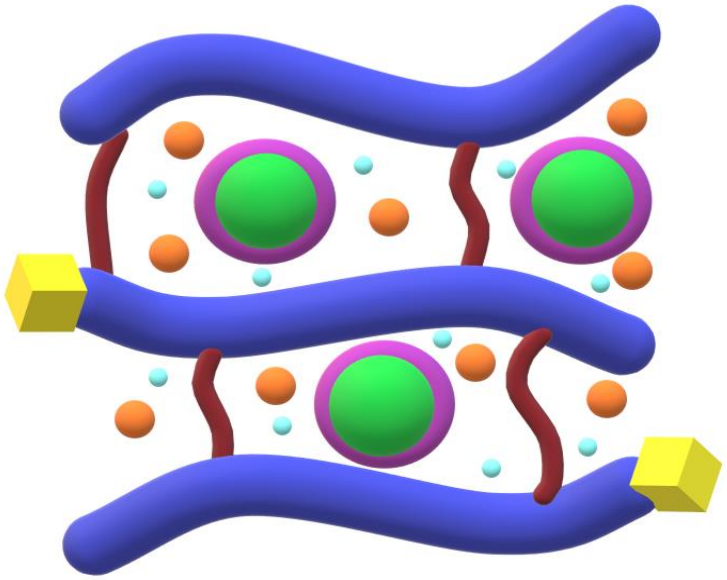

Figure 8: Scheme of a ceramic slurry[65] *– blue lines representing the polymer backbone, red lines the crosslinking units, green spheres the ceramic particles, pink doughnuts the dispersing agent, orange spheres the absorbing agent, the turquois spheres the and the yellow cubes the photointiator.*

The monomer mixture consists of difunctional methacrylate and trifunctional acrylates, acting as cross linker. Combined with the dispersing agent, the diluent and the photoinitiator. They build up the organic matrix of the ceramic green body. The powder particles are captured in the polymer network and thereby bound in the desired shape.[41]

In order to achieve good physical properties of the final part, a rather high amount of filler is needed, as with more ceramic powder the shrinkage is lower and thereby also the diffusion paths of the material during sintering. This allows for an easier path towards densely sintered materials, leading to better material properties. But with more ceramic particles the curing depth strongly reduces and the viscosity highly increases, which can lead to problems in the SLA process.[64]

3.5.1. Ceramic Matrix Composites (CMCs)

In order to achieve better mechanical properties, especially to increase fracture toughness of the final ceramic part, the CMCs approach is promising. Although both the fibers and the ceramic matrix are brittle, in composites they can improve fracture toughness. [66,67]

At present, one uses particles, fiber and whiskers to reinforce a ceramic matrix. Due to their high hardness und wear resistance, working with CMCs in traditional production is often challenging, therefore a higher interest in AM processing has developed in the last decade. This caused a development of a wide array of methods, ranging from direct ink writing and selective laser sintering, to SLA. [68,69–71]

When a fracture occurs in a CMCs material, an important toughening mechanism called fiber pulling-out. This leads to an energy transfer from the matrix onto the fibers. Therefore, energy dissipation over crack deflection, crack bridging and pull-out happen at the fiber-matrix-interface. In order to facilitate these mechanisms, the interface strength must be low enough. At the same time, it needs to be strong enough to allow the load transfer to happens, in order to have enough cohesion in transverse direction. [66,67]

Out of this knowledge two approaches were developed, the “weak interphase”- and the “weak matrix”-method. In the weak matrix approach, a porous material is used as the “grid material.” This leads to only a few local fiber-matrix contact points, which leads to easy debonding of the interface. In the weak interphase approach, one uses cleavable, porous and/or low toughness materials as fiber to achieve the same result. [72]

3.5.2. Aluminum oxide (Al_2O_3)

When talking about Al_2O_3 usually alpha-Al_2O_3 is implied, also referred to as corundum. This material has a high melting point, hardness, strength, wear resistance and chemical stability and therefore a wide array of application. From jewelry and optical applications, to high temperature or mechanical load bearding as structural ceramic, it truly has a broad field of application. Therefore, it has become one of the model ceramics in research.[73]

There are also some metastable modifications (γ, δ, η, κ, θ and ζ), deriving from different baking conditions of precursor materials (e.g., hydroxides). These can be transformed into corundum by high-temperature baking at 1000-1300°C.[73]

Al_2O_3 outperforms other oxides in hardness, while also having very high compressive strength. But its ultimate flexural und tensile strength as well as the fracture toughness are lower than other oxides (e.g. zirconia). Due to its biocompatibility, it is still a widely used material in medicine e.g., in bone replacement.[15,73]

Aluminum oxide can be subdivided as follows:

- Transition Al_2O_3: all metastable forms of alumina
- Calcined Al_2O_3 (baked alumina): describes a product out of thermal decomposition of aluminum hydroxides – brittle polycrystalline alpha-Al_2O_3
- Lamellar/Tabular/Sintered Al_2O_3: when sintering baked alumina above 1600°C – very pure polycrystalline material, classified by its particle size
- White fused Al_2O_3: Heat treatment over 2050°C – fine-grain microstructure with distinctly expressed crystal faces, allowing the production of single crystals
- Brown fused Al_2O_3: corundum with high amount of titanium, higher crack resistance
- High-purity Al_2O_3: at least 99,99 wt.% pure and small-size crystallites
- Sapphire: special trigonal crystal type, has different colors depending on the traces of metal ions in the lattice

Of special interest is high-purity Al_2O_3, as it has the best mechanical properties and thereby, it is most commonly used in research.[73]

3.5.3. Aluminum silicate

Aluminum silicate is a fibrous material derived from aluminum oxide and silicon dioxide. It is more a glassy solid solution than a chemical compound and is usually described by its wt.-% of Al_2O_3 and SiO_2. Generally, it is written as $xAl_2O_3*ySiO_2*zH_2O$, but there are a few more common examples:

- Al_2SiO_5: occurs naturally in different crystalline structures, in the minerals andalusite, kyanite and sillimanite.
- Kaolinite
- Metakaolinite
- Mullite

All these natural materials can be used to craft a high-performance ceramic material for different application. Most commonly these fibers are used for thermal insulation, but they are also very promising as a filler material in CMCs. [74–77]

3.5.4. Slurry Stabilization

It is important to know, that a dispersion is thermodynamically unstable. However, one can stabilize them kinetically for a long period of time. This is referred to as their shelf life.

"Dispersion stability refers to the ability of a dispersion to resist change in its properties over time." [78]

In order to understand how to stabilize a slurry, one must know the destabilization mechanisms. They can be divided in two categories:

1. Phenomena of migration: Phase separation occurs, because of variance in the densities of continuous and dispersed phase.
    - Creaming: Occurs with a less dense dispersed phase, forming a foamy top layer. (e.g., milk or soft drinks)
    - Sedimentation: When the continuous phase is less dense, the dispersed phase collects at the bottom. (e.g., paint, CMC slurry or …)
2. Phenomena of particle growth: The dispersed phase increases in size.
    - Reversable: The dispersed phase can change between a larger und smaller state. This is seen in Flocculation.
    - Irreversible: The dispersed phase grows to hardly separatable larger units. This is known as aggregation or coalescence.

3.6. Thermal post-processing

The thermal processing steps control the final properties of the ceramic part and vary strongly with the application of the product. In DLP, the printed parts are so-called green bodies und must undergo thermal post-processing to create the final ceramic part. These green bodies show lower density and mechanical properties, as the ceramic particles are dispersed in an organic matrix. The green part is cleaned in appropriate solvents to remove residual uncured monomers. Afterwards, the solvent is slowly dried off, leaving a partially porous part. This porosity helps during debinding, since the decomposition products can be removed more easily. After debinding, the part is sintered in order to obtain a dense ceramic microstructure. During sintering, the ceramic particles pack densely together, based on partial diffusion processes.[47]

To generate reproducible metal or ceramic parts, it is important to control the dimensional accuracy in the furnace and the following shrinkage.

In lithography-based ceramic manufacturing, the most important thermal post-processing methods are thermal debinding and sintering.

3.6.1. Debinding

As described by German and Bose in 1997, debinding refers to the process of binder removal in injected parts. It is a thermal process producing the so-called brown parts from green parts To avoid quality loss by cracking, distortion, blistering or contamination, it is of great importance, that debinding is performed very carefully. [79,80]

In SLA processing, debinding describes the process of decomposing the organic matrix. This involves not only the structure giving polymers, but also the photoinitiator, the diluent and the additives, such as the dispersing agent. This is described by Ani in 2014, by the two-stage debinding, where in a first stage the "support components" (e.g. diluent) and in a second step the "backbone components" (polymer network components) are removed.[81]

But before debinding itself happens, the part undergoes a drying step. From the start of the heating process, until around 120°C, volatile molecules, such as solvents or other non-reactive compounds, evaporate. This creates open pores in the structure of the green part, these will later guide the components of higher molecular weight, when exiting the structure. In order to minimize internal stress, it is important to choose low heating rates in temperature areas of high weight loss. This allows for better diffusion of the decomposed diluents, which on the ladder, causes better diffusion and evaporation of the pyrolyzed polymers.[42,47]

During the heating period, until about 400°C, the polymer networks are completely destroyed and removed. The brown part is created, resembling a loosely packed ceramic structure, only held together by its cohesive forces.

As this process is a very time consuming one, a lot of research went into different debinding techniques, including thermal, wicking, solvent, evaporation and catalytic debinding. When working with oxide ceramic green parts, one usually works thermally in common oxygen furnaces, where the organic compounds are combusted.[82,83]

In order to find out the right parameters of this processes, one must consider the chemical composition of the binders, the geometrical dimensions of the green parts and the slurry's solid loading. All of these variables change the weight and dimensional shrinkage. In order to have a clearer picture of these phenomena, thermogravimetric (TGA) and thermomechanical analysis (TMA) can be conducted. With the gained information, suitable temperature profiles can be generated.[84,85]

The temperature ranges of higher mass loss or dimensional change can be handled with isothermal plateaus, to provide better diffusion without causing extra internal stress. Here, the "surface-to-volume ratio" comes into play. It describes, that longer diffusion paths and voluminous parts lead to longer isothermal stages and slower heating rates, in order for flawless debinding to occur.[84,85]

3.6.2. Sintering

In order to obtain dense materials, a process called sintering is applied. Ceramic or/and metal powders are compacted by the use of thermal energy. Looking at the four basic elements of material science, structure/composition, performance, property and processing/synthesis, sintering has its place in synthesis/processing and has become a crucial interest in research. [86,87]

Different to other processing methods, sintering is not independent to the other methods used in the production chain. The shape of the final object, for example, can change the sintering conditions drastically. However, also the sintering step by itself can change the properties of the final material e.g., the microstructure. [79]

The aim is to control the sintered density, grain size and distribution and size of all phases including pores, simply by the sintering parameters.

Sintering can be categorized into two major groups: solid state sintering (SSS) and liquid phase sintering (LPS). When the densification of the powder compact solely happens in the solid state, one speaks of SSS. If the sintering temperature leads to a liquid phase, LPS occurs. As shown in Fig. 9, there are special cases, called viscous flow sintering and transient liquid phase sintering.

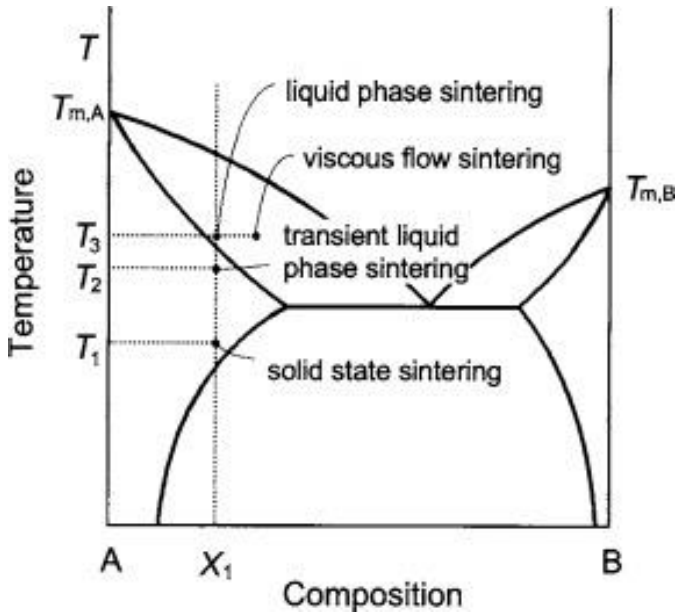

Figure 9: Phase diagram of the different sintering types of a two component system.[87]

Viscous flow sintering applies when the entire compaction is facilitated by the viscous flow of the grain-liquid mixture. This means not causing any shape change of the grain. Transient liquid phase sintering on the other hand, is when a liquid phase occurs, but disappears as the process continues and has no influence on the densification, which happens in the solid state.

The driving force of this phenomena, depicted in Fig. 10, lies in reducing the total interfacial energy. The total interfacial energy consists of the change in interfacial energy portrayed by densification and the change in interfacial area based on grain coarsening/growth. When considering sintering, there are two different variables behind the process. On the one hand process variables and on the other hand material variables.

The material variables are determined by the influence on the compressibility and sinterability of the powder. They compose of the shape, size, size distribution of the powder, its chemical composition and the degree of agglomeration, to name a few. Here one word is of utter most importance: homogeneity. The more the used powders vary, the harder a suitable sintering process is to find.

The process variables are more or less all thermodynamic parameters, such as temperature, pressure, time, heating and cooling rate and the atmosphere.[87]

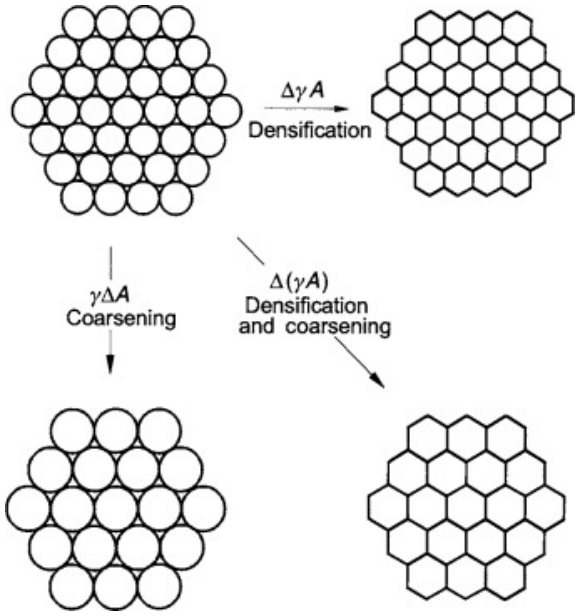

Figure 10: Scheme of the different phenomena while sintering.[87]

4. Experimental Part

4.1. Chemicals

In this chapter all used chemicals are listed and sorted by their type, which correlates to their field of application.

a) Polymers:
   - Diurethane Dimetharylate (UDMA, Sigma Aldirch©)
   - Propoxylated Trimethylolpropane Triacrylate (Sartomer SR492, Arkema Group)

b) Solvent:
   - Polypropylene Glycol (PPG425, MW = 425 g/mol, Sigma Aldrich©)
   - Isopropanol (70%, Carl Roth)
   - Isopropanol (99,9%, Sigma Aldrich)

c) Dispersing Agents:
   - Disperbyk(c)109 (BYK)
   - Disperbyk(c)111 (BYK)
   - Disperbyk(c)118 (BYK)
   - Disperbyk(c)180 (BYK)
   - Disperbyk(c)2152 (BYK)
   - Disperbyk(c)2155 (BYK)
   - Disperbyk(c)2157(BYK)

d) Photoinitator: Ivocerin© (K69, Ivoclar Vivadent Inc.)

e) Absorbent: Sudan Yellow©-117 (BASF)

f) Ceramic Fillers:
   - Aluminum Oxide (TM-DAR, KRAHN Chemie GmbH)
   - Aluminum Silicate (Fiberfrax©-B102, Unifrax Co.)

g) Lubricant:
   - DP-Lubricant Blue (Struers)

h) Grinding Suspension:
   - DP-Suspension P, 9 µm (Struers)
   - DP-Suspension P, 3 µm (Struers)
   - DP-Suspension P, 1 µm (Struers)

i) Warm Embedding Agent:
   - PolyFast (Cloeren Technology GmbH)

4.2. Devices

Chapter 4.2 introduces all devices used during this thesis.

a) Blueprinter 6 (BP6, Institute of Materials Science and Technology at TU Wien)
b) SpeedMixer™
    - DAC 150.1 FVZ (Hauschild)
    - DAC 80.2 VAD-P (Hauschild)
c) Ultrasonic Generator (Sonifier 450, Branson)
d) Ultrasonic Bath (Emmi-40HC, EMAG Technologies Inc.)
e) Furnace:
    - FED 400 (Binder)
    - HTC 08/16 (Nabertherm)
    - HRF 7/22 (Carbolite Ltd.)
f) Furnace Controller:
    - P 320 (Nabertherm)
    - Eurotherm 3508 (Carbolite Ltd.)
g) Spatial Measurement Tools
    - IP 67 (Kroeplin)
    - Caliper (RND Lab)
    - Ruler
h) Rheology
    - MCR 300 (Anton Paar)
i) Thermal Analysis
    - Toledo TGA/DSC1 (Mettler)
    - TMA-Q400 (TA-Instruments)
j) Mechanical Testing
    - Z050 (Zwick Roell)
    - Z250 (Zwick Roell)
k) Scales
    - LE225D (Sartorius AG)
    - CARAT SCALE GK1203 (Sartorius AG)
l) Grinding and Polishing plates
    - Piano 220

- Allegro
- Largo
- Nap
- Chem

m) Grinding tools
    - TegraPol-31 (Struers)
    - TegraForce-5 (Struers)
    - Tegradoser-5 (Struers)

n) Embedment device
    - CitoPress-20 (Struers)

4.3. Optimization of the Slurry

4.3.1. Slurry Composition

As a starting point for a comparative ceramic part the slurry composition of the PhD thesis of Simon Gruber was used. A mix of reactive monomers, a solvent, a reactive photoinitiator, an absorber and a dispersant compose the organic matrix, called the master batch.

UDMA and TMPPTOA were used as the respective photocurable monomers. As seen in scheme 2, based on the terminal reactive groups, UDMA is mainly used to form the main chain of the polymer network.

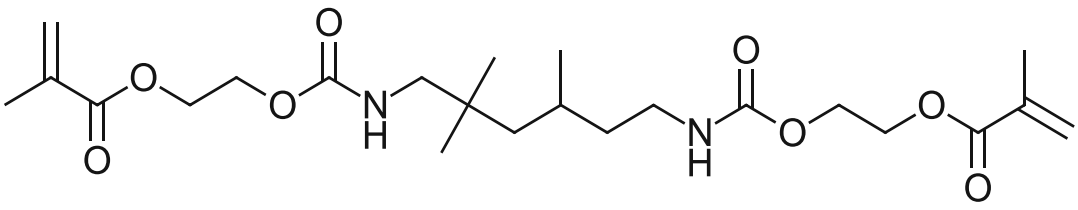

Scheme 2: diurethane dimetharcylate

Acylates, in general, form a secondary radical species, thereby being more reactive than the corresponding methacrylate. The methacrylate forms stable tertiary radicals, hence hindering further polymerization.

The acrylate, TMPPTOA, acts as the crosslinker, this stems from its trifunctional nature depicted in scheme 3, allowing for the encapsulation of the ceramic particles in the polymer network.

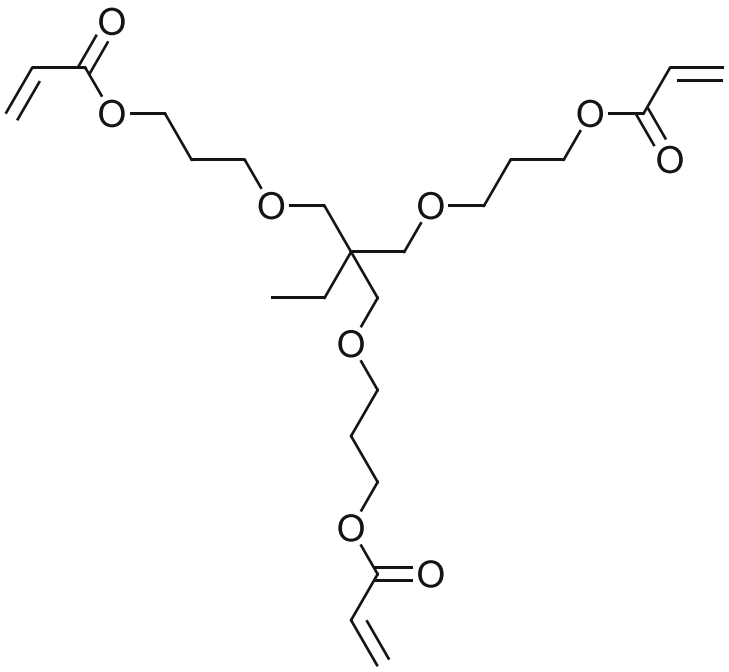

Scheme 3: TMPPTOA

Polypropylene glycol, as the solvent, had the main function to regulate the viscosity of the slurry. It was used with a molecular weight of 425 g/mol and can be seen in scheme 4.[49]

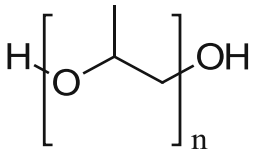

Scheme 4: Polypropylene glycol

The dispersing agent either enables the mixture in general or helps with the process leading to a suitable dispersion. Suitable meaning dispersed homogeneously with as little as possible agglomeration and shelf stable for a couple of days. They also regulate the viscosity and can be shear thinning or thickening. In the case of Disperbyk-2155, it shows a very strong shear thinning.[44]

Ivocerin©, depicted in scheme 5, was used, because it forms four radical sites when irradiated with 460 nm blue light. Thereby, having very fast and potent initiation at the provided wavelength of the LEDs.[88]

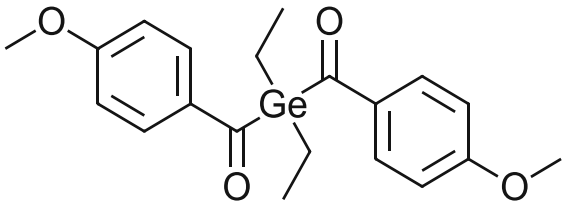

Scheme 5: Ivocerin© or [(p-Anisoyl)bis(ethyl)germyl](p-methoxyphenyl)methanone according to IUPAC

In order to cope with the light scattering of the fillers an absorbent was added. Based on the PhD thesis of Gruber[65], Sudan Yellow©-117 from BASF was chosen, leading to less over-polymerization and while remaining a similar curing depth.

Al_2O_3 particles acted as the solid loading of the slurry and after sintering as the matrix of the CMC part, seen in table 1.

The ceramic fibers acted as an additional solid loading and as the reinforcement of the Al_2O_3 matrix, after sintering.

Table 1: Comparison of the base formulation and new formulation

Materials	**Base formulation (g)**	**new formulation (g)**
Al_2O_3	78.45	77,67
Fiberfrax-B102	0	0,78
Ivocerin	0.04	0.04
Disperbyk-(111 or 2155)	0.74	0
UDMA	6.66	6.66
TMPPTOA	6.24	6.24
PPG425	7.86	7.86
Sudan Yellow	0.002	0.002

When comparing the compositions, one can recognize, that no dispersant was added in the master batch. While there was no dispersing agent added to the master batch, the ceramic fillers were pre-dispersed with a 5 wt.-% of Disperbyk-2155.

4.3.2. Dispersing the Filler Materials

The main reason for optimization of the slurry composition was the dispersion of the fillers. Before dispersing the aluminum silicate fibers, the Al_2O_3 particles were dispersed in separate trails.

As discussed in chapter 4.3.1 the master batch of the old recipe still contained the dispersant and was mixed before the ceramic particles were added in three batches and the slurry was mixed in the SpeedMixer™. This led to poor dispersion, of agglomerate size >100 µm and therefor needed optimization.

The principle of the speed-mixing stems from a double rotation of the container, also known as dual asymmetric centrifuge.[41]

In order to improve on this result, different approaches were evaluated:

- Ultrasonic horn
- Ultrasonic bath
- Milling in the SpeedMixer™
- Milling at the roller mill
- Predispersing

4.3.2.1. Predispersing

In a first approach, the Al_2O_3 and the fibers were predispersed separately, simply in a mixing cup on a magnetic stirrer for 24h.

In a second approach, all of the ceramics were jointly predispersed, still using the magnetic stirrer for 24h.

Finally, a total amount of 40g, composed of ceramic powder, fibers, and the dispersant were milled in 65 mL isopropanol (99,9%) on a roller mill. Afterwards, the solvent was removed via evaporation in the FED 400 furnace at 75°C for 24 h. The dry powder was sieved and used as described in chapter 5.1.2. This way it is assured, that the maximum amount of dispersant is coating every ceramic particle, leading to a more evenly dispersed slurry.

This final approach showed the least amount of agglomerates, and therefore was used for every slurry from this point on for all further investigations.

As the dispersion of the fibers did not show the wanted agglomerate size of under 30 µm, different dispersants, as listed in Table 2, were investigated.

Before any further experiments were conducted, the data sheets of the additives were scanned for its applications. If it was applicable for inorganic pigments and titanium dioxide, it was considered for further experiments. The second limitation was the solubility in the master batch. Therefore, three drops of additive were added to 10 drops of master batch and then stirred by shaking and via a vortex device.

Table 2: List of tested dispersants

Name	Applicable for TiO2/Pigments	Optical Abnormalities	Soluble in Master Batch
Disperbyk©-109	Yes	Clear & Colorless	Yes
Disperbyk©-111	Yes	Clear & Colorless	Yes
Disperbyk©-118	Yes	Clear & Coloration	Yes
Disperbyk©-180	Yes	Clear & Colorless	Yes
Disperbyk©-2030	No	-	-
Disperbyk©-2152	Yes	Clear & Coloration	Yes
Disperbyk©-2155	Yes	Clear & Colorless	Yes
Disperbyk©-2157	Yes	Clear & Colorless	No
Rheobyk©-410	No	-	-
Rheobyk©-7411	No	-	-
Rheobyk©-7410ET	No	-	-
Rheobyk©-7420ES	No	-	-
Bykjet©-9152	No	-	-
Byk©-W969	No	-	-

This led Disperbyk© 109, 111, 118, 180, 2152 and 2155 to be cleared for further testing. For all these dispersants, the concentrations 1, 3 and 5 wt.-% were investigated. In order, to also test if one was especially capable in dispersing fiber, the fiber content was varied. As the fibers seemed rather hard to disperse, 1, 2.5 and 5 wt.-% were chosen for these experiments. These mixtures, were mixed with a magnetic stirrer.

After optical analysis, it was clear, that 111, 118 and 2155 showed the best results. These dispersants were also tested on the roller mill.

4.3.3. Slurry preparation

The preparation of the slurry was done as follows; first the master batch was prepared - all organic components were added to a special mixing cup and mixed with the SpeedMixer™ for a minute at 800 rpm.

When working with light-absorber and/or the photoinitiator, the mixture was additionally stirred over night with a magnetic stirring unit.

Afterwards the master batch and the filler were mixed to the slurry according to Table 3.

The ceramic powder was added in three steps, this allows the shearing forces to have their biggest effect. It was also important, that the remaining masterbatch was added stepwise, in order to assure homogeneous mixture, while keeping the shearing forces at its highest.

The final process is portrayed in Table 3.

Table 3: Preparation procedure of the ceramic slurry

Steps (for 100g Slurry)	Master Batch (%*)	Master Batch (g)	Ceramics (%*)	Ceramics (g)	Mixing Speed (rpm)	Mixing Time (s)
1	15	3.23	33	26.15	1600	60
2	15	3.23	33	26.15	1600	60
3	15	3.23	33	26.15	1600	60
4	5	1.08			1800 3500	60 30
5	5	1.08			1800 3500	60 30
6	5	1.08			1800 3500	60 30
7	5	1.08			1800 3500	60 30
8	5	1.08			1800 3500	60 30
9	5	1.08			1800 3500	60 30
10	5	1.08			1800 3500	60 30
11	5	1.08			1800 3500	60 30
12	5	1.08			1800 3500	60 30
13	10	2.17			1800 3500	60 30

*the % refers to the total amount master batch or ceramics used, not to the total amount of slurry created

4.3.4. Optical Analysis

4.3.4.1. Transmission Light Microscope

To measure the size of agglomerates a transmission light microscope (Fig. 12) was used. It was kindly provided by the working group of Prof. Liska of the Institute of Applied Synthesis of the TU Wien. This microscope was able to depict the agglomerates and additionally take pictures with an attached camera.

After speedmixing, the slurry was degassed, so the integrated air bubbles did not obscure the dispersion, when looked at under the microscope. Afterwards, with the help of a small plastic spatula, a thin layer was brushed on top of a glass slide. Subsequently, a coverslip was placed over the slurry and carefully press on the slurry with the back of a cable tie to create an even surface.

In order to know how big a pixel was, a glass slide with a scale bar etched into it was used. At least three pictures were taken from every sample.

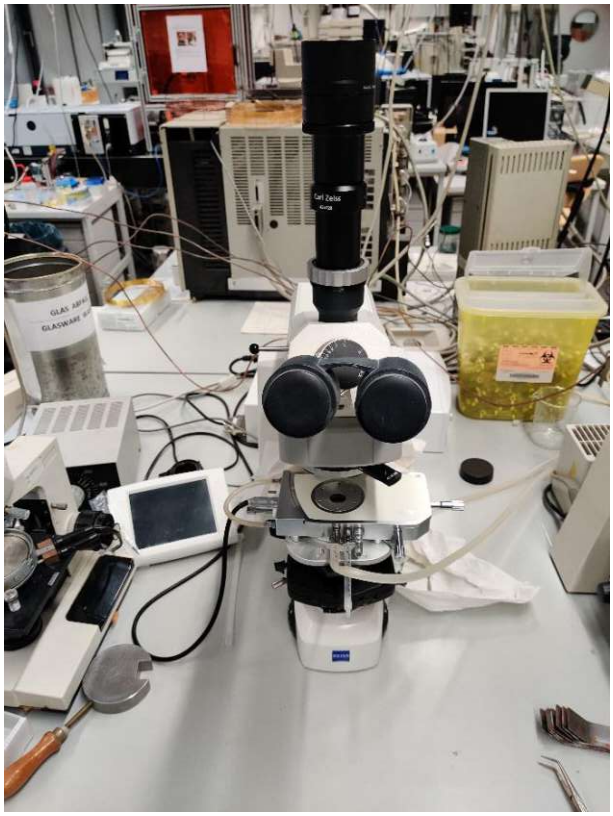

Figure 11: Transmission microscope used for optical analysis.

The pictures were edited in FIJI, a software for image analysis. All images were transferred into 8-bit images. Then the contrast and brightness were adjusted based on an integrated algorithm. Afterwards, the image was scaled in µm and a scale bar was added. This process is shown in Fig. 12, it starts with the raw image and ends with finished edit.

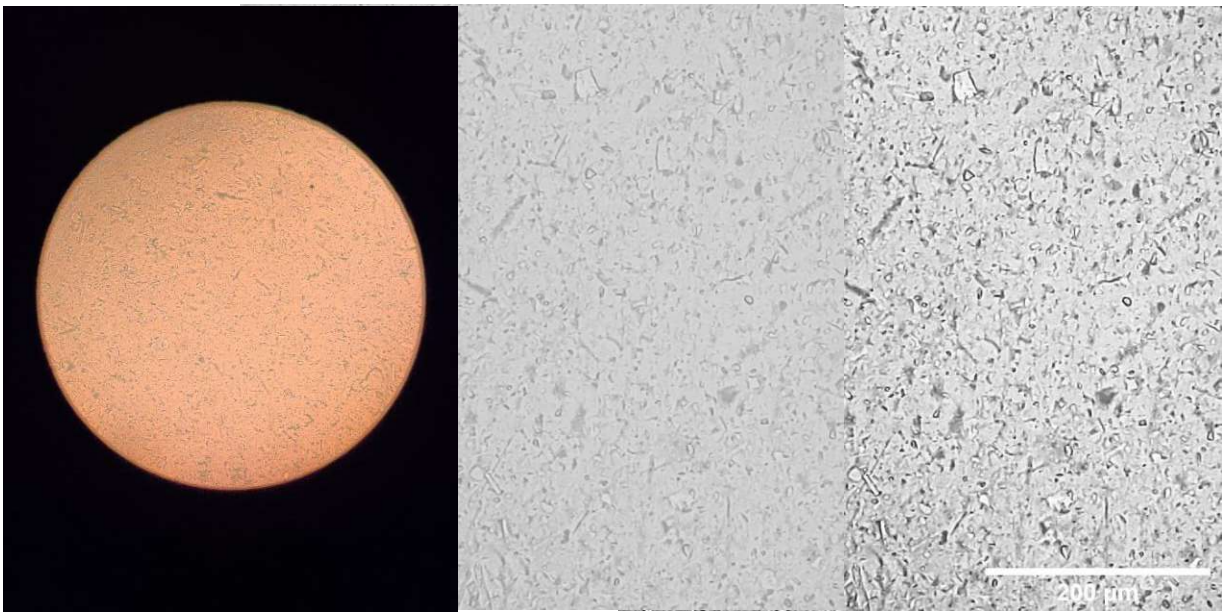

Figure 12: Progress of the editing process; left raw image, middle transferred and cut, right finished image with added scale bar.

In order to compare the different samples, any bigger agglomerates were now measured and additionally the number of agglomerates compared.

4.3.4.2. Grind Gauge

Additionally, to the light microscope, the agglomeration size was tested for slurries without the fibers using a grind gage, depicted in Fig. 15. For this, an equal drop of slurry was placed on the two tracks and covered with a special coating blade. The achieved particle size could be read from the scale bar on the side of the measuring block.

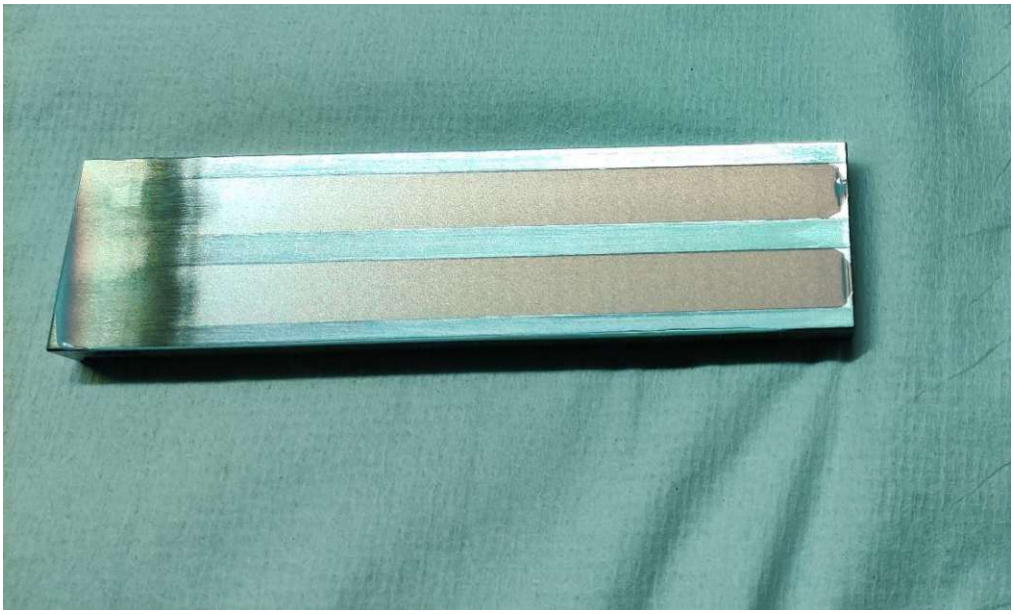

Figure 13: Grind Gauge coated with a thin layer of slurry.

4.3.4.3. Scanning Electron Microscope

The last optical analysis was done on a scanning electron microscope (SEM). With this technique it was investigated, if the fibers could be detected after sintering. Additionally, the orientation of the fibers was analyzed. For this analysis, several samples were sintered at different temperatures.

Firstly, the cylinder used for the density determination and shrinkage evaluation was embedded in a conductive resin. This allowed for better handling during the grinding and polishing process.

As described in Table 4, the samples underwent a predesigned grinding and polishing profile at the TegraPol-31.

Table 4: Grinding and Polishing Profile

Base	**Suspension**	**Lubricant**	**Time (min)**
Piano 220	-	Water	3
Allegro	DP-P 9 µm	Blue*	4
Largo	DP-P 3 µm	Blue	8
Nap	DP-P 1 µm	Blue	8
Chem	OP-U		4

*Blue referrers to DP-Lubricant Blue by Struers

Each step was evaluated under a light microscope before the subsequent step was started. The sample was put in an ultrasonic bath for 30 s and was rinsed with water afterwards. After drying it with isopropanol and a hair dryer, it was investigated under the microscope.

This way a smooth surface, a couple of 100 µm inside the printed part, was generated.

In addition to these cuts, also the ceramic powder, breakage of the debinding and sintering process and the fracture surface of the biaxial platelets were investigated. In order to make the fibers and the matrix visible, the samples were sputtered with gold for 30 s at an amperage of 1,1 A. The samples were subsequently placed on a special sample table, seen in Fig. 14 and placed in the SEM under vacuum.

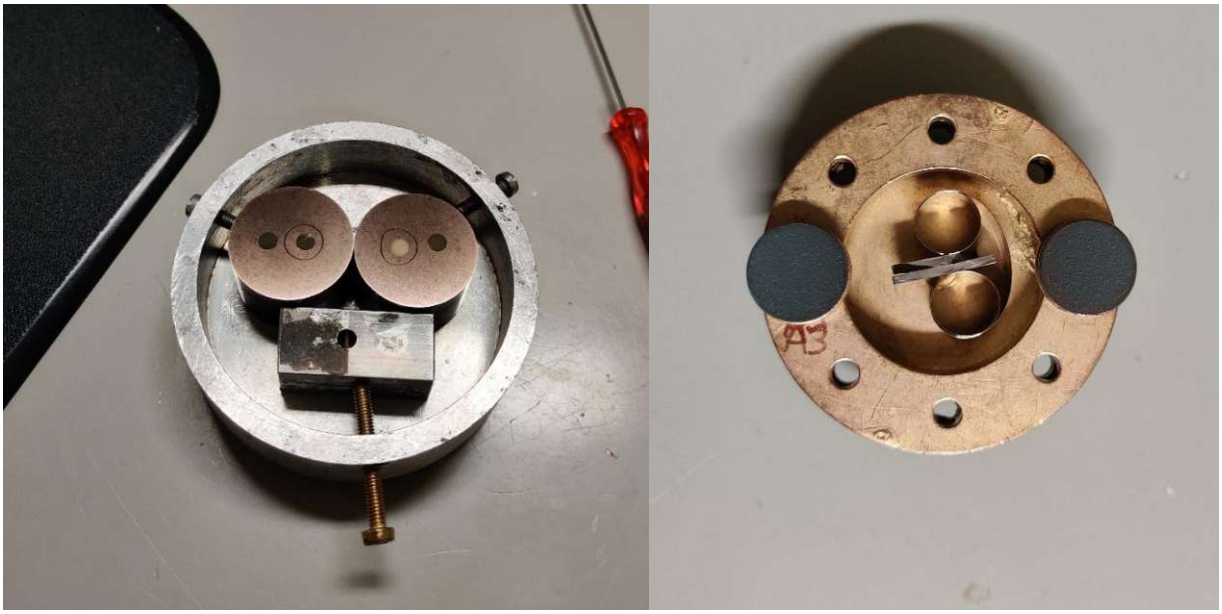

Figure 14: SEM Sample Table; right with the embedded cylindric samples and left with the powders and the fracture surface from biaxial bending.

For the SEM images, the current could be adjusted, every measurement was started with 20 kV and scanned via the TV setting or a bigger spot size. When the desired position was found, the settings were switch to a smaller spot size, especially when working with magnifications higher than 1000x and when working with the backscattered electron (BSE) detector. Then the focus was readjusted and a frozen image was saved, in this frozen image a scale bar and measurements could be applied.

4.3.5. Rheology Measurements

The rheology tests measure the flow of a material whilst applying a certain force to it. This was used to determine, which slurries are suitable for 3D-printing. In order to meet this criterion, the viscosity at a shear rate of 20 s^{-1} needed to be below 20 Pa*s or even better below 15 Pa*s. This allows a smooth coating of the material vat surface, while the abundant slurry can easily flow into the storage of the double-edged blade.[65]

It was important to use a rheometer, not a viscometer, because the slurries could not be described by one single viscosity, but rather in tandem with other values. For this, they needed to be screened by an array of parameters, like temperature, shear rate or oscillation, as the viscosity changes alongside with them.

All rheology measurements were conducted with the same parameters. To make the results even more comparable, the profile was composed of three intervals. In the first one, the shear rate was kept on 5 s^{-1} for a duration of 0.5 min. The second interval was a dwell time of 2 min without an applied shear rate. Then the measurement started, collecting 35 data points during a shear rate change from 0.01 to 500 1/s. For each measuring point, the information of the shear rate (s^{-1}), the shear stress (Pa), the viscosity (Pa*s), the rotation speed (min^{-1}) and the torque (µNm) were collected. Each slurry was measured three times at room temperature, this allowed an average value and standard deviation to be calculated.

The experiments were done with the plate-to-plate set up (CP25-1 SN18564) and data analysis was done with the Rheoplus V3.40 software of Anton Paar.

The obtained data was used to plot the dynamic viscosity (Pa*s) against the apparent shear rate (s^{-1}).

4.4. Optimization of the Print

4.4.1. Adjusting the Printer

The printer used in this diploma thesis was the Blueprinter 6 (BP6), displayed in Fig. 15. With this printer, a wall thickness of 4 pixels could be achieved, while having a building resolution of 25x25x25 µm, leading to a minimum wall thickness of 0,1mm.[50]

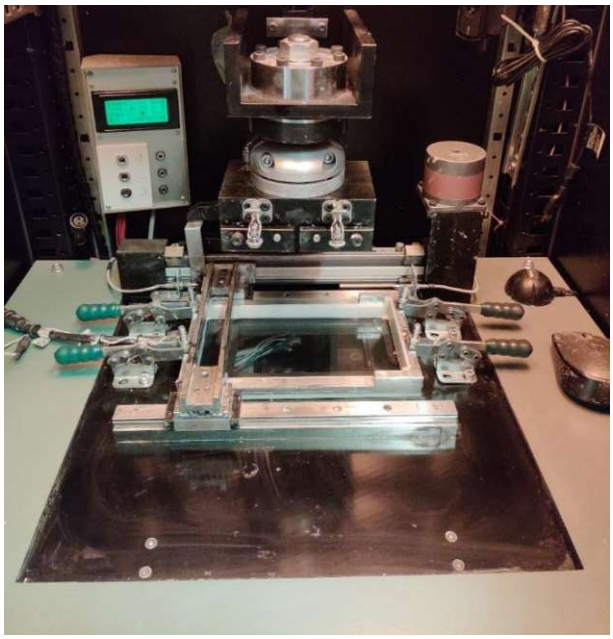

Figure 15: Blueprinter 6 with installed material vat.

Before the printing process could start, a couple of hardware and software preparation had to be fine-tuned:

- Focusing the surface
- Adjusting for parallelism
- Alignment of the building stage and the blade
- Adjusting the wet layer thickness
- Creating the building job

To make sure, that the light source illuminates every pixel with the same resolution, the focus of the light engine had to be tuned in. Three millimeter-screws inside the housing of the SLA system were used for that. At the same time a camera was put on the material vat and the resolution of the pixel pattern was checked.

After the coating blade was installed, the slurry was be poured in. To avoid oxygen inhibition and defects due to uncured spots in the build, the slurry was degassed under vacuum in the Speedmixer^{TM}, at 800 rpm and 40 mbar.

One very important task, was the parallelism adjustment of the building platform to the vat. For this the ball joint of the "head" of the printer had to be loosened. In the loose state, the building platform was then lowered onto the material vat carefully. When the pressure sensor had its first spike, the screws were tightened again. This was a very fragile moment in the printer adjustment, because when one applied to much pressure for too long, the FEP-Foil of the material vat could be damaged. After the screws were tight, the building platform was raised again. Then after the slurry was finely squeezeed in the vat, the platform was lowered again into the slurry. When a uniformly imprint of the build platform in the wet slurry film was achieved, the system setup was complete.

Subsequently, the vat was filled with the degassed slurry, the double-edged blade coated the surface evenly in a certain thickness. This so-called "wet layer thickness" was then adjusted with the millimeter screws shown in Fig. 9. and measured with a special comb, seen in Fig. 16. With the wet layer thickness adjusted to 300 µm, the print job could be started.

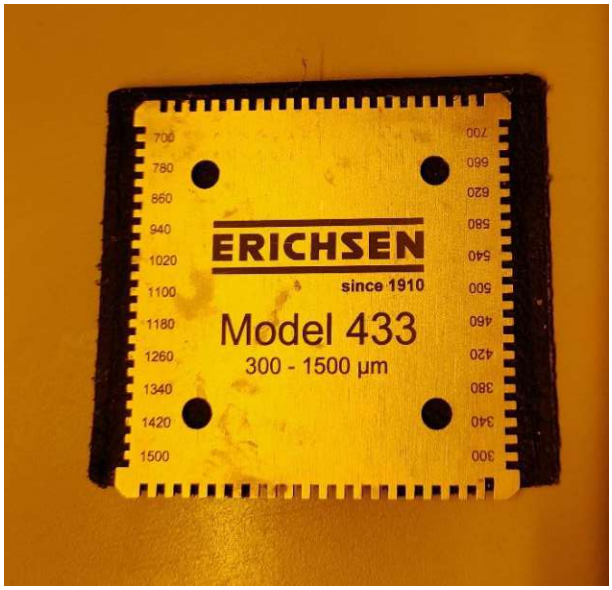

Figure 16: Measuring comb.

4.4.2. Sample Manufacturing with the BP6

4.4.2.1. Choosing printing parameters

Prior to printing, a so-called “job” had to be created. At the beginning stands a STL-file of the wanted geometry. This was drawn in Autodesk Inventor Professional. Afterwards, this file was loaded into the printing job and if wanted could be duplicated to fill up the building plate. Subsequently, all printing parameters were applied. These were kindly provided by the institute, and are shown in the Tables 5 and 6, for a layer thickness of 25 µm and 50 µm.[65]

Table 5: Printing Parameters for a layer thickness of 25 µm

Parameter	unit	value
Layer thickness	µm	25
Illumination intensity base layer	-	500
Illumination intensity part layer	-	500
Number of base layers	#	15
Back light illumination	ms	5000
Exposure time base layer	ms	2500
Exposure time part layer	ms	2500
Tilting speed down base layer	-	5
Tilting speed down part layer	-	10
Tilting speed up base	-	800
Positioning speed base layer	-	5
Positioning speed part layer	-	25
Coating speed a	-	150
Coating speed b	-	10
Z-axis speed at separation	-	1200
Dwell before back light illumination	ms	7000
Dwell before base exposure	ms	10000
Dwell before part exposure	ms	3000
Contact pressing force	N	55
Tilting distance base layer	-	40
Tilting distance part layer	-	40
Separation distance	-	30000
Coating distance	-	535
Minimal object distance	µm	2000
Widening of supports	µm	300

Table 6: Printing Parameters for a layer thickness of 50µm

Parameter	unit	value
Layer thickness	µm	50
Illumination intensity base layer	-	500
Illumination intensity part layer	-	500
Number of base layers	#	10
Back light illumination	ms	5000
Exposure time base layer	ms	9000
Exposure time part layer	ms	4000
Tilting speed down base layer	-	5
Tilting speed down part layer	-	10
Tilting speed up base	-	800
Positioning speed base layer	-	5
Positioning speed part layer	-	25
Coating speed a	-	150
Coating speed b	-	10
Z-axis speed at separation	-	1200
Dwell before back light illumination	ms	7000
Dwell before base exposure	ms	10000
Dwell before part exposure	ms	3000
Contact pressing force	N	55
Tilting distance base layer	-	40
Tilting distance part layer	-	40
Separation distance	-	30000
Coating distance	-	535
Minimal object distance	µm	2000
Widening of supports	µm	300

4.4.2.2. 3D-Printing

The printing process itself was composed of an iterative series of identical steps. The building platform was lowered to a specific height above the surface of the vat, called the layer thickness. This height determined the number of layers that had to be printed, in order to reach the defined geometry of the part.

First, the back light was activated to eliminate irregularities on the surface and to strengthen the adhesion between platform and the part being built. Then the vat could be locally exposed with blue light, corresponding to the slice of the design, The curing process happens at a defined intensity of 25,25 mJ/cm^2 and 4 s of exposure.

Before lifting the building platform, the material vat was carefully tilted away, following a set number of tilting steps over a defined length. This reduced the detaching forces and thereby avoided delamination of layers or even detachment of the entire part from the building platform. The describes process was repeated until the green part was fully built.

4.4.2.3. Postprocessing

When the printing process was finished, the parts were removed from the building platform. This was done carefully with a special type of razor blade. The green body was cleaned from the noncured slurry. This was done in a beaker filled with propylene glycol diacetate. The beaker was put in an ultrasonic vat for 10 min, afterwards the parts were cleaned with a paper towel and support structures were cut off with a scalpel. The coarse cutting edge was then smoothened with superfine sand paper (P1000).[47,85]

To reach the final material properties the ceramic green bodies then underwent debinding and sintering.

4.4.3. Curing depth

In order to know how long the illumination of the single layers should be, curing depth tests were done. The slurry was carefully filled in a template, that was put on a foil, as shown in Fig. 17 This set up, was then placed on the material vat of the 3D-printer. Beforehand, the spots, that were light up, were marked on the material vat. This ensured even curing of the slurry, in every cavity of the template. The excess material was afterwards removed carefully, subsequently the thickness measurement was done, with the Kroeplin IP 67

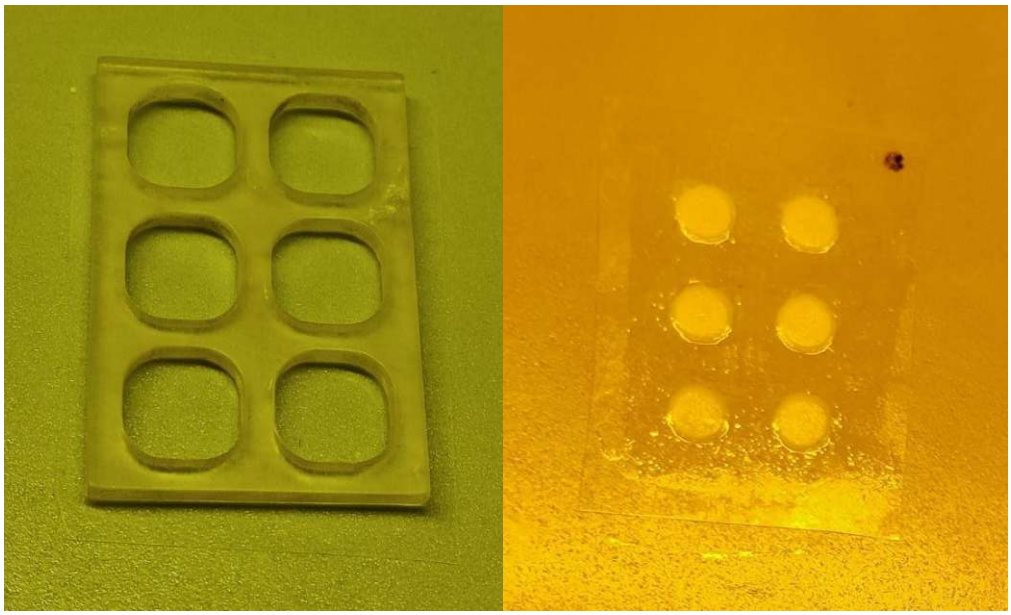

Figure 17: left: cured spots after an exposure of 4 s; right: FEP Foil and Curing Template for the Curing Depth Measurements.

The samples were illuminated for 2, 4, 8, 16 and 30 s of exposure, with 25,25 mJ/cm^2. For every duration six platelets were measured and the average and the standard deviation was calculated.

With the data points generated a working curve was plotted and the penetration depth and critical exposure was calculated.

4.4.4. Shrinkage

When aiming for a precision manufacturing process, it is important to know how much shrinkage accurse in every direction in space, as well as in terms of weight. In order to fulfill this need, at least three cylinders were printed, for every temperature setting during sintering

The printed cylinders were then cleaned as described in the chapter 4.4.2.3 and dried for 24h with silica gel in a desiccator, debinded and sintered according to Table 7 and 8 in chapter 4.5. Afterwards they were weight and measured.

The absolute shrinkage (g or mm) and the relative shrinkage (%), equation 2, could be calculated.

Equation 2: relative linear shrinkage in one direction

$$shrinkage = \frac{\Delta L}{L} * 100$$

4.5. Thermal Treatments

4.5.1. Debinding Profiles

As described in chapter 3.6, the first of the thermal treatment steps, is known as debinding. It removes all organic compounds, leaving a fragile, porous ceramic part behind, referred to as the brown body.

To develop the temperature profile for the printed parts, starting point was found in the profile of Gruber, described in Table 7.[65] To test different heating systems, both the Carbolite furnace with air circulation heating, the Nabertherm oven with resistance coil heating were used.

Iteratively, additional ramps were added to ensure defect free debinding. These profiles were then analyzed via TMA. This way a new improved debinding profile could be established, shown in chapter 5.3.1. of the results.

Table 7: Debinding Profile

Step	Setting	value
1	Starting Temperature (°C)	30
	Ramp (K/min)	1
	Elevation Temperature (°C)	110
	Dwell Time (min)	0
2	Starting Temperature (°C)	110
	Ramp (K/min)	0.3
	Elevation Temperature (°C)	130
	Dwell Time (min)	300
3	Starting Temperature (°C)	130
	Ramp (K/min)	0.3
	Elevation Temperature (°C)	140
	Dwell Time (min)	600
4	Starting Temperature (°C)	140
	Ramp (K/min)	0.2
	Elevation Temperature (°C)	150
	Dwell Time (min)	600
5	Starting Temperature (°C)	150
	Ramp (K/min)	0.2
	Elevation Temperature (°C)	180
	Dwell Time (min)	180
6	Starting Temperature (°C)	180
	Ramp (K/min)	0.2
	Elevation Temperature (°C)	280
	Dwell Time (min)	180
7	Starting Temperature (°C)	280
	Ramp (K/min)	0.2
	Elevation Temperature (°C)	300
	Dwell Time (min)	120
8	Starting Temperature (°C)	300
	Ramp (K/min)	1
	Elevation Temperature (°C)	500
	Dwell Time (min)	30

4.5.2. Sintering Profiles

The sintering profile in Table 8, was available in the database of the Institute of Materials Science and Technology. It is a sintering profile optimized for the use of Al_2O_3 brown bodies, with a maximum temperature of 1600°C.[65]

This profile needed to be adjusted, as the alumina silicate fibers would undergo a solid phase reaction and dissipate into the bulk.

Three different adjustments were made:

1. 1300°C: In this case, the maximum temperature was lowered to 1300°C, all steps leading up to it stayed the same and the dwelling step at a lower temperature afterwards was cut.
2. 1350°C: The procedure was the same as in the 1300°C approach.
3. 1300°C/1250°C: As in the base profile, a dwelling time at lower temperature (1250°C) followed the peak temperature at 1300°C.

Table 8: Sintering profile

Step	**Setting**	**value**
1	Starting Temperature (°C)	30
	Ramp (K/min)	1
	Elevation Temperature (°C)	500
	Dwell Time (min)	480
2	Starting Temperature (°C)	500
	Ramp (K/min)	10
	Elevation Temperature (°C)	1600
	Dwell Time (min)	30
3	Starting Temperature (°C)	1600
	Ramp (K/min)	10
	Elevation Temperature (°C)	1500
	Dwell Time (min)	175

4.5.3. Thermomechanical Analysis

To investigate the debinding process in detail, TMA measurements were conducted.

As seen in Fig. 18, the device consisted of a sample platform, a linear variable differential transducer (sensor) and a furnace (not in the picture, was set around the sample platform, after the sample was fixated).

To start an analysis, a plane-parallel cylindric green part was placed on the sample platform. Carefully, the sensor is lowered on the superior face of the sample, assuring a centered positioning. Then a preload force of 0.1 N was applied and the staring dimension was measured. Over the course of the debinding temperature profile, seen in Table 6, the linear shrinkage and expansion was measured and analyzed with the provided software.

The collected data was analyzed with the Universal Analysis 2000 Software of TA-Instruments.

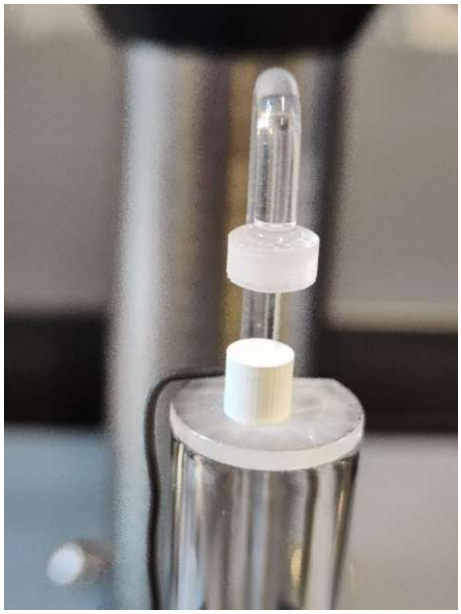

Figure 18: Thermomechanical analysis sample stage without the furnace.

4.5.4. Thermogravimetric Analysis

Additionally, TGA measurements were conducted to study the debinding behavior in detail.

With this analysis the mass loss was considered in dependency to temperature and time. Therefore, the set up differs from the TMA's. The sample stage consisted of a precision scale with a pan, out of an inert material, where the sample was placed, and a furnace around it, as seen in Fig 19.

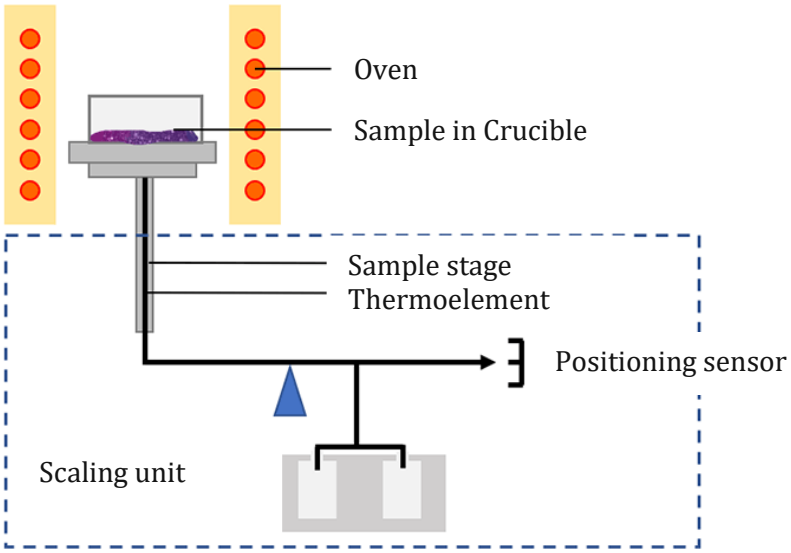

Figure 19: Working principle of a thermogravimetric analysis.

Before the measurement was started, the cooling system had to be activated. After this was done, the Al_2O_3 crucible was cleaned, first simply by using a pipe cleaner, afterwards it is heated with a propane torch to red heat and cooled again.

Then the pan was weight by itself and additionally with the sample inside. Subsequently, the crucible was placed in the autosampler

After all samples were positioned, the software was started and a "routine" was created. When started, data points of the mass change over a certain temperature ramp were collected. These could be used to plot the absolute weight (µg) or the relative weight change (%) against the temperature or the time.

For these experiments a starting temperature of 40°C was chosen. With a heating rate of 0.2 K/min a maximum temperature of 600°C was reached after around 47 h.

4.6. Mechanical Testing

4.6.2. Biaxial Bending Tests

As mentioned in norm DIN EN ISO 6872, three steel balls were placed on a circle of a diameter of 11±1 mm, distributed 120° apart. On top the ceramic discs were placed, before a flat surface piston, with a 0.7±0.1 mm radius, applied a force to the center of the sample, until failure of the material. To distribute the force evenly a flexible thin layer plastic film was placed between the steel balls and the sample and also on top of the disc. The set up can be seen in Fig. 20. In order to fulfill the requirements of the norm, at least 10 and preferably 30 sintered ceramic plates had to be processed of every tested slurry.[89,18]

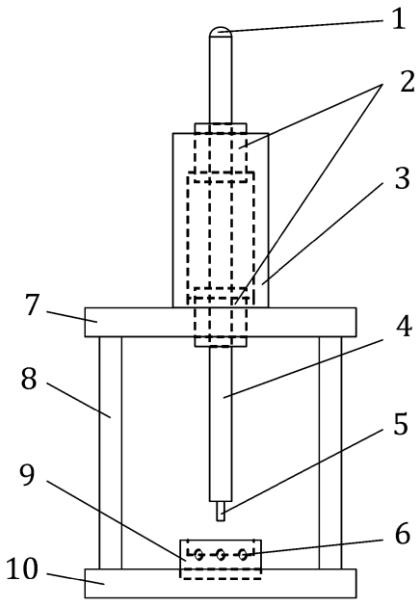

Figure 20: Schematic of the biaxial bending test.[18]

In order to calculate the bending strength value (MPa), the recorded fracture load (N), the thickness and the radius of the disc (mm) were used, seen in equation 3.

Equation 3: Calculation of the bending strength

$$\sigma = \frac{-0.2387 * P * (X - Y)}{b^2}$$

$$X = (1 + v) * \ln\left(\frac{r_2}{r_3}\right)^2 + \frac{(1 - v)}{2} * \left(\frac{r_2}{r_3}\right)^2$$

$$Y = (1 + v) * \left[1 + \ln\left(\frac{r_1}{r_3}\right)^2\right] + (1 - v) * \left(\frac{r_1}{r_3}\right)^2$$

$$\sigma \ldots max.\, stress\ in\ the\ middle\ (MPa)$$

$$P = total\ force\ measured\ at\ break\ (N)$$

$$v = Poisson's\ ratio$$

$$r_1 \ldots radius\ of\ the\ circle\ the\ steel\ balls\ were\ placed\ (mm)$$

$$r_2 \ldots radius\ of\ the\ loaded\ area\ (mm)$$

$$r_3 \ldots radius\ of\ the\ sample\ (mm)$$

$$b \ldots thickness\ of the\ sample\ at\ fracture\ origin\ (mm)$$

Additionally, the Weibull modulus was calculated, this provides a dimensionless parameter that shows the variability of measured material strength values.[18]

Ceramic strength values are generally not normally distributed around its average. Usually, there are slightly shifted towards higher values. To describe both this asymmetric distribution and a normal distribution the two parameter Weibull Statistic is used, seen in equation 4. The cumulative probability of failure (P_f) of an area or volume under stress is connected to two parameters: the Weibull Modulus (m) and the characteristic Weibull Strength (σ_0).[18]

Equation 4: Probability of failure

$$P_f = 1 - e^{\left[-\left(\frac{\sigma}{\sigma_0}\right)^m\right]}$$

4.7. Density Determination by Archimedes' Principle

As described in equation 5, the density of the solid body (ϱ) can be calculated out of the weight of the solid body in air (W(a)), the weight of the solid body underwater (W(fl)), the density of the fluid (water at 20.3 °C, ϱ(fl)), the density of air at standard conditions (ϱ(a)) and a correction constant (Korr).

The constant contains the lift of the measuring basket and geometrical consideration of the set up and thereby only applies to this specific set up.

Equation 5:

$$\varrho = \frac{W(a) * \varrho(fl) - \varrho(a)}{(W(a) - W(fl) * Korr)} + \varrho(a)$$

This method was conducted on the Sartorius LE225D precision scale, with the setup, shown in Fig. 21. The process was strictly done according to the manual provided by Sartorius AG.[90]

Figure 21: Set up for Archimedes' Principle Measurement.

Before any sample was weighed, the temperature of the water was measured. The samples were first weighed in air, then in water, after a fixed time of 30 s. Afterwards, the part was dried with a non-linting paper towel and the process was repeated. The collected weights were then transferred to an excel sheet where the property values were calculated.

5. Results and Discussion

5.1. Optimization of the Slurry

5.1.1. Slurry Composition

As dispersing two fillers, the particles and the fibers is challenging, the dispersing agent Disperbyk©-109, 111, 118, 180, 2152, 2155 and 2157 were investigated.

To ensure the compatibility of the dispersing additive and the master batch, a solubility study was conducted. As seen in Fig. 20, this led to the result, that Disperbyk©-2157 was the only dispersive agent non-soluble in the masterbatch. This led to Disperbyk©-2157 being eliminated from further testing.

Additionally, one could see that Disperbyk©-118 and 2152 were the only additives that showed a slight coloration.

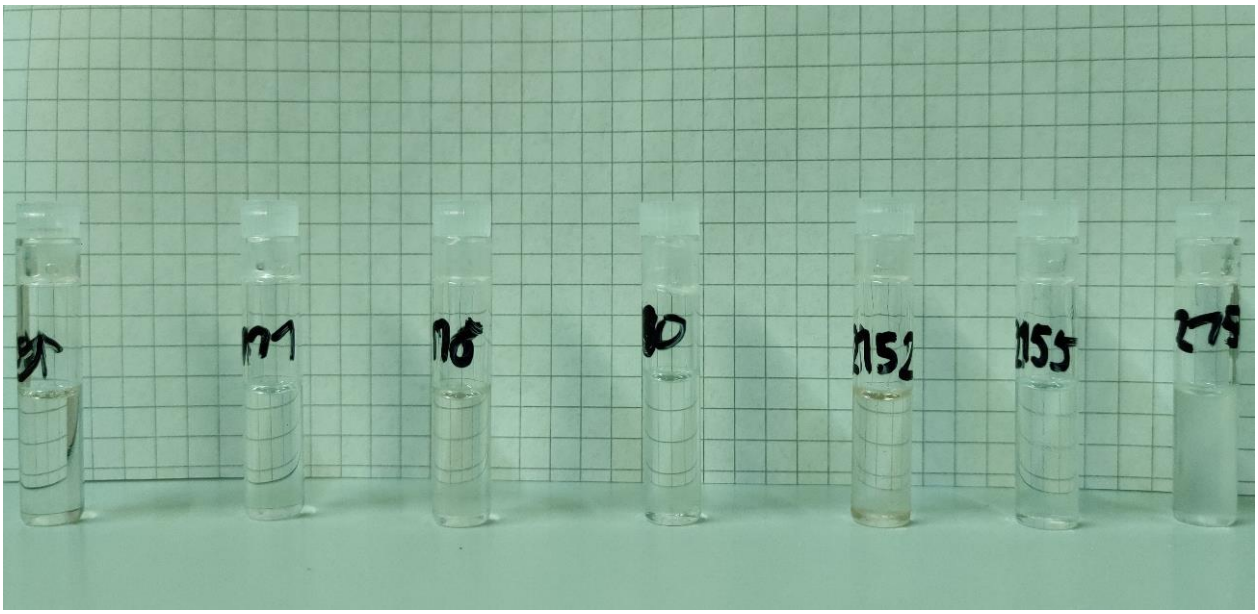

Figure 22: Solubility Test of the Dispersants; from left to right, Disperbyk(c)109, 111, 118, 180, 2152, 2155 and 2157.

After testing all soluble additives, Disperbyk©-2155 was chosen, as it showed the finest dispersion with the filler materials.

Additionally, the Al_2O_3 particles tested in this thesis (TM-DAR) outperformed the previously used Al_2O_3 (A3). Therefore, it replaced A3 as the ceramic filler.

This outperformance could be traced back to the significantly more uniform particle size for TM-DAR, as seen in the SEM images in Fig. 21 and therefor to better dispersibility

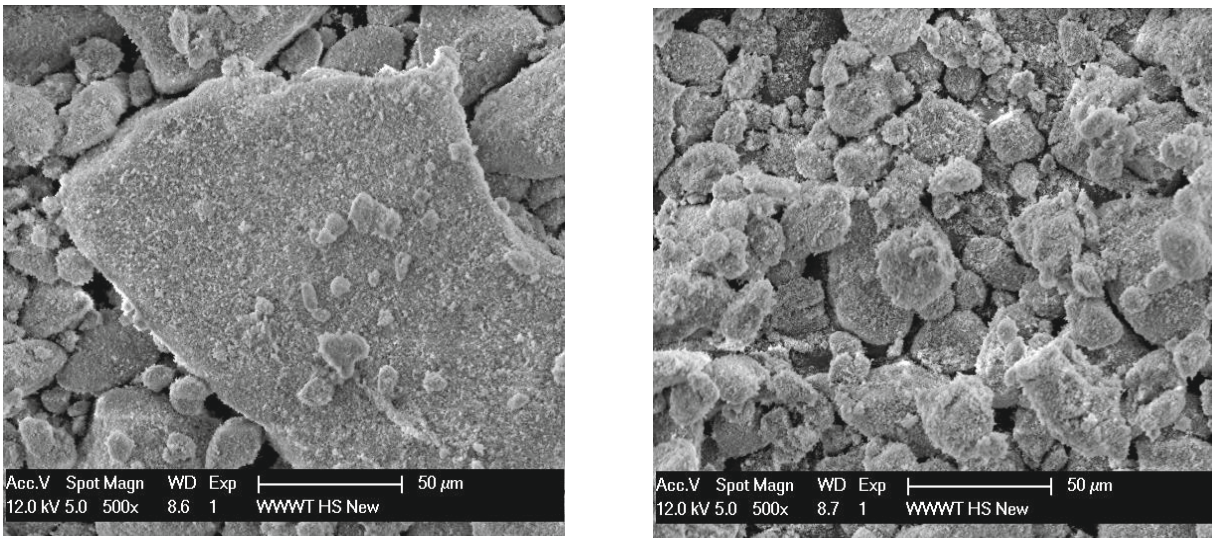

Figure 23: SEM images of the ceramic particles; left A3 and right TM-DAR.

As described in chapter 4.3.1 the ceramic powders were added in a three-step fashion, this allowed the shearing forces to have their biggest effect, during speed mixing. As it is crucial, that the slurry was not so thin in viscosity, whilst at the same time fully incorporating the powders. It is also important, that the remaining master batch is added slowly in order to assure homogeneous mixture, while keeping the shearing forces at its highest.

5.1.2. Dispersing the Filler Material

In this chapter, the results of the different dispersion strategies are being presented and discussed. These included dispersing via ultrasonic horn, ultrasonic bath, speed mixing, milling at the roller mill and predispersing.

Without any further treatment, so just by mixing the components as described in chapter 5.1., the achieved dispersion did not reach the desired agglomeration size of under 30 µm. This "base-line-dispersion" can be seen in Fig 24.

As one can see, there were particles in the size range of 50-100 µm. Leaving them in the slurry would have several unwanted effects. Firstly, the particles would at least match the size of our layer thickness during 3D-printing. This would cause an uneven cure of the layer and furthermore, could led to delamination of this or the next layer, as adhesion between the polymer layer would not be guaranteed. Even if a part could be printed with this slurry, the problems would continue to haunt one. The agglomerates also have an influence in the debinding and sintering process and finally would be considered as defects in the final material. This could lead to lower mechanical strength.

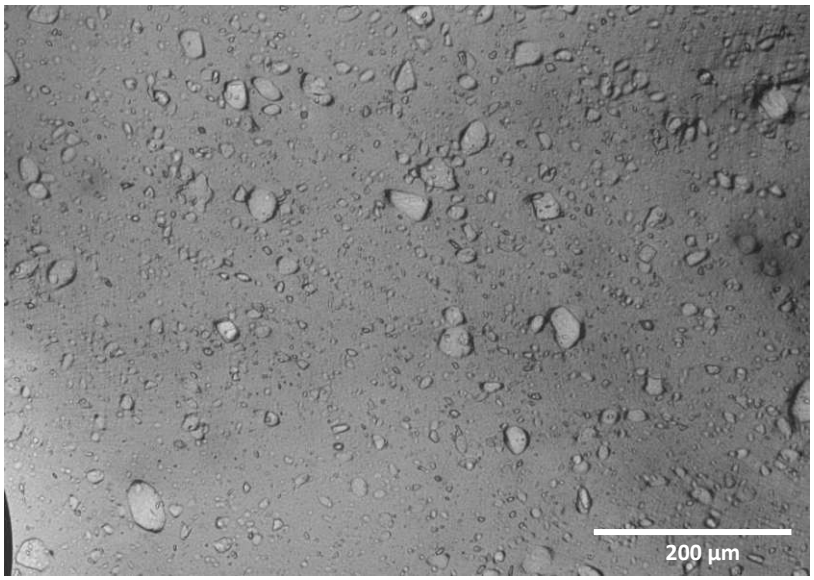

Figure 24: Ceramic Slurry without any treatment.

5.1.2.1. Ultrasonic Horn

As one can see in Fig. 25, the first dispersing experiment, only done with Al_2O_3, led to some change in the size and distribution of the agglomerates, but not to a dispersed slurry with agglomerates below 30 µm. There were still a great number of particles of around 50 µm and the slurry hereby would not result in a material of wanted properties.

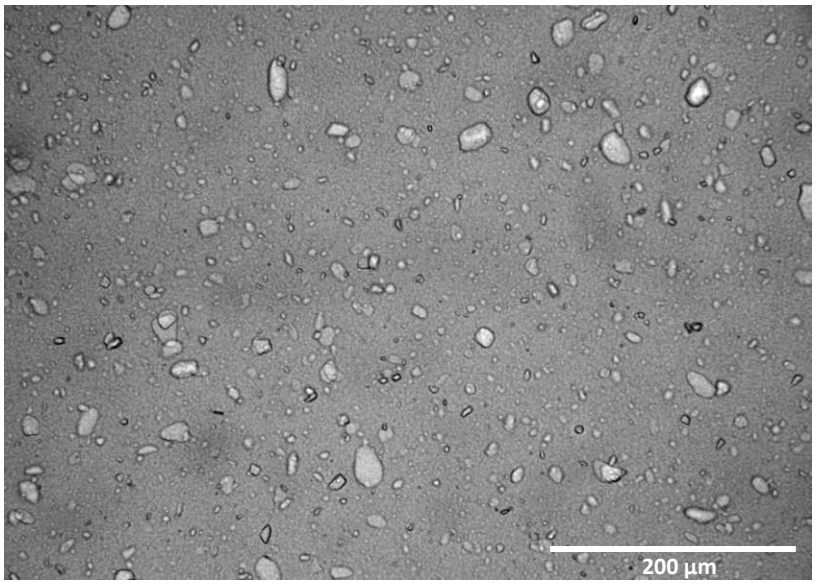

Figure 25: Ceramic Slurry after 40 min of Ultrasonic Treatment at Output Setting 2-4.

This was improved by increasing the output setting to 6. Additionally, a magnetic stirring unit was added, due to the high viscosity of the slurry. The stirrer was set on 900 rpm and was kept this way. The process was conducted, until 40 min of sonification were reached, with an amplitude of 30 at the start, that drop to 20 in the first half of sonification and stayed there for the second half.

After the mentioned adjustments, the most promising outcome was achieved, seen in Fig. 26, were most of the particles were in a printable size range.

Despite promising results, this method was not further investigated. This was due to the high viscosity of the slurry, which led to insufficient removal of the generated heat, thereby hindering further deagglomeration.

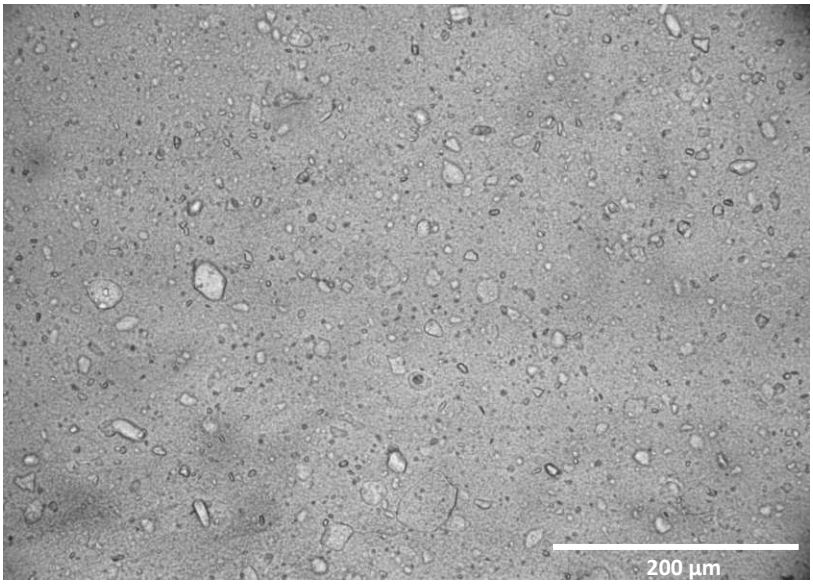

Figure 26: Ceramic Slurry after Ultrasonic Treatment of 40 min at Output Setting 6.

5.1.2.2. Predispering

As seen in Fig. 27, the Al_2O_3 powder was simply predispered in a speed mixing cup on a magnetic stirrer. Predispersing decreased the average size and the size distribution. It can be seen, that the size distribution shifted towards smaller sizes of 30 µm and below, only leaving a few bigger agglomerates. Therefore, predispersing was the superior method. The remaining agglomerates above 30 µm were tackled, when predispersing on the roller mill.

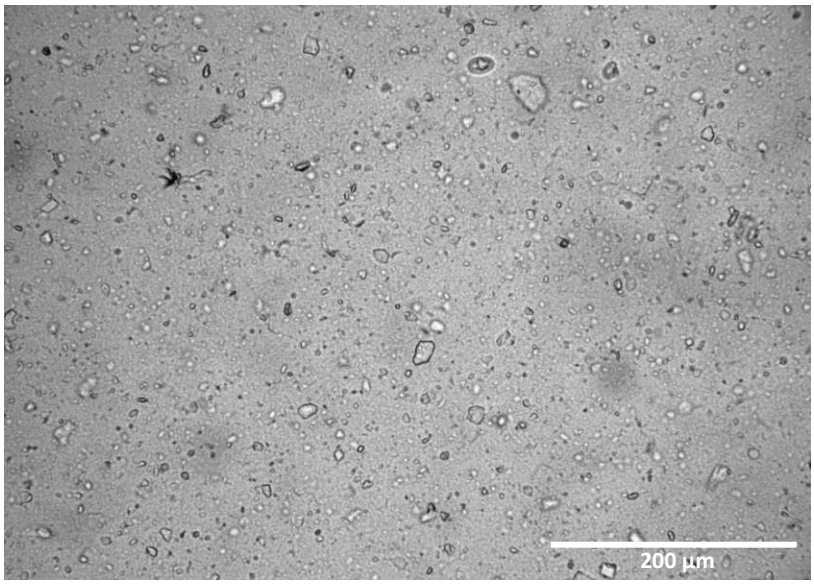

Figure 27: Ceramic Slurry composed of predispered Al_2O_3 particles.

When looking at Fig. 28, agglomerations of sizes around 20 µm were a sparse exception, so few, that using the grind gage, they could no longer be detected. In fact, these tests only showed a particle size of around 10 µm.

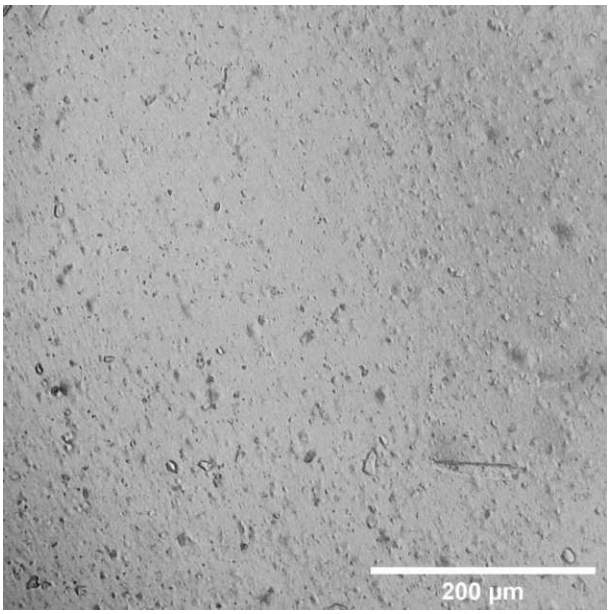

Figure 28: Ceramic Slurry composed of predispered Al_2O_3 particles, 24 h on the roller mill.

As the method resulted in the smallest particle size, both ceramic fillers were dispersed via this route. The following figures display the best results of the dispersant optimization and should be considered as benchmarks for future optimization. All the slurry depicted consist of predispersed ceramic fillers, with 1 wt.-% fibers, that were predispersed on the roller mill with 5 wt.-% respective dispersant added.

When looking at Fig. 29, even as little as 1 wt.-% added fiber powder already changed the dispersion in the polymer matrix drastically. Therefore, only these pictures will be shown, as the other slurries would not yield an improved material or even printable slurry.

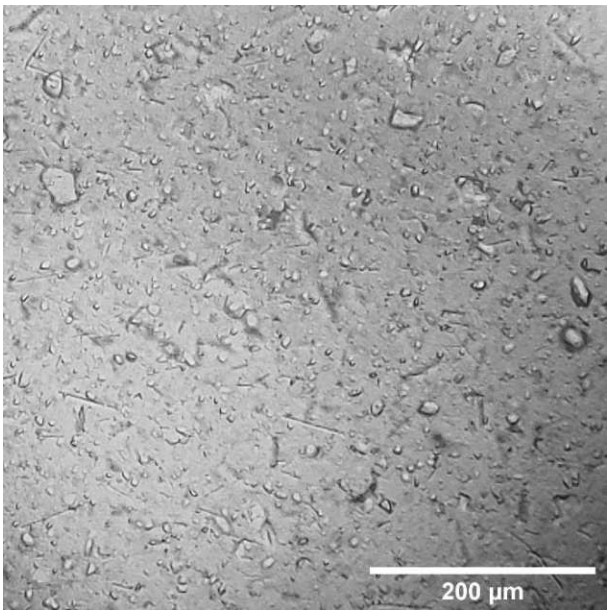

Figure 29: Ceramic slurry with 1 wt.-% fibers and 5 wt-% Disperbyk©-111.

When comparing Disperbyk©-118 and 111, Fig. 30, one can discard Disperbyk© -118 for further testing, the size distribution was just spread out to widely, even leading to agglomerations bigger than 100 µm.

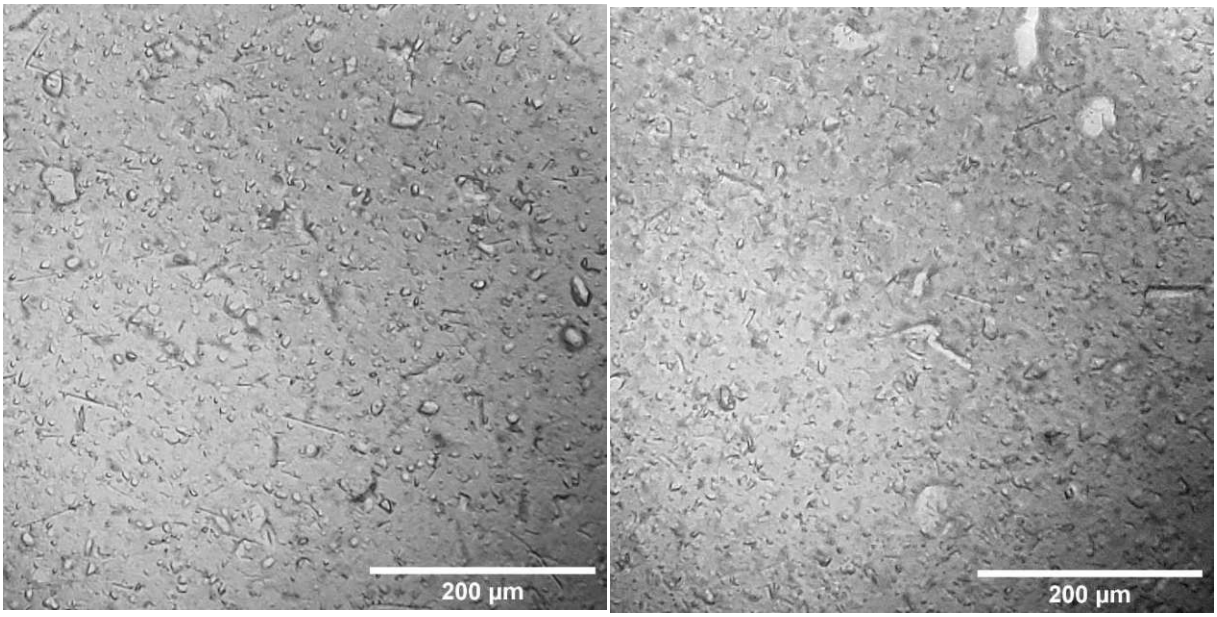

Figure 30: Comparison of a ceramic slurry with 1 wt.-% fibers and 5 wt-% Disperbyk©-118 on the right, with a Ceramic slurry with 1 wt.-% fibers and 5 wt-% Disperbyk©-111 on the left.

When comparing Disperbyk©-111 and 2155, Fig. 31, it can be seen, that Disperbyk©-2155 has a narrower size distribution and also that many of the bigger structures could be assigned to fiber, where with Disperbyk©-111 more Al_2O_3 agglomerates formed.

Additionally, there were tests with only 1 wt.-% dispersant added to the predispersing step. These also favored Disperbyk©-2155.

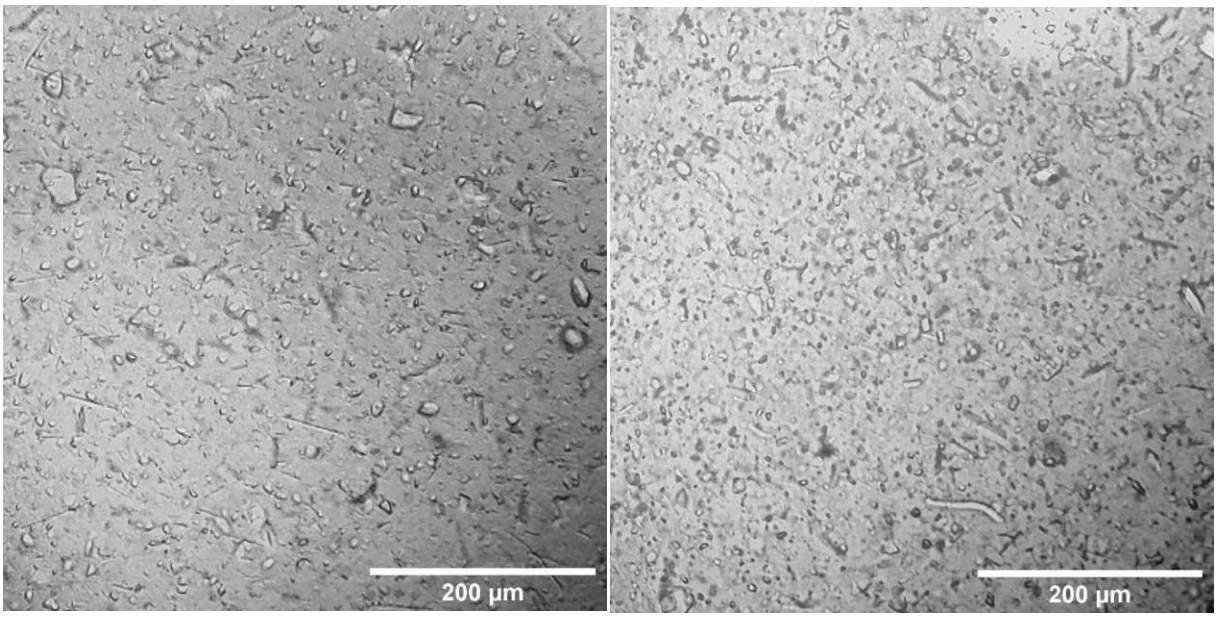

Figure 31: Comparison of a ceramic slurry with 1 wt.-% fibers and 5 wt-% Disperbyk©-111 on the left with a ceramic slurry with 1 wt.-% fibers and 5 wt-% Disperbyk©-2155 on the right.

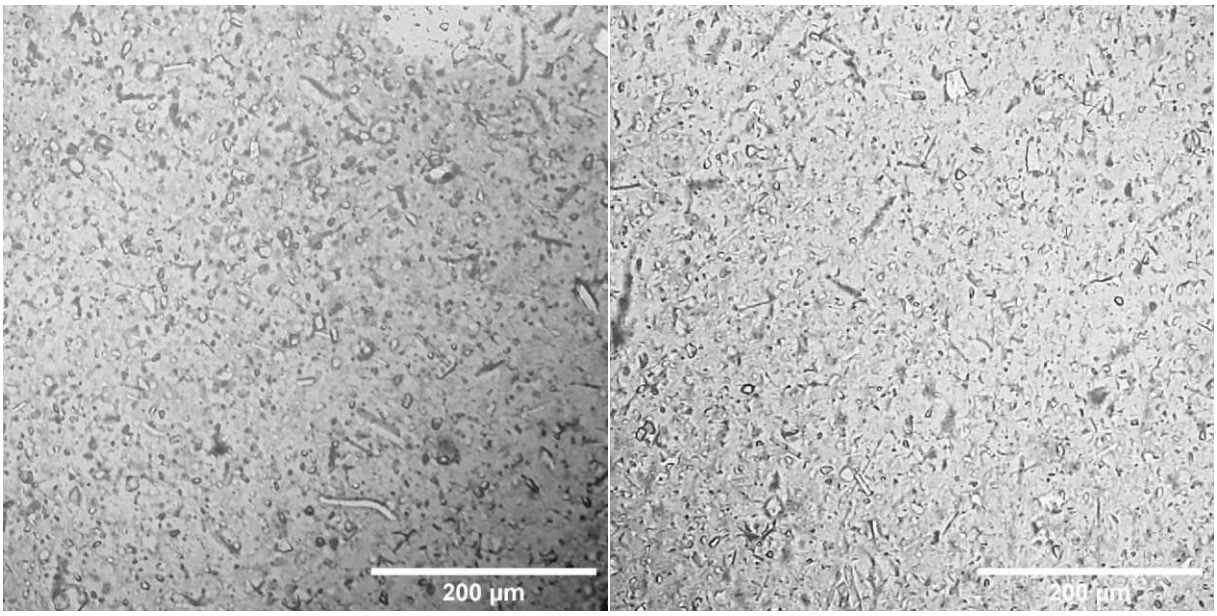

Figure 32: Comparison of a ceramic slurry with 1 wt.-% fibers and 5 wt-% Disperbyk©-2155, collectively dispersed on the right, with a Ceramic slurry with 1 wt.-% fibers and 5 wt-% Disperbyk©-2155, separately dispersed on the left.

The smallest particle size, as seen in Fig. 32, were achieved with 5 wt.-% Disperbyk©-2155 and 1 wt.-% fibers, when the fibers and the ceramic powder were predispersed together on the roller mill for 24 h.

Compared to figures 29-31, one could easily tell, that the dispersion was more evenly, providing smaller agglomerates with a narrower size distribution, leading towards better printability and better material properties.

5.1.3. Rheology Measurements

After the first slurries that had sufficient dispersion of the fibers and particles, rheology measurements were conducted. The goal of these investigations was the identification of 3D-printable formulations. Of special interest, was the difference in viscosity of the slurry with 1 wt.-% and 5 wt.-% Disperbyk-2155 added, as both showed promising results in terms of dispersion and for debinding and shrinkage the amount of added organic compounds should be kept to a minimum.

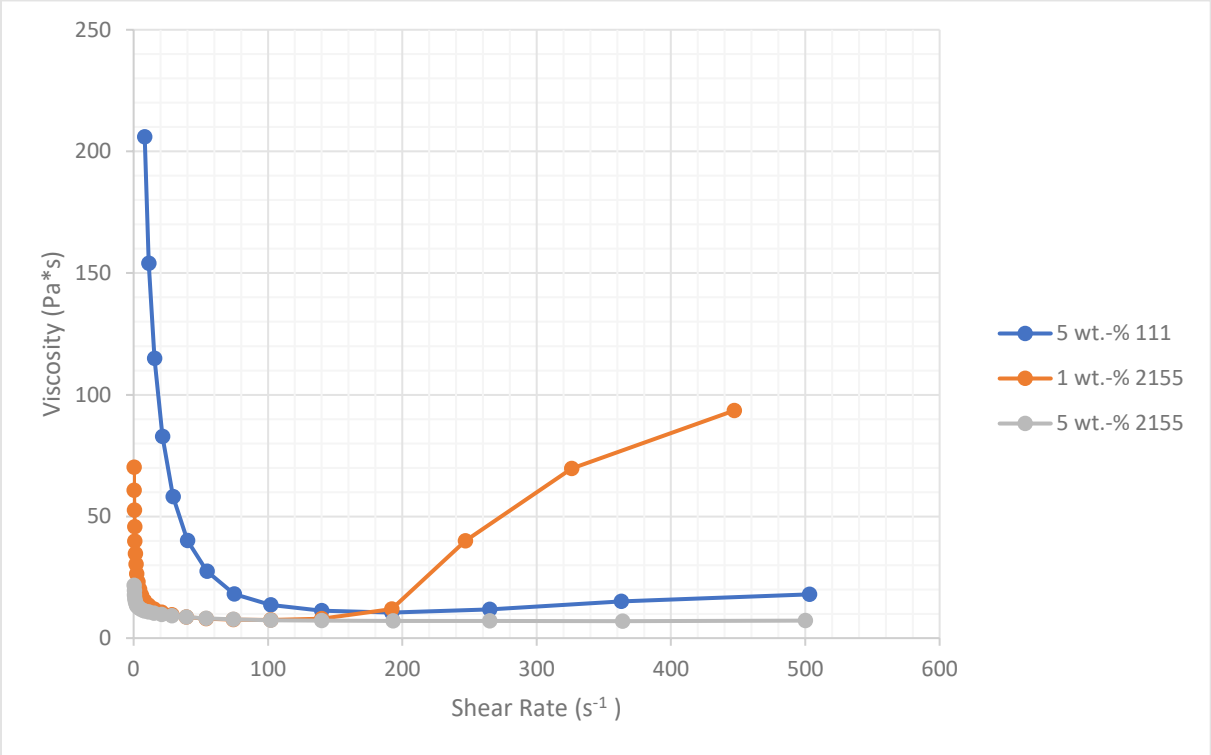

Figure 33: Rheology Measurements of slurries with different dispersant concentration and dispersant type.

As can be seen in the graph above, there was a significant difference in the plot of the 1 wt.-% Disperbyk-2155 slurry compared to the other curves. This excluded the slurry for 3D printing.

What can also be seen, is that with the switch from Disperybyk-111 to 2155 the viscosity also dropped drastically. Going from a viscosity of 80 Pa*s to one of 10 Pa*s, at 20 s^{-1}, depicting a serious improvement.

As it is of interest to lower the concentration of dispersant added as far as possible, while remaining with a printable slurry. It was investigated, if one can raise the amount of PPG instead

of the dispersant. Therefore, three adjusted versions of the 1, 3 and 5 wt.-% 2155 slurry were mixed, adding 2, 5 and 10 wt.-% PPG.

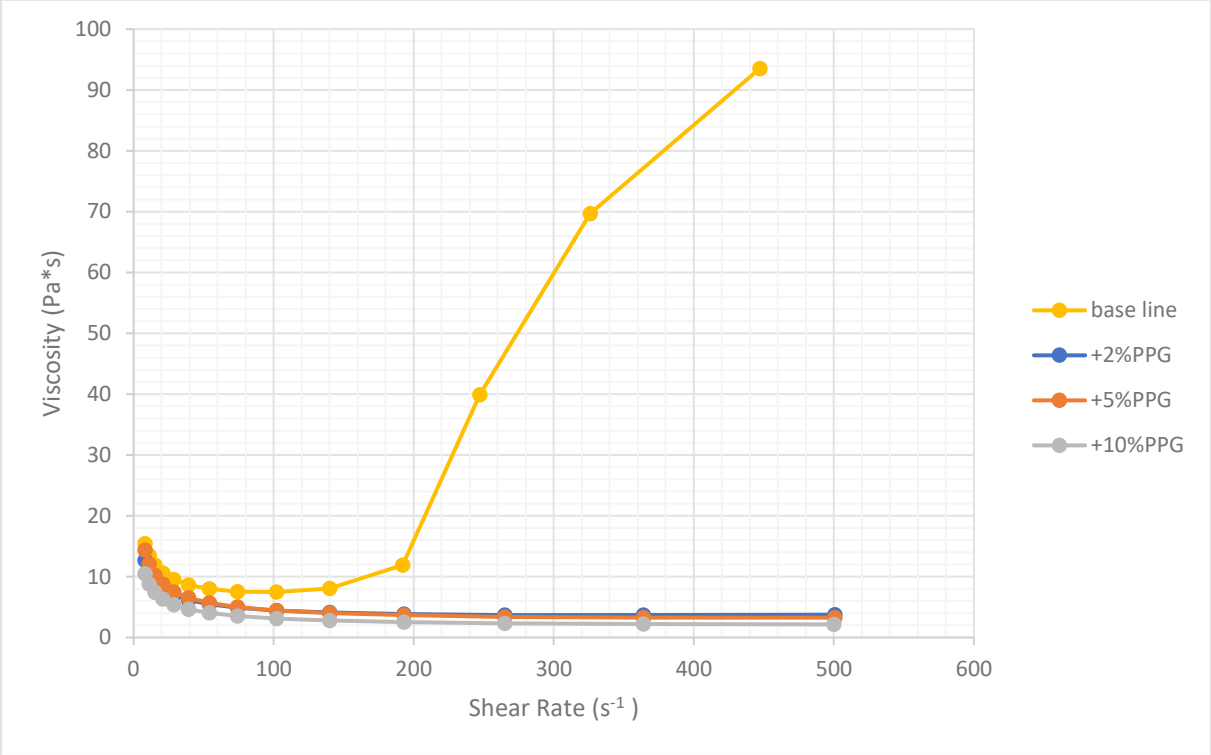

Figure 34: Comparison of the adjusted 1 wt.-% Disperbyk-2155 slurries.

As seen in Fig. 34, this indeed led to a decrease in viscosity and thereby to the loss of the skyrocketing viscosity increase. The viscosity generally dropped with additional wt.-% of PPG added. The most significant impact was generated when going from no PPG added to 2 wt.-% PPG added. This already made the abnormality disappear and changed the viscosity at 20 s^{-1} from 10.6 to 8.04 Pa*s. With 5 wt.-% PPG added, this changed to 8.74 Pa*s and with 10 wt.-% to 6.32 Pa*s.

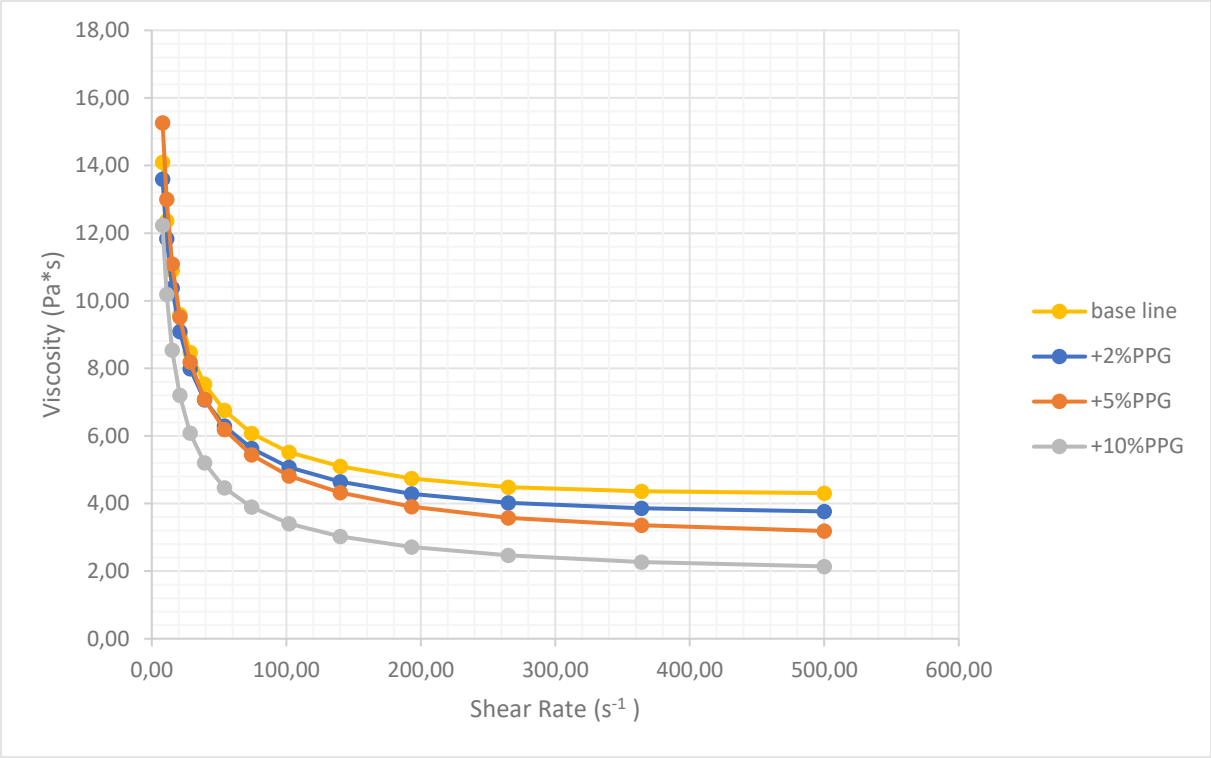

Figure 35: Comparison of the adjusted 3 wt.-% Disperbyk-2155 slurries.

The comparison of the 3 wt.-% Disperbyk-2155 slurry, seen in Fig 35, shows the gradient change of viscosity based on the wt.-% of added PPG. However, at a shear rate of 20 s^{-1}, there is a raise from a viscosity of 9.09 to 9.59, when comparing 2 wt.-% with the 5 wt.-% PPG added. Finally, with 10 wt.-% PPG added the viscosity dropped to 7.20 Pa*s.

When looking at Fig. 36, one can see, that this tendency is disrupted for the 5 wt.-% Disperbyk©2155 slurry. There is a severe drop in viscosity at 20 s^{-1}, going from 9.61 Pa*s to 6.20 Pa*s. When adding more PPG slightly increased to 7.17 Pa*s, but when following the graph on can see, that the viscosity dropped at higher shear rates. Finally with 10 wt.-% PPG added the viscosity at 20 s^{-1} dropped again to 6.01 Pa*s.

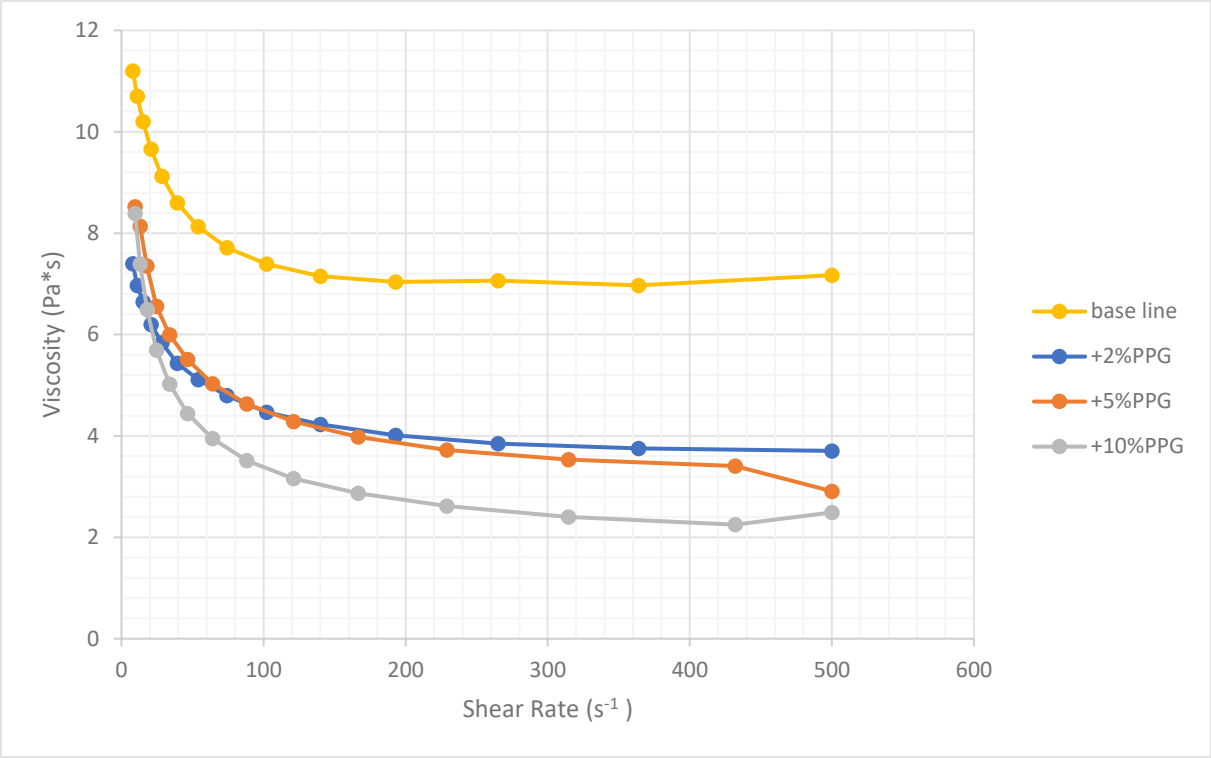

Figure 36: Comparison of the adjusted 5 wt.-% Disperbyk©-2155 slurries.

It can be concluded, that all of these adjusted slurries would make future candidates for further testing. Especially interesting are the slurries with 2 wt.-% added, as this is only a minor adjustment, that lowered the viscosity at 20 s^{-1}.

5.2. Optimization of the Print

5.2.1. Sample Manufacturing with the BP6

Firstly, the print was tried with 25 µm layer thickness, but this led to a few problems. The main problem was, that the parts detached from the building platform, during the printing process. This not only happened from the building platform, which could be adapted via an increase of the back layer exposure time, but also between the printed layers. The lack of interlaminar adhesion could be a symptom of the ceramic agglomerates or an indicator of a loose building platform. It was decided to go with the 50 µm program instead. This worked out without any major setbacks.

5.2.2. Curing Depth

In order to compare slurries that have no fibers with ones that have fibers, four working curves were plotted. This was done for the base recipe slurry, the new recipe slurry and the slurries with 1 wt.-% B102 fibers with 1 and 5 wt.-% Disperbyk©-2155. To understand this method in more detail, figure 37 shows a sheet of cured plates after 16 s of exposure, ready to be measured.

Figure 37: left: measurement tool; right: FEP-Foil with 6 cured slurry platelets after 16 s of exposure.

Table 9 shows the individual measurements, their average value and standard deviation.

Table 9: Curing depth measurements

Slurry	Time (s)	Curing depth (µm)	Standard Deviation (±)
Base formulation	1	95.0	4.47
	2	132.7	2.64
	4	232.5	9.35
	8	324.2	12.01
	16	397.5	4.18
	30	487.5	19.17
New formulation (see Slurry Composition)	1	101.7	6.83
	2	154.2	9.70
	4	223.3	13.29
	8	319.2	11.14
	16	371.7	12.52
	30	438.0	21.37
1 wt.-% B102 1wt.-% 2155	1	94.2	4.91
	2	143.3	13.66
	4	198.3	5.16
	8	268.3	4.08
	16	350.0	32.86
	30	397.0	24.85
1 wt.-% B102 1 wt.-% 2155	1	102.5	7.58
	2	165.0	19.75
	4	211.7	7.07
	8	262.5	10.36
	16	326.7	6.06
	30	373.0	6.89

As seen in the graph below, the curing values varied, which ultimately led to different critical exposures and penetration depths.

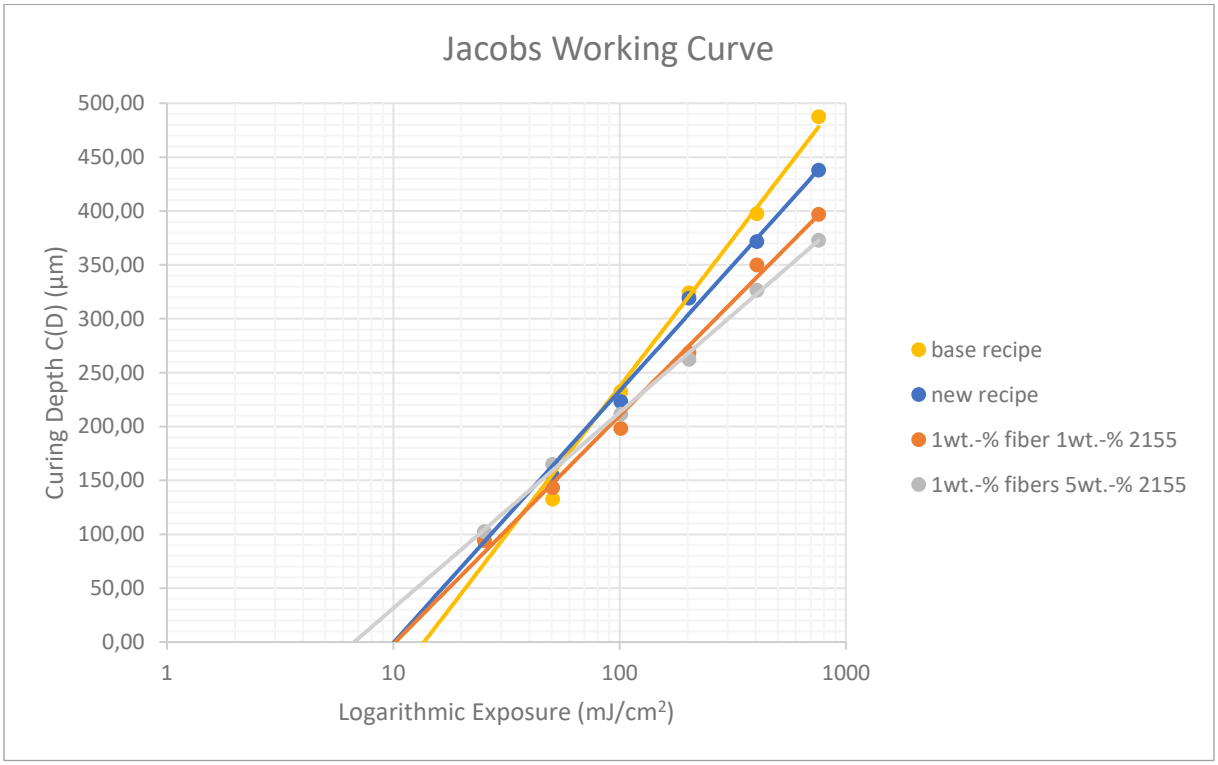

Figure 38: Jacobs working curve of the four investigated slurries.

As expected, the slurry with the highest amount of fibers and Disperbyk-2155 had the lowest critical light exposure (E_c) with 6.72 mJ/cm^2 and a penetration depth (D_p) of 0.33 mm.

The new recipe slurry and the one with 1 wt.-% fibers and 1 wt.-% 2155 were quite similar. This shows, that the addition of only 1 wt.-% fibers, does not affect the light scattering in a drastic fashion. The new recipe has a slightly lower E_c of 10.08 mJ/cm^2, but has a higher D_p of 0.42 mm, compared to the 10.22 mJ/cm^2 and 0.39 mm of the 1 wt.-% fiber and 1 wt.-% 2155 slurry. This underpins that there is slight light scattering due to the fibers.

The highest values of critical exposure and penetration depth were achieved by the base recipe at 13.68 mJ/cm^2 and 0.50 mm.

These results show, that either the different dispersants of the base and new recipe have different optical properties or that the amount adhered to the ceramic particles varies. It could be seen, that the amount of fibers also played a role, but with only 1 wt.-% added, the difference to the blank sample was minor.

5.3. Thermal Treatment

5.3.1. Debinding

As mentioned in chapter 4.5.1 the debinding process was optimized during this master thesis.

The first trial with sinter sand looked promising, but it generated broken platelets in the end. One explanation could be, that the sand grains are pushing back on the plates, as they expand, causing additional stress. On top of that, the slight temperature gradient between the sand and the air in the oven, could provide stress on the sample.

As the Carbolite furnace was heated via air circulation, the sinter sand experiment was retried in the Nabertherm oven, which is heated via resistance coil. This provided no improvement.

The profile provided by Gruber worked for the reinforced ceramic parts and the plain Al_2O_3 parts, with the improved organic matrix, but only for printed cylinders. When the biaxial bending plates were treated, only the fiber reinforced ceramic parts did not break during the process. One theory is, that the fibers could help with the transportation process of the gases during debinding, creating channels where gases can travel more easily to the outside. The optimized base slurry (new recipe) could not be debinded with the profile the base recipe slurry could.

To ensure the defect-free debinding of the sample, an additional ramp at 165 °C was added, with a heating rate of 0.2 K/min and a dwell time of 10 h was chosen. This did not show an effect, both the upright and the flatwise plates broke. Subsequently, two ramps were added one at 160 °C and one at 170 °C. Both ramps were heated to with 0.2 K/min and had a dwelling time of 10h.

After revaluation of the TMA measurement, an additional step at 230 °C was added, again with ramp of 0.2 K/min and with a dwell time of 180 min. This final adjustment, allowed for suitable debinding.

After revaluation of the TMA measurement, an additional step at 230 °C was added, again with ramp of 0.2 K/min and with a dwell time of 180 min. This final adjustment, allowed for suitable debinding.

In the end, three additional steps were inserted at 160, 170 and 230 °C. This allowed for sufficient debinding of the platelets with and without fibers.

5.3.2. Sintering

In order to create the strongest parts possible, different sintering profiles derived from Grubers profile were tested.[65] One of these profiles had its peak temperature at 1600 °C, as here phase transition of the fibers was expected.

The different sinter profiles influenced the density and porosity, discussed in chapter 5.5, as well as on the existence of fibers in finished CMC part.

When sintering at 1600°C the fibers undergo solid state reaction and mixed with the matrix material. As seen in Fig. 39, no fibers could be found and there were large crystalline structures, while still having the highest density with 3.937 g/cm^3 and lowest porosity, reaching 99% of the theoretical density.

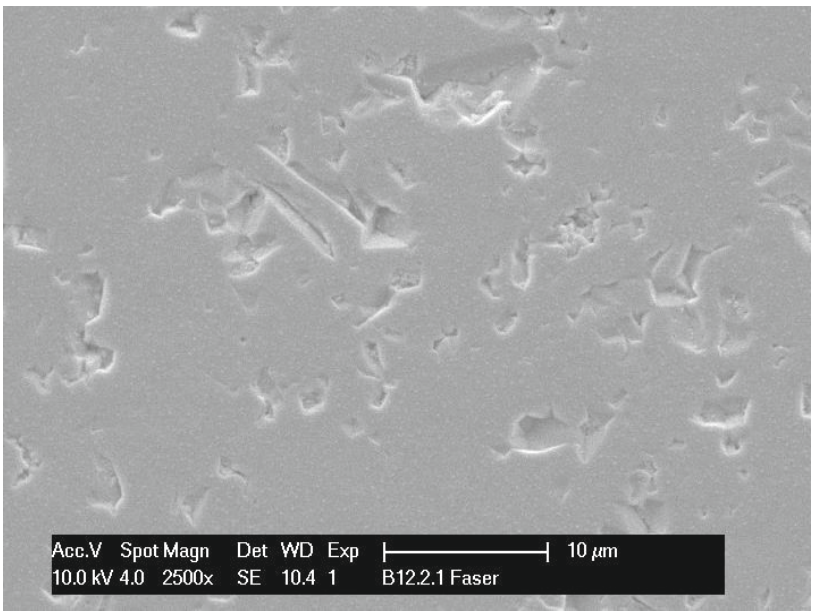

Figure 39: SEM Image of the 1 wt.-% B102, 5 wt.-% Disperbyk(c)2155 slurry, sintered at 1600°C.

With any other temperature profile, fibers could be found in the cut image. Fig. 40, show this for the 1300°C, 1300°C/1250°C and 1350°C temperature profile.

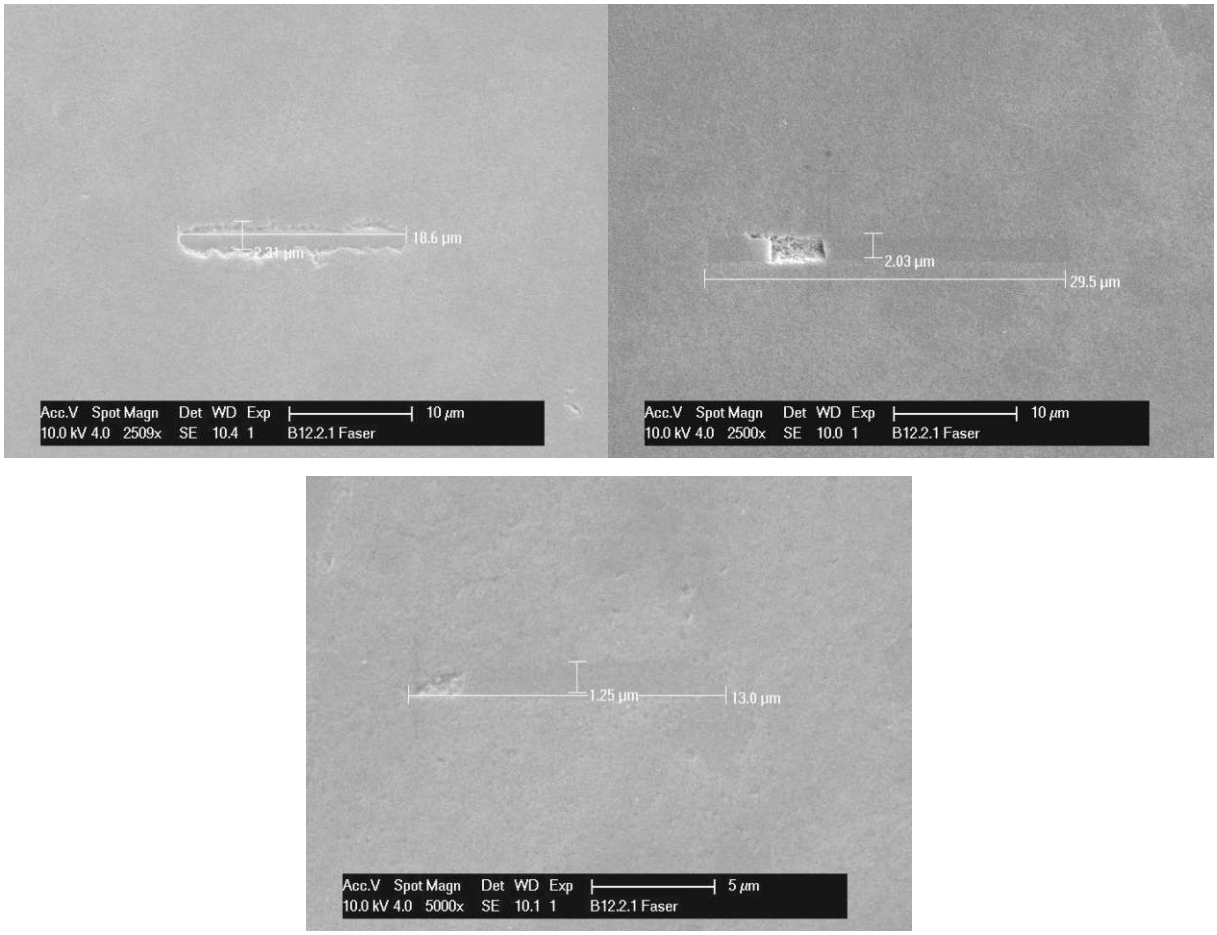

Figure 40: SEM Images of the different sintering temperatures; top left 1300°C, top right 1300°C/1250°C and bottom 1350°C.

5.3.3. Thermomechanical Analysis

When looking at the TMA graph of the base recipe, seen in Fig. 41 and following the green line of the dimension change, one could see, that with increasing temperature, the sample shrunk. In only the first 500 min, the half of the dimensional change had already happened, but hence there were no disturbances in the further course of the plot and there were no defects in the part as well, this was not investigated in more detail.

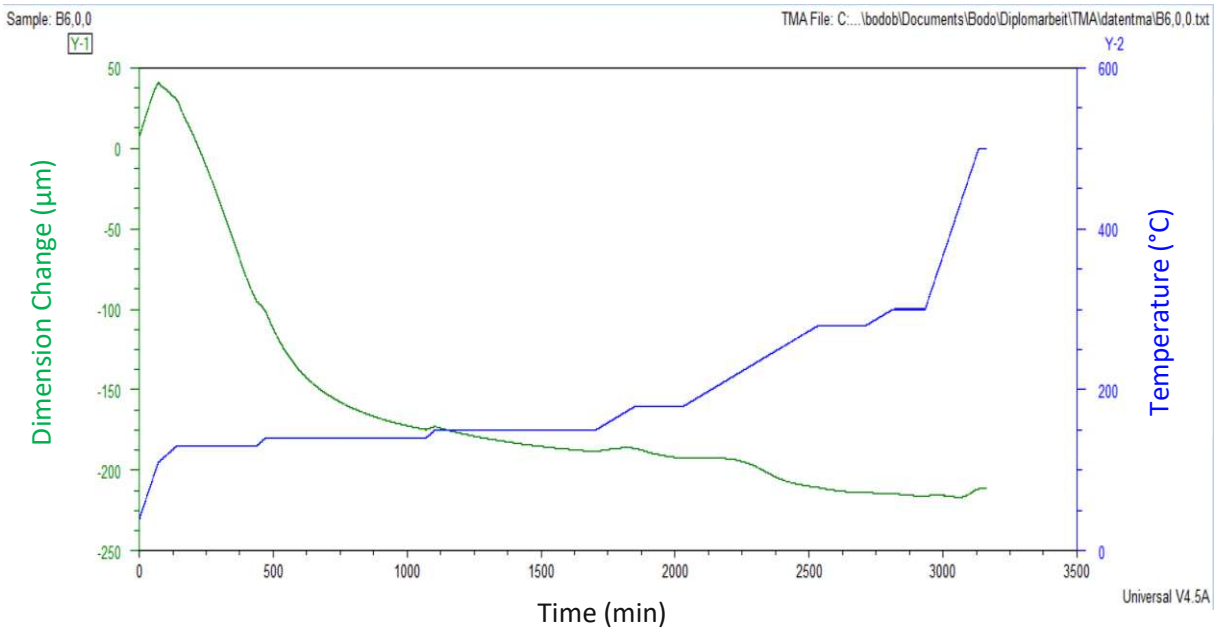

Figure 41: TMA graph of the base recipe slurry.

During this debinding step, at 110 °C, solvent residues evaporated and also the TMPPTOA starts to break down and evaporate. As can be seen, at every temperature ramp, there was slight increase in the dimension change, this could be due to simple expansion of the crystal lattice, afterwards the sample shrunk again.

During the next dwelling time at 150 °C, all the organic compounds, except for the UDMA, have started to evaporate and were transported outside of the material. This correlated to the boiling temperatures of the used components.

As this was a crucial part of the process, the dwelling time is 10 h long and therefore double the length of the dwelling time at 130°C. To make sure, that everything is removed without breakage of the sample, additional ramps and dwelling times until 180°C were present in this debinding profile. This insured, that the other components, except for the UDMA, were

removed. This could create big enough pores, by the absence of said organic materials, for the rest to diffuse easily.

During the ramp to 280°C and the following dwelling time, all UDMA should at least be evaporated. The temperatures above 280°C should remove every bit of the organic matrix.

When looking at Fig. 42, two things stick out: firstly, the same dimension change that happened for the base recipe during the 500 min, takes this sample around 1500 min and the stress on the sample was lower that way. Secondly, two distortions were visible. Once when heating to 180 °C and a second time during the heating period from 180°C to 280°C.

Both of which could cause stress in the sample, but as there were no stronger disturbances, characterized by a discontinuity region, the sample did not break.

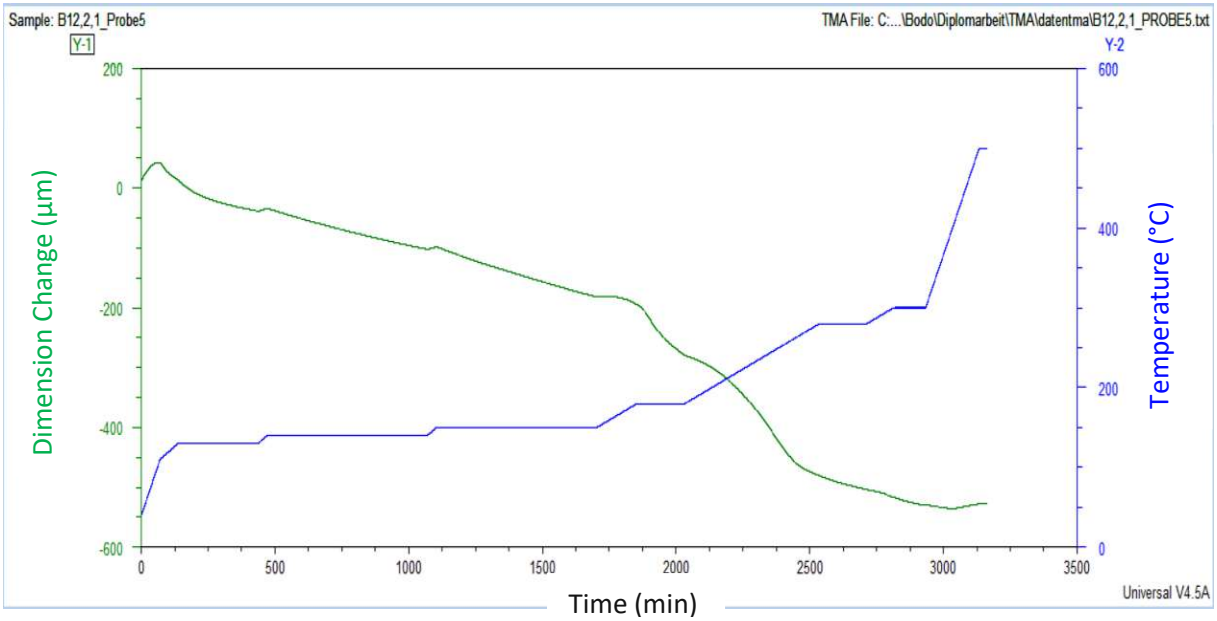

Figure 42: TMA graph of the 1 wt.-% B102, 5 wt.-% Disperbyk©-2155 slurry.

When comparing Fig. 42 and 43, and therefore the slurries with 5 wt.-% Disperbyk©-2155 with fibers and without them, two more or less equal TMA plots could be looked at. The only difference, were the shape of the region between 150 and 280°C. For the sample without fibers,

the first distortion was little smaller, but with no discontinuity region, also this sample stayed intact.

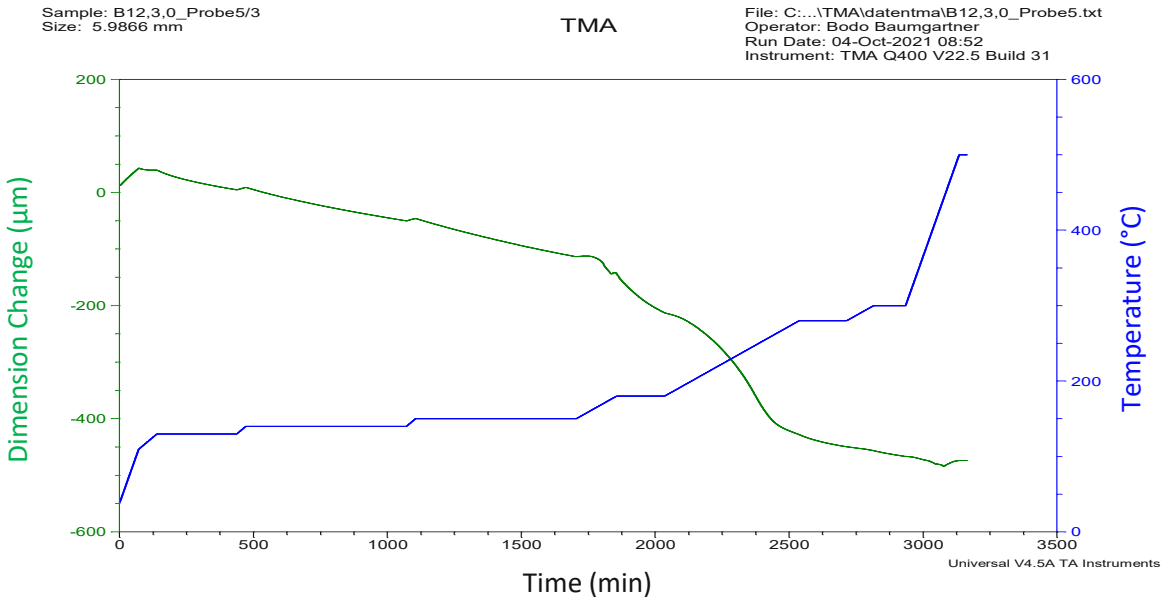

Figure 43: TMA graph of the 5 wt.-% Disperbyk©-2155 slurry without fibers (new recipe).

5.3.4. Thermogravimetric Analysis

With the TGA measurements the mass loss (%) was investigated during a certain heating rate. Out of this correlation, one could extract the temperatures, at which substances start to react and the behavior of the decomposition. With every new “step” in the diagram, a new matrix material starts to decompose and depending on the slope of the graph, this process is more abrupt or not.

When discussing the mass loss displayed in Figure 44, and thereby the newly optimized slurry composition with fibers, one could tell, that the process was divided in 3 stages. First, starting at around 100-110°C, the SR492 starts to decompose, this is shortly followed by the PPG425 and ends with the dispersion additive at around 200°C. The next step described the decomposition of UMDA.

It is depicted, how the mass loss did not end with the decomposition. The gaseous phase had to be transported out of the ceramic brown body. This is the process depicted between 280-500°C.

All in all, a mass loss of 24,34 wt.-% was achieved, which is a slight offset to the 21,54 wt.-% organic components added. As described by Pfaffinger et al. in 2015 [91], this could be due to the hygroscopic properties of the slurry components. The water was retained by the humidity of the air during building and storage.

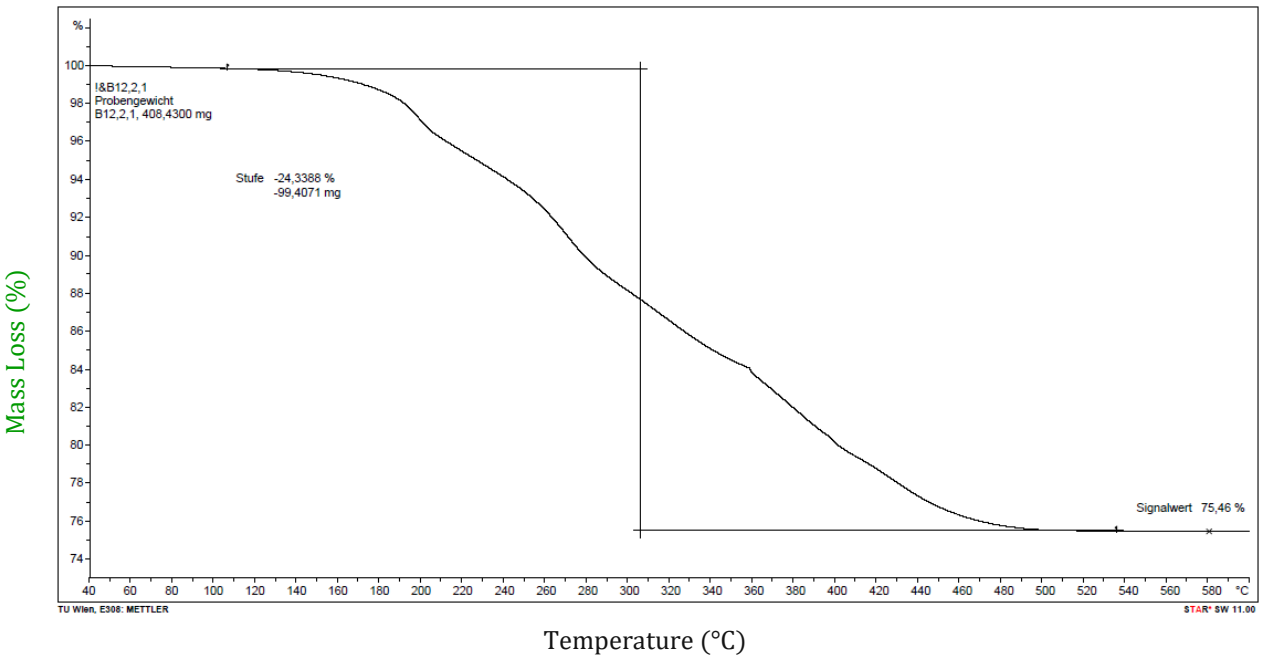

Figure 44: TGA plot of a fiber-containing green body of the optimized composition.

When looking at the plot of the fiber-free green body, in figure 43, a similar trend could be seen. Again, the organic compounds, step by step, started to decompose and evaporate, but there were some relevant differences compared to the sample with fibers as well.

The first step is slightly elongated stopping at 210°C not 200°C. Also, the diffusion phase after 280°C show a step-behavior. This comes from the worse diffusion paths without fibers. Subsequently, reaching a mass loss plateau slightly later at 505°C instead of 495°C.

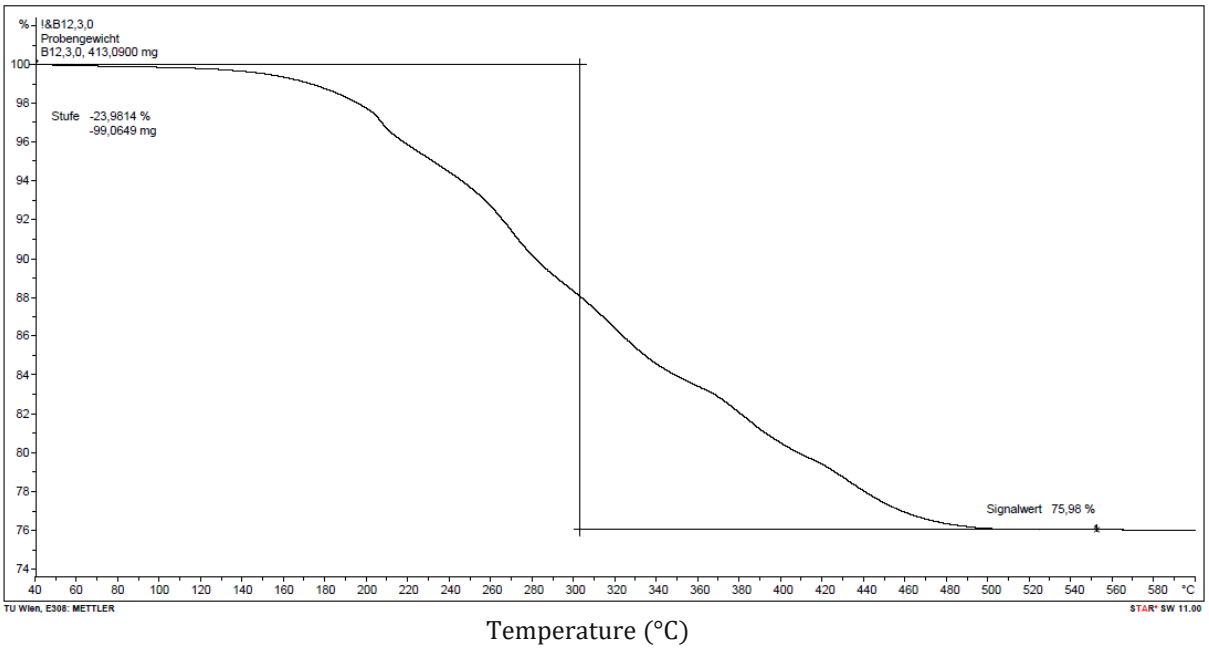

Figure 45: TGA plot of a fiber-free green body of the optimized composition.

5.4. Mechanical Testing

5.4.1. Biaxial Bending Test

In order to establish whether the fiber-reinforcement reinforces the ceramic parts, mechanical testing was done. As described in the introduction the focus was kept on biaxial bending tests, as they are commonly used for bioceramics.

When looking at the established stress-strain-plot, in Fig. 46, two different regions were of interest. The set of lines reaching around 200 MPa biaxial bending strength, came from the platelets, that were printed upright (ZYX). The set, reaching around 460 MPa, corresponded to flatwise (YXZ) platelets.

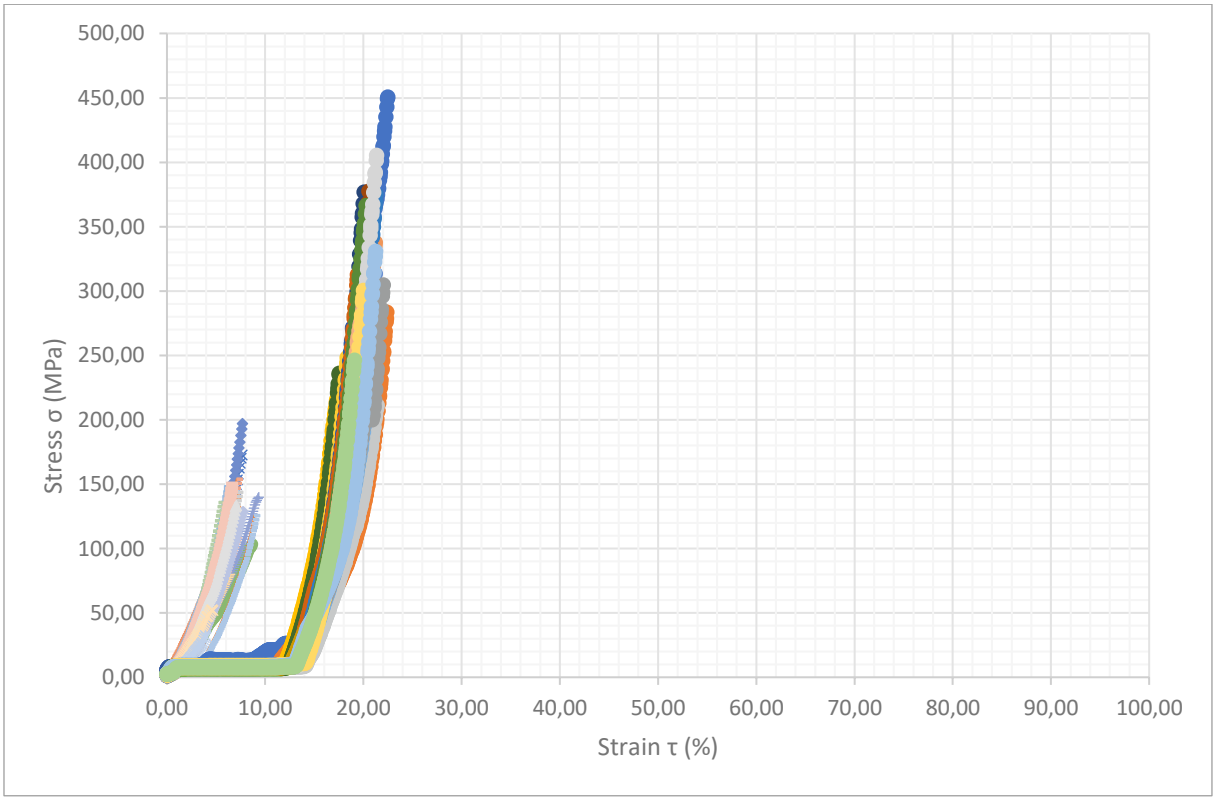

Figure 46: Stress-Strain diagram; left the printed upright samples and right the flatwise samples of the 1 wt.-% B102 and 5 wt.-% 2155 slurry.

There were different explanations on why the bending strength values differed so substantially. Firstly, it had to do with how the printed layers were orientated during the bending test. While for the upright samples, one applied pressure alongside the different layers, for the flatwise samples, the printed layers stood orthogonally to the pressure vector. Supporting this theory, was the fact that all upright printed samples broke into two pieces, not the usual three.

When looking at the SEM images of the fracture surface an additional factor came into play. All fibers aligned orthogonally in the case of the flatwise printed samples. This could also add to the biaxial bending strength of the flatwise samples.

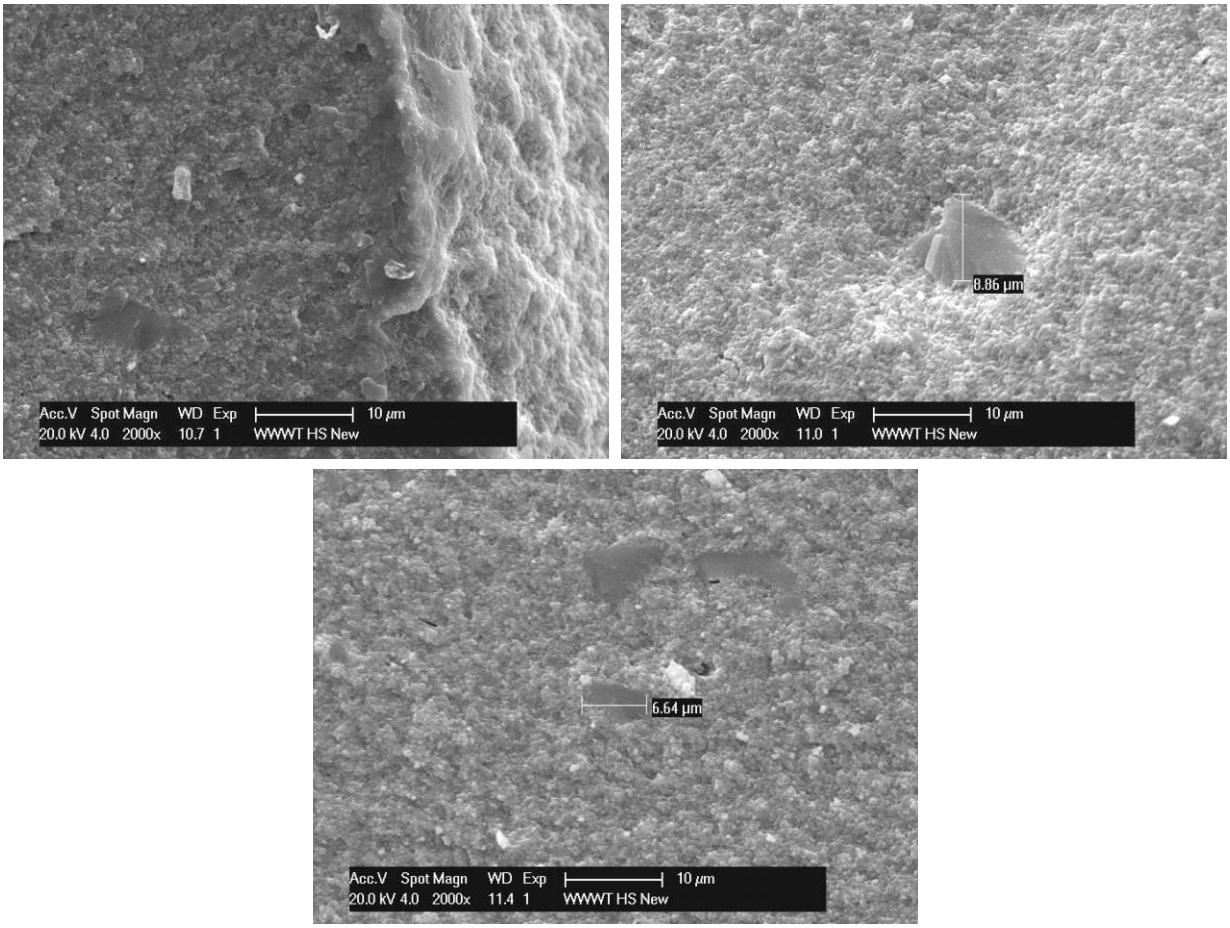

Figure 47: SEM images of fracture surface of the flatwise samples.

Based on the measured diameter of the fibers, which exceeded the expected values of around 2 µm, it is valid assumption, that the fibers either agglomerated or that there were also some bigger non-fiber particles present.

The upright printed samples the fibers (Fig. 48) showed an anisotropic distribution, sometimes laying alongside the fracture surface and sometimes standing orthogonal to it. In these images, the fibers could be identified clearly. Different to Fig. 47, there were not only agglomerates, but also single fibers orthogonally orientated. This can be seen in the upper left image.

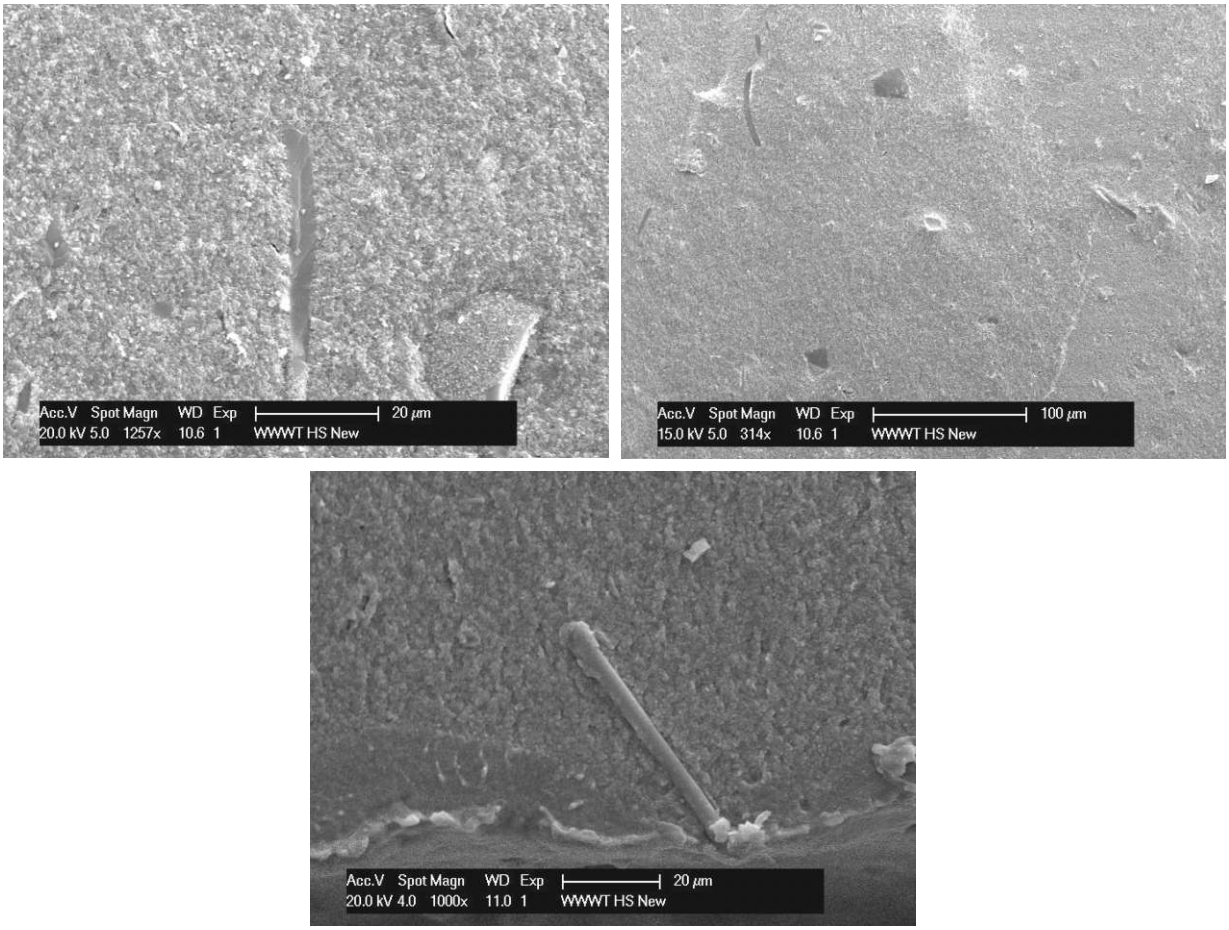

Figure 48: SEM images of the fracture surface of the upright parts.

When looking at the stress-strain-plot of the pure Al_2O_3 parts, one needs to look a little bit closer in order to distinguish between the flatwise und upright printed parts. There were two different maxima reached, one at around 200 MPa und and one at 440 MPa. The lower values again corresponding to the upright printed samples and the higher values to the flatwise printed parts.

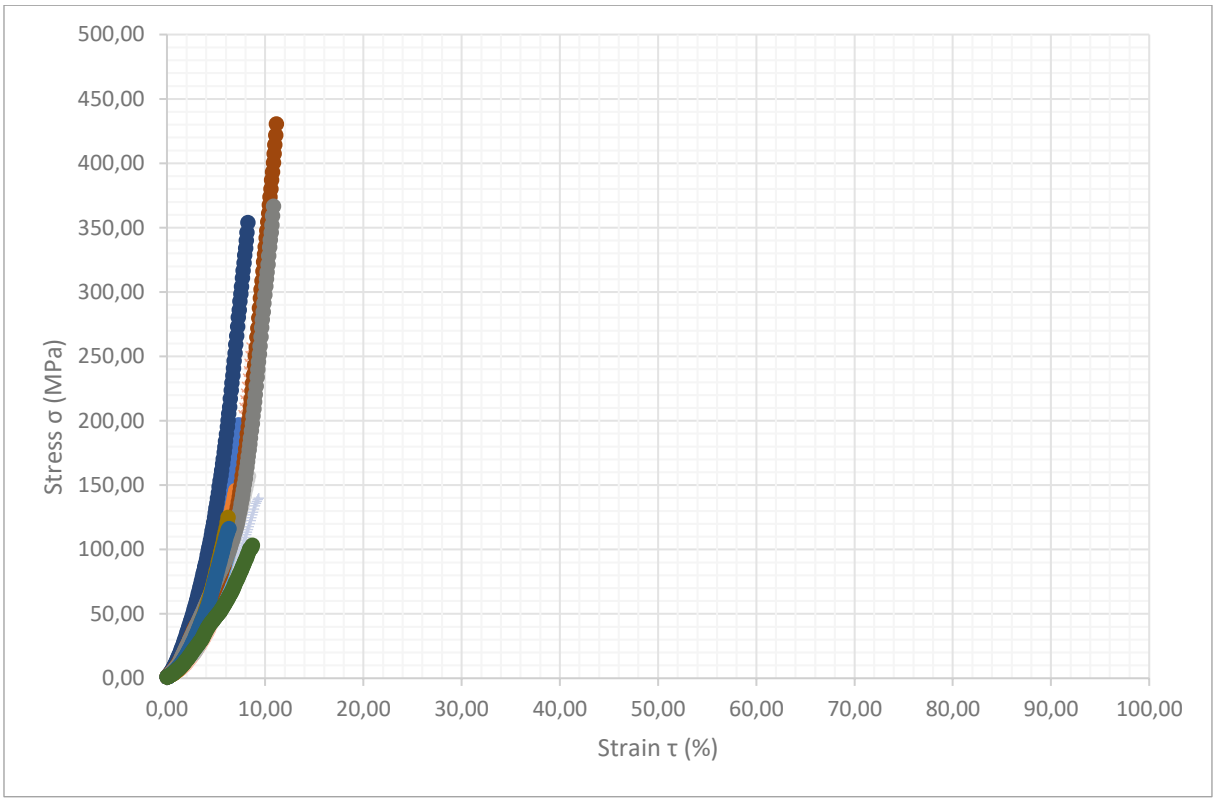

Figure 49: Stress-Strain diagram; the printed upright samples and the flatwise samples of the slurry without B102-Fibers and 5 wt.-% 2155.

The same patterns in the breakage could be seen as well. Again, all the upright printed samples split into two parts, while the couches parts split into the expected three parts.

When looking at Fig. 50, one can easily differentiate the parts with fibers from the ones without fibers, as the ones with fibers (bright colors) were parallel shifted to higher strain. This would be a major improvement, going from an average elongation at break of 10,66 ± 2,11 % to 24,39 ± 1,65 %.

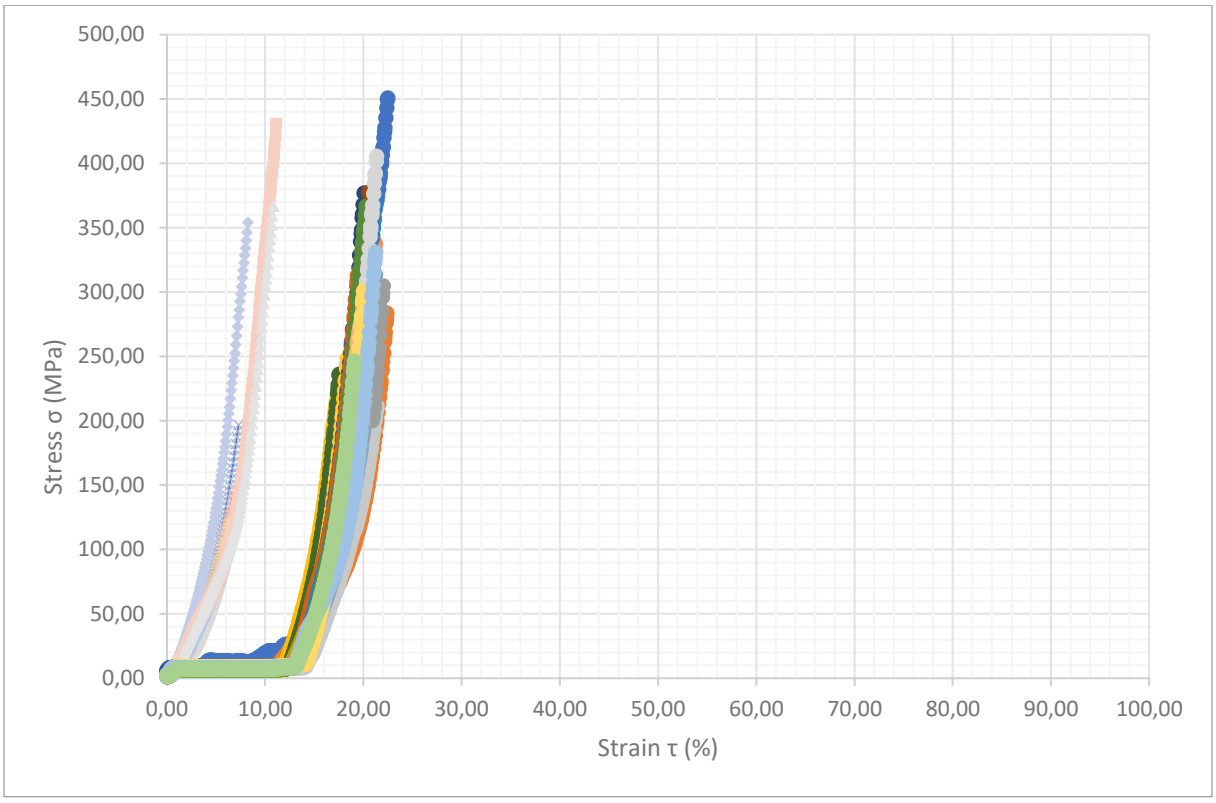

Figure 50: Stress-strain diagram of the flatwise samples of the slurry without B102-fibers and 5 wt.-% 2155 (left) and with B102-fibers and 5 wt.-% 2155 (right).

When comparing their maximum bending strength, one could assume a slight improvement. The flatwise parts with fibers showed a maximum of 451 MPa with an average of 290 ± 83 MPa. The non-reinforced parts had a maximum of 430 MPa and an average of 286 ± 63 MPa. But as both standard deviation values were included in the others error tolerance, this was not the case.

When looking at the measurement in more detail, one sees that there is still room for improvement, as we have a rather big standard deviation. Also, for the fiber samples, there were quite a few parts that broke at values that clearly correlate with defects in the platelet.

In Fig. 51, the upright printed parts are displayed. The first big difference to coached samples was the significantly lower bending strengths. Not even the clear stray bullet at around 250 MPa

came close to the average of the flatwise ones. The second thing visible was the missing parallel shift of the fiber-reinforced samples (bright colors). The pure Al_2O_3 samples (pastel colors) had a moderately higher elongation at break of 8,16 ± 1,81 % compared to 7,85 ± 1,81 %. This is probably an effect of the isotropic distribution of the fibers, as the fibers aligning parallel with the printed layers provide predetermined breaking points and thereby limiting deformation.

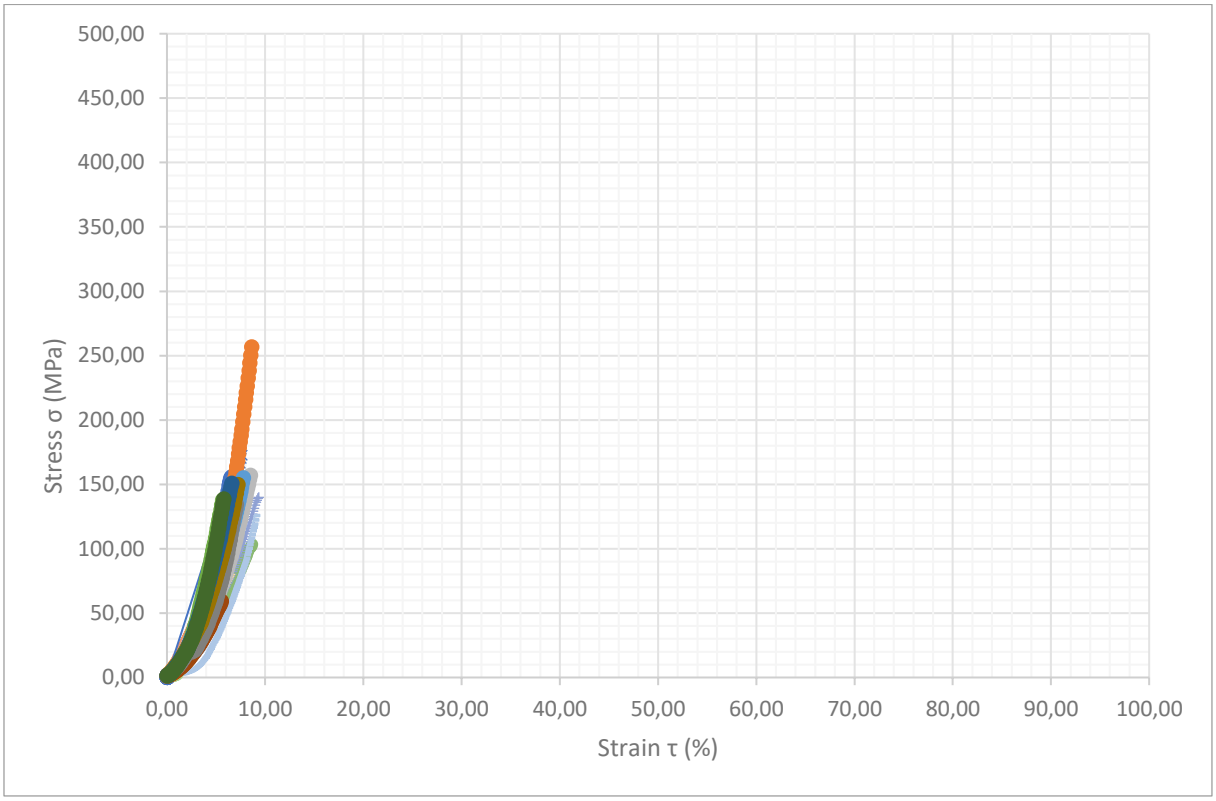

Figure 51: Stress-Strain diagram; the printed upright samples of the slurry with and without B102-Fibers and 5 wt.-% 2155.

This trend could also be seen in the bending strength, with an average of 141 ± 48 MPa for the ceramic parts and 119 ± 35 MPa for the reinforced samples. The same finding as for the flatwise parts worsened for the upright printed samples, as serval tiles broke below a stress value of 50 MPa. This clearly underlined the anisotropic behavior of fiber reinforcement, even with short fibers, when working with an DLP approach. It also strongly suggested, that research in the field of fiber alignment would be of great interest.

5.4.2. Weibull Modulus

The strength values of ceramic parts are not normally distributed. The Weibull Modulus describes the shape of the strength distribution as function of the probability of failure. When m is similar, but inverse in terms of the standard deviation, to a normal distribution, this means: the smaller m the bigger is the scattering of the data. The characteristic Weibull strength expresses the strength of a sample at a probability of 63,2 % to fail under the tested circumstances.[18]

Out of the equations seen in Fig. 52, the Weibull modulus and the characteristic Weibull strength could be collected, seen in Table 10.

Table 10: Results of the Weibull analysis

Sample	Weibull Modulus	Weibull Strength
Alumina flatwise	4.51	298.46
Alumina upright	4.38	162.35
Fiber-reinforced flatwise	3.81	310.39
Fiber-reinforced upright	6.60	134.78

As the minimum sample number was only reached for the fiber-reinforced part, only their values will be discussed further.

With a Weibull modulus of 3.81 the print of the flatwise fiber-reinforced parts showed the biggest scattering. The Weibull strength underlined the findings made before; the fiber-reinforcement showed some effect in increasing the strength of the material. It yielded a characteristic strength of 310.39 MPa.

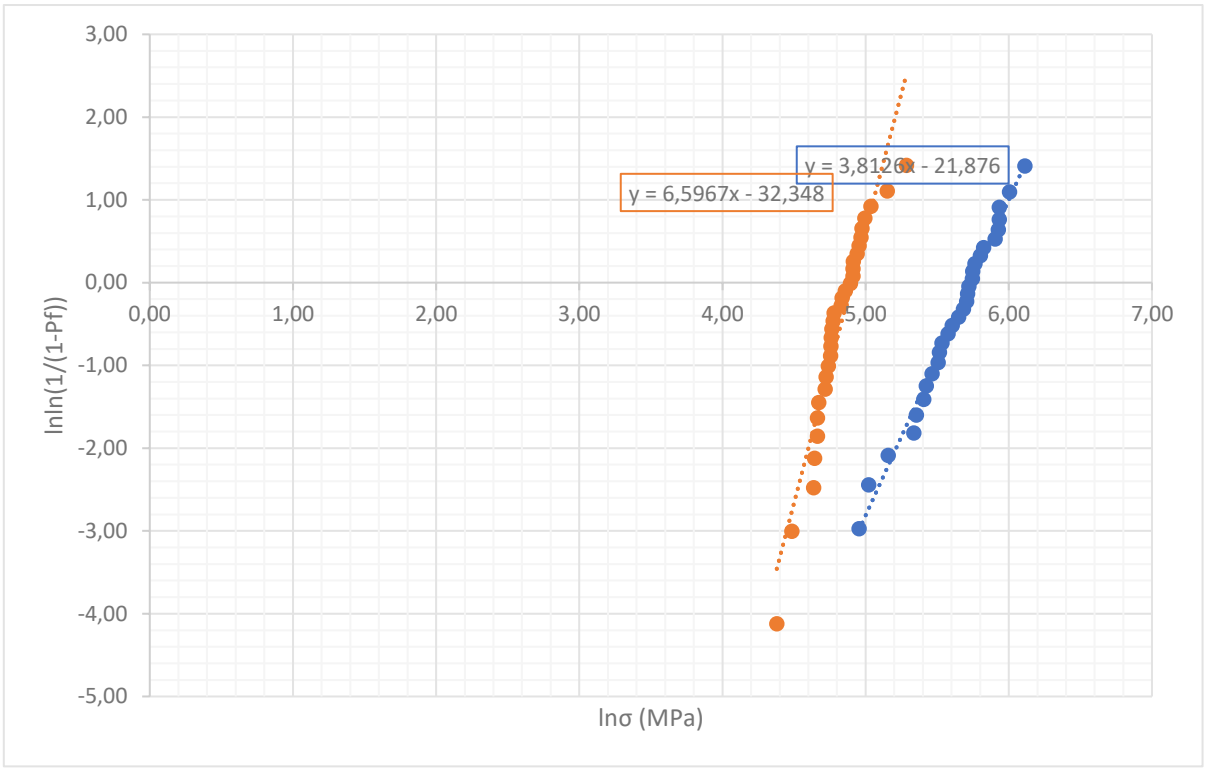

Figure 52: Weibull analysis of the reinforced parts, in blue the flatwise samples and the upright ones in orange.

Interestingly, the upright printed reinforced parts had the highest modules at 6.60 and thereby the lowest scattering. This underlined the case made before, that the fibers between the printed layers acted as defects and at a similar force applied debonding happened between the fibers and the matrix initiating failure of the parts.

This also showed in the Weibull strength, as the reinforced samples only reached a strength of 134 MPa.

5.5. Density Determination by Archimedes' Principle

The results, shown in Table 10, gave insight in the density and porosity of the samples. The adaptations in the sintering profiles yielded in differently dense sintered parts, based on the peak temperature.

Table 11: Density Measurement of 6x6 mm cylinders with fibers

Sintering Peak-T (°C)	**Measurement**	**Weight in Air W(a) (g)**	**Buoyancy of the Sample G (g)**	**Density ϱ (g/cm³)**	**Δ ϱ (g/cm³)**
1600	1	0.27097	0.06878	3.927	0.012
	2	0.27168	0.06918	3.915	
1600	1	0.27041	0.06829	3.947	0.006
	2	0.27054	0.06843	3.941	
1350	1	0.27551	0.07215	3.806	0.032
	2	0.27604	0.07290	3.775	
1300	1	0.27527	0.07068	3.882	0.164
	2	0.28084	0.07530	3.718	
1300	1	0.27990	0.07140	3.908	0.247
	2	0.28710	0.07818	3.661	
1300	1	0.27400	0.07093	3.851	0.164
	2	0.28070	0.07590	3.687	
1300/1250	1	0.27654	0.07338	3.757	0.027
	2	0.27833	0.07439	3.730	

As one can tell, the density of the samples dropped with decreasing sintering peak temperature. As the average density after sintering at 1600 °C was 3.937 g/cm^3 (considering the second measurement), 3.783 g/cm^3 at 1350 °C and 3.697 g/cm^3 at 1300 °C. The theoretical density lies at 3.94 g/cm^3.

The 1300/1250 °C sample, as can be seen in chapter 5.3.2, had a dwelling time at 1250 °C. This was done in the hope, that this way the sample would become denser, without destroying the fibers. With a density of 3.738 g/cm^3, this was the case when compared to the 1300 °C samples. What underlined this finding, was the low Δϱ. This value can be seen an indicator of the sample

porosity, as it showed how much the density changed, when the measurement was conducted a consecutive, second time. This correlates to non-infiltrated pores in sample.

It was thereby possible, to reach the same density with the 1300/1250 °C samples as with 1350 °C, without exceeding the maximum working temperature of the fibers (1300 °C), provided by the manufacturer.[92]

In comparison with Table 11, which shows the density of the ceramic parts without fibers, the reference measurement of the sample sintered at 1600 °C showed a slightly lower density at 3.893 g/cm^3, this mainly comes from the higher $\Delta\varrho$, indicating a higher porosity compared to fiber containing samples.

Table 12: Density measurement of 6x6 mm cylinders without fibers

Sintering Peak-T (°C)	**Measurement**	**Weight in Air W(a) (g)**	**Lift of the Sample G (G)**	**Density ϱ (g/cm^3)**	**$\Delta\varrho$ (g/cm^3)**
1600	1	0.19486	0.04909	3.957	0.064
	2	0.19500	0.04993	3.893	
1300/1250	1	0.19427	0.04898	3.954	0.182
	2	0.19723	0.05212	3.772	
1300/1250	1	0.19905	0.05192	3.822	0.032
	2	0.19918	0.05239	3.790	
1300/1250	1	0.19446	0.05112	3.792	0.079
	2	0.19461	0.05225	3.713	

When comparing to the theoretical density of 3.94 g/cm^3, a 99 % densification in both cases at 1600 °C, showed that a dense ceramic part was created. When looking at 1300/1250 °C, 95 % densification could be achieved for both the ceramic and CMC part.

6. Conclusion

Before going into more detail, it can be said, that the goal of the thesis could be obtained, as it is indeed possible to 3D print fiber-reinforced ceramic parts via a DLP approach.

To make this possible, it was necessary to work on three major topics: (1) optimization of the slurry, (2) optimization of the print parameters and (3) thermal postprocessing.

Via fine tuning of the matrix composition and investigation of different dispersing agents and techniques it was possible to create a composite slurry that shows a good property profile for 3D printing. The viscosity was clearly below the maximum allowed value of 15-20 Pa*s at a shear rate of 20 min^{-1}. Furthermore, it was possible to produce a slurry where the Al_2O_3 agglomerates were smaller than 30 µm. This made the slurry printable with a wet layer thickness of 50 µm.

For the optimization of the print, curing depth measurements were conducted. These yielded expected reslts, the slurry with the highest amount of fibers and Disperbyk-2155 had the lowest critical light exposure (E_c) with 6.72 mJ/cm^2 and a penetration depth (D_p) of 0.33 mm. The highest values of critical exposure and penetration depth were achieved by the base formulation without fibers at 13.68 mJ/cm^2 and 0.50 mm. These results underline, that the fibers caused light scattering, which needs to be considered in the printing parameters.

Thermal postprocessing turned out to be the biggest challenge of this thesis. As discussed in chapter 5.3.1, a rather long debinding profile needed to be found, in order to create defect-free ceramic part ready for sintering. On the other hand, it could be proven, that the addition of fibers helps with this process, as the fiber-reinforced parts also debinded defect-free with the starting point profile. Additionally, the variation of sintering profiles, as suspected, had an effect the properties of the ceramic part.

Concluding with the mechanical testing, unfortunately the bending strength could not be increased significantly. The fiber-reinforced flatwise samples did show the highest average bending strength of 290 ± 83 MPa, but not significantly, the non-reinforced sample having a value of 268 ± 63 MPa. Very interesting and promising was an increased elongation for the flatwise fiber-reinforced samples, doubling the value of the Al_2O_3 with 24.2 %.

In further research, it would be interesting to closer investigate lower viscosity slurries. Here, it would be possible to make use of the promising ultrasonic dispersing technique, which was

not tested with fibers during this thesis. When the increased viscosity stems from an adjusted proportion of polymer to diluent, this can also benefit the debinding properties of the slurry. As discussed in chapter 3.6.1, the diluent is the first component to evaporate or decompose of the organic matrix. The thereby formed channels help for a milder, gentler debinding later on in the process.

Of uttermost importance is the future investigation of higher fiber content in the slurry and therefor in the CMC material. This could cause an improvement of the bending strength, elongation at break and lead to toughening of the material.

Lastly, the transition to biodegradable and bioresorbable material for both the ceramic matrix as well as the ceramic filler material would be a very interesting. This could benefit future generation to have more unproblematic bone replacement, while also providing enough strength and toughness during the healing process.

7. References

1. Hoffman, T., Khademhosseini, A. & Langer, R. Chasing the Paradigm: Clinical Translation of 25 Years of Tissue Engineering. *Tissue Eng. - Part A* **25**, 679–687 (2019).

2. Langer, R. Tissue Engineering. *Science (80-.).* **260**, 920–926 (1993).

3. Baino, F. *Ceramics for bone replacement: Commercial products and clinical use*. *Advances in Ceramic Biomaterials: Materials, Devices and Challenges: First Edition* (Elsevier Ltd, 2017). doi:10.1016/B978-0-08-100881-2.00007-5.

4. Ramos, T. & Moroni, L. Tissue Engineering and Regenerative Medicine 2019: The Role of Biofabrication - A Year in Review. *Tissue Eng. - Part C Methods* **26**, 91–106 (2020).

5. Nichol, J. W. & Khademhosseini, A. Modular tissue engineering: Engineering biological tissues from the bottom up. *Soft Matter* **5**, 1312–1319 (2009).

6. Raquel Maia, F., Correlo, V. M., Oliveira, J. M. & Reis, R. L. *Natural Origin Materials for Bone Tissue Engineering*. *Principles of Regenerative Medicine* (Elsevier Inc., 2019). doi:10.1016/b978-0-12-809880-6.00032-1.

7. Ghassemi, T. Current Concepts in Scaffolding for Bone Tissue Engineering. *Arch Bone Jt Surg.* vol. 6 90–99 (2018).

8. Palmer, L. C., Newcomb, C. J., Kaltz, S. R., Spoerke, E. D. & Stupp, S. I. Biomimetic systems for hydroxyapatite mineralization inspired by bone and enamel. *Chem. Rev.* **108**, 4754–4783 (2008).

9. H., D. Ueber Knochenpiombirung. *Beitr Klin Chir* 804–810 (1892).

10. Dorozhkin, S. V. A detailed history of calcium orthophosphates from 1770s till 1950. *Mater. Sci. Eng. C* **33**, 3085–3110 (2013).

11. Wang, W. & Yeung, K. W. K. Bone grafts and biomaterials substitutes for bone defect repair: A review. *Bioact. Mater.* **2**, 224–247 (2017).

12. Chevalier, J. & Gremillard, L. Ceramics for medical applications: A picture for the next 20 years. *J. Eur. Ceram. Soc.* **29**, 1245–1255 (2009).

13. Saini, M. Implant biomaterials: A comprehensive review. *World J. Clin. Cases* **3**, 52 (2015).

14. Choudhari, C. M. & Patil, V. D. Product Development and its Comparative Analysis by SLA, SLS and FDM Rapid Prototyping Processes. *IOP Conf. Ser. Mater. Sci. Eng.* **149**, (2016).

15. Ha, S.-W. & Wintermantel, E. Biokompatible Keramische Werkstoffe. *Medizintechnik* 277–297 (2009) doi:10.1007/978-3-540-93936-8_13.

16. Schmücker, M. Faserverstärkte Oxidkeramische Werkstoffe. *Materwiss. Werksttech.* **38**, 698–704 (2007).

17. Chen, Z. *et al.* 3D printing of ceramics: A review. *J. Eur. Ceram. Soc.* **39**, 661–687 (2019).

18. Technischen Komitee ISO/TC 106 „Dentistry“, Technischen Komitee CEN/TC 55 „Zahnheilkunde“ & DIN Deutsches Institut für Normung. Dentistry - Ceramic Materials (ISO 6872:2015 + Amd.1:2018). (2019).

19. ISO. DRAFT INTERNATIONAL STANDARD ISO / DIS 17296-1 Additive manufacturing — General principles — Part 1 : Terminology. *Addit. Manuf.* **2014**, (2015).

20. Hopmann, C., Greif, H. & Wolters, L. Additive Fertigungsverfahren. *Technol. der Kunststoffe* 159–169 (2021) doi:10.3139/9783446469600.015.

21. Holzmann, P., Schwarz, E. J. & Audretsch, D. B. Understanding the determinants of novel technology adoption among teachers: the case of 3D printing. *J. Technol. Transf.* **45**, 259–275 (2020).

22. Thomas. 3D printed jellyfish robots created to monitor fragile coral reefs. *3D Printer and 3D Printing News* http://www.3ders.org/articles/20181003-3d-printed- (2018).

23. Tofail, S. A. M. *et al.* Additive manufacturing: scientific and technological challenges, market uptake and opportunities. *Mater. Today* **21**, 22–37 (2018).

24. Breuninger, J., Becker, R., Wolf, A., Rommel, S. & Verl, A. Generative Fertigung mit Kunststoffen. *Gener. Fert. mit Kunststoffen* 113–114 (2013) doi:10.1007/978-3-642-24325-7.

25. Ngo, T. D., Kashani, A., Imbalzano, G., Nguyen, K. T. Q. & Hui, D. Additive manufacturing (3D printing): A review of materials , methods , applications and challenges. *Compos. Part B* **143**, 172–196 (2018).

26. I. Gibson, D. W. Rosen, B. S. *Rapid Prototyping to Direct Digital Manufacturing*. *Additive Manufacturing Technologies* (2010).

27. Gibson, I. History of Stereolithographic Processes. (2011) doi:10.1007/978-0-387-92904-0.

28. Melchels, F. P. W., Feijen, J. & Grijpma, D. W. A review on stereolithography and its applications in biomedical engineering. *Biomaterials* **31**, 6121–6130 (2010).

29. Mahesh, M. & Wong, Y. S. Benchmarking for comparative evaluation of RP systems and processes. **10**, 123–135 (2004).

30. Struve, B. *Einführung in die Lasertechnik: Physikalische und technische Grundlagen für die Praxis*. (2008).

31. Raman, R. & Bashir, R. *Stereolithographic 3D bioprinting for biomedical applications*. *Essentials of 3D Biofabrication and Translation* (Elsevier Inc., 2015). doi:10.1016/B978-0-12-800972-7.00006-2.

32. Lee, I. H. & Cho, D. W. An investigation on photopolymer solidification considering laser irradiation energy in micro-stereolithography. *Microsyst. Technol.* **10**, 592–598 (2004).

33. Park, J. H., Jang, J., Lee, J. S. & Cho, D. W. Three-Dimensional Printing of Tissue/Organ Analogues Containing Living Cells. *Ann. Biomed. Eng.* **45**, 180–194 (2017).

34. Farkas, B. *et al.* Four-order stiffness variation of laser-fabricated photopolymer biodegradable scaffolds by laser parameter modulation. *Mater. Sci. Eng. C* **55**, 14–21 (2015).

35. Lim, T. A. E. W. O. O. & Park, S. H. U. Two-photon stereolithography. **16**, 59–73 (2007).

36. Piqué, A., Auyeung, R. C. Y., Kim, H., Charipar, N. A. & Mathews, S. A. Laser 3D micro-manufacturing. *J. Phys. D. Appl. Phys.* **49**, (2016).

37. Stampfl, J. *et al.* Photopolymers with tunable mechanical properties processed by laser-based high-resolution stereolithography. *J. Micromechanics Microengineering* **18**, (2008).

38. Chia, H. N. & Wu, B. M. Recent advances in 3D printing of biomaterials. *J. Biol. Eng.* **9**, 1–14 (2015).

39. Bertsch, A., Jiguet, S. & Renaud, P. Microfabrication of ceramic components by microstereolithography. *J. Micromechanics Microengineering* **14**, 197–203 (2004).

40. Xie, R. & Li, D. Research on the curing performance of UV-LED light based stereolithography. *Opt. Laser Technol.* **44**, 1163–1171 (2012).

41. Felzmann, R. *et al.* Lithography-based additive manufacturing of customized bioceramic parts for medical applications. *Proc. IASTED Int. Conf. Biomed. Eng. BioMed 2013* 442–446 (2013) doi:10.2316/P.2013.791-129.

42. Felzmann, R. *et al.* Lithography-based additive manufacturing of cellular ceramic structures. *Adv. Eng. Mater.* **14**, 1052–1058 (2012).

43. Mitteramskogler, G. *et al.* Light curing strategies for lithography-based additive manufacturing of customized ceramics. *Addit. Manuf.* **1**, 110–118 (2014).

44. Lasgorceix, M., Champion, E. & Chartier, T. Shaping by microstereolithography and sintering of macro-micro-porous silicon substituted hydroxyapatite. *J. Eur. Ceram. Soc.* **36**, 1091–1101 (2016).

45. Wallace, J. *et al.* Validating continuous digital light processing (cDLP) additive manufacturing accuracy and tissue engineering utility of a dye-initiator package. *Biofabrication* **6**, (2014).

46. Gmeiner, R., Mitteramskogler, G., Stampfl, J. & Boccaccini, A. R. Stereolithographic ceramic manufacturing of high strength bioactive glass. *Int. J. Appl. Ceram. Technol.* **12**, 38–45 (2015).

47. Lantada, A. D., De Blas Romero, A., Schwentenwein, M., Jellinek, C. & Homa, J. Lithography-based ceramic manufacture (LCM) of auxetic structures: Present capabilities and challenges. *Smart Mater. Struct.* **25**, (2016).

48. Gruber, S. (12) Patent Application Publication (10) Pub . No .: US 2016 / 0271610 A1 Patent Application Publication. **1**, 1–5 (2016).

49. Gmeiner, R. *et al.* Additive manufacturing of bioactive glasses and silicate bioceramics. *J. Ceram. Sci. Technol.* **6**, 75–86 (2015).

50. Dorfinger, P., Stampfl, J. & Liska, R. Toughening of photopolymers for stereolithography (SL). *Mater. Sci. Forum* **825–826**, 53–59 (2015).

51. Allcock, H. R., Lampe, F. W. & Mark, J. F. Contemporary Polymer Chemistry. in 29–30 (2003).

52. Fried, J. R. *Polymer Science & Technology: Third Edition*. *Prentice Hall* (2014).

53. Nesvadba, P. Radical polymerization in industry. In Encyclopedia of Radicals in Chemistry, Biology and Materials. *Encyclopedia of Radicals in Chemistry, Biology and Materials* (2012).

54. Qin, X. H., Ovsianikov, A., Stampfl, J. & Liska, R. Additive manufacturing of photosensitive Hydrogels for tissue engineering applications. *BioNanoMaterials* **15**, 49–70 (2014).

55. Lunzer, M. Synthesis and Characterization of Triarylamine Based Materials as Two Photon Absorption Photoinitiators. (2014).

56. Green, W. A. *Industrial Photoinitiators*. *Industrial Photoinitiators* (2010). doi:10.1201/9781439827468.

57. Gruber, H. F. Photoinitiators for free radical polymerization. *Prog. Polym. Sci.* **17**, 953–1044 (1992).

58. Ganster, B., Fischer, U. K., Moszner, N. & Liska, R. New photocleavable structures. Diacylgermane-based photoinitiators for visible light curing. *Macromolecules* **41**, 2394–2400 (2008).

59. Radebner, J. *et al.* Tetraacylgermanes: Highly Efficient Photoinitiators for Visible-Light-Induced Free-Radical Polymerization. *Angew. Chemie - Int. Ed.* **56**, 3103–3107 (2017).

60. Gorsche, C. *et al.* New generation of highly efficient long- wavelength photoinitiators for dental restoratives : From research to application. *Radtech Conf.* **2**, (2014).

61. Jacobs, P. F. Rapid prototyping & manufacturing— Fundamentals of stereolithography. *J. Manuf. Syst.* **12**, 430–433 (1992).

62. O'Neill, P. F. Internal void fabrication via mask projection micro-stereolithography : A rapid repeatable microfluidic prototyping technique. 173 (2018) doi:10.13140/RG.2.2.14152.78080.

63. Halloran, J. W. Freeform fabrication of ceramics. *Br. Ceram. Trans.* **98**, 299–303 (1996).

64. Song, X., Chen, Y., Lee, T. W., Wu, S. & Cheng, L. Ceramic fabrication using Mask-Image-Projection-based Stereolithography integrated with tape-casting. *J. Manuf. Process.* **20**, 456–464 (2015).

65. Gruber, S. Lithography-based additive manufacturing of alumina parts. (2013).

66. Saruhan, B. 2 CHARACTERISTICS OF OXIDE-BASED FIBER-. (2003).

67. Chawla, K. K. *Ceramic Matrix Composites Second Edition*. (2003).

68. Lu, Z., Cao, J., Song, Z., Li, D. & Lu, B. Research progress of ceramic matrix composite parts based on additive manufacturing technology. *Virtual Phys. Prototyp.* **14**, 333–348 (2019).

69. Lewicki, J. P. *et al.* 3D-Printing of Meso-structurally Ordered Carbon Fiber/Polymer Composites with Unprecedented Orthotropic Physical Properties. *Sci. Rep.* **7**, 1–14 (2017).

70. Compton, B. G. & Lewis, J. A. 3D-printing of lightweight cellular composites. *Adv. Mater.* **26**, 5930–5935 (2014).

71. Yunus, D. E., He, R., Shi, W., Kaya, O. & Liu, Y. Short fiber reinforced 3d printed ceramic composite with shear induced alignment. *Ceram. Int.* **43**, 11766–11772 (2017).

72. Chen, Z. C., Kulkarni, R., Chawla, K. K., Koopman, M. & Ikeda, K. Processing and microstructure of an all-oxide ceramic composite. *Mater. Sci. Forum* **475–479**, 1301–1304 (2005).

73. Abyzov, A. M. Aluminum Oxide and Alumina Ceramics (review). Part 1. Properties of Al2O3 and Commercial Production of Dispersed Al2O3. *Refract. Ind. Ceram.* **60**, 24–32 (2019).

74. Ribbe, P. H. The crystal structures of the aluminum-silicate feldspars. 1–2 (1994).

75. Pinkas, J. Chemistry of silicates and aluminosilicates. *Ceram. - Silikaty* **49**, 287–298

(2005).

76. MAZDIYASNI, K. S. & BROWN, L. M. Synthesis and Mechanical Properties of Stoichiometric Aluminum Silicate (Mullite). *J. Am. Ceram. Soc.* **55**, 548–552 (1972).

77. Gallup, D. L. Aluminum silicate scale formation and inhibition: Scale characterization and laboratory experiments. *Geothermics* **26**, 483–499 (1997).

78. McClement, D. J. *Food Emulsions: Principles, Practices, and Techniques, Second Edition*. (2004).

79. German, R. M. *Sintering Theory and Practice*. (1996).

80. Gonzlez-Gutirrez, J., Beulke, G. & Emri, I. Powder Injection Molding of Metal and Ceramic Parts. *Some Crit. Issues Inject. Molding* (2012) doi:10.5772/38070.

81. Md Ani, S., Muchtar, A., Muhamad, N. & Ghani, J. A. Binder removal via a two-stage debinding process for ceramic injection molding parts. *Ceram. Int.* **40**, 2819–2824 (2014).

82. Silva Jorge, H. Compounding and Processing of a Water Soluble Binder for Powder Injection Moulding. (2008).

83. Trunec, M. & Cihlar, J. Thermal removal of multicomponent binder from ceramic injection mouldings. *J. Eur. Ceram. Soc.* **22**, 2231–2241 (2002).

84. Mitteramskogler, G. Selective coloring of 3D-printed parts made of Zro2.". (2015).

85. de Blas Romero, A. *et al.* Lithography-based additive manufacture of ceramic biodevices with design-controlled surface topographies. *Int. J. Adv. Manuf. Technol.* **88**, 1547–1555 (2017).

86. EXNER, H. E. & ARZT, E. Sintering Processes. *Phys. Metall.* 2627–2662 (1996) doi:10.1016/b978-044489875-3/50036-3.

87. Kang, S.-J. L. Sintering Processes. *Sintering* 3–8 (2005) doi:10.1016/b978-075066385-4/50001-7.

88. Ag, I. V. Meilenstein Technologie. 1–44 (2013).

89. Gozneli, R., Kazazoglu, E. & Ozkan, Y. Flexural properties of leucite and lithium disilicate ceramic materials after repeated firings. *J. Dent. Sci.* **9**, 144–150 (2014).

90. Sartorius AG. *Sartorius Anleitung - Anhang*. (1997).

91. Pfaffinger, M., Mitteramskogler, G., Gmeiner, R. & Stampfl, J. Thermal debinding of ceramic-filled photopolymers. *Mater. Sci. Forum* **825–826**, 75–81 (2015).

92. Unifrax Ltd. Fiberfrax Bulk and Chopped Fibers. **44**, 1–2 (2009).